DEVELOPMENT OF A NEW SURFACE ION-SOURCE AND ION GUIDE IN THE ALTO PROJECT

P. V. Cuong

UNIVERSITÉ DE PARIS-SUD 11
U.F.R. SCIENTIFIQUE D'ORSAY

THÈSE DE DOCTORAT

présentée par

PHAN VIET CUONG

pour obtenir le grade de docteur en sciences de l'université Paris XI Orsay

Sujet:

DEVELOPMENT OF A NEW SURFACE ION-SOURCE AND ION GUIDE IN THE ALTO PROJECT

Soutenue le 16 December 2009 devant la Commission d'examen

M.	**Mushin HARAKE**	Rapporteur
M.	**Fadi IBRAHIM**	Directeur de Thèse
M.	**Serge FRANCHOO**	Examinateur
M.	**Tran Duc THIEP**	Directeur de Thèse
MMe.	**Tiina SUOMIJÄRVI**	Président
MMe.	**Marie-Geneviève SAINT-LAURENT**	Rapporteur

To my family.

Résumé

Pour le projet ALTO l'IPN d'Orsay, comme pour d'autres laboratoires qui exploitent la technique ISOL pour produire des faisceaux radioactifs intenses et purs, il est crucial, lorsque des isotopes de courte durée de vie sont produits dans des cibles épaisses, de réaliser des cibles et des sources d'ions avec des bonnes propriétés de sortie et de haute efficacité. Ainsi les études de R&D sur les cibles et les sources d'ions sont très importantes pour l'optimisation de la production, la sélectivité et la sortie des isotopes d'intérêt. Ces études sont aussi nécessaires vers les futurs installations transnationales de recherche en physique nucléaire SPIRAL-2 et EURISOL. Le travail présent est consacré à la production d'isotopes de gallium riches en neutrons par la technique de cible épaisse ISOL reposant sur la photo-fission et l'ionisation de surface. Nous visons à l'étude de la structure nucléaire du ^{82,83,84}Ge grâce à la désintegration bêta du ^{82,83,84}Ga. Dans ce but, nous nous concentrons sur le développement d'une nouvelle source d'ionisation de surface faite de matériaux à haute fonction de travail comme le Re et l'Ir. Un code C++ a été construit pour simuler l'efficacité d'ionisation de la source pour des surfaces différentes (des matériaux différents et des dimensions différentes) et le résultat a été comparé avec une base de données expérimentales du CERN. Le code peut être utilisé pour optimiser les dimensions de la source d'ions dans des agencements futurs. En même temps nous avons réalisé une expérience d'essai afin de mesurer l'efficacité d'ionisation du gallium dans des cavits de Re et Ir-Re. D'autre part, pour les études de structure nuclaire d'éléments

réfractaires, comme le cobalt ou le nickel, pour lesquels on s'attend à ce qu'ils révèlent un trésor d'informations de structure intéressantes, la technique ISOL à cible épaisse n'est plus appropriée. En effet, le point de fusion élevé de ces éléments fait qu'ils se volatilisent et se libèrent difficilement d'une cible épaisse. Alors une technique basée sur des cibles minces s'avère nécessaire et le guide d'ions à laser, basé sur une cellule à gaz pour thermaliser, neutraliser et arrêter les produits de réaction reculants suivie d'une ionisation résonnante laser pour les re-ioniser sélectivement, semble un bon choix. Cependant, afin de déterminer si la technique convient pour ALTO, nous devons répondre à la question quant au taux d'ionisation du gaz tampon par le faisceau primaire ainsi que les charges secondaires? Autrement dit, quel est le taux de production de paires ion-électron dans la cellule à gaz? En effet, un taux d'ionisation trop grand empêche l'extraction efficace des ions d'intérêt du guide d'ions à laser. Pour répondre à cette question, nous avons construit un code basé sur GEANT-4 pour simuler l'ionisation du gaz tampon. En outre, dans un mouvement vers le projet SPIRAL-2 au GANIL, où la fission de l'^{238}U sera induite par des neutrons produits dans un convertisseur carbonique depuis un faisceau de deutons, nous avons écrit un code GEANT-4 pour simuler la production de neutrons, la fission induite par neutron et le dépôt d'énergie dans une cellule à gaz de dimensions semblables à la cellule proposée pour ALTO.

Acknowledgements

Firstly, I would like to express my gratefullness to my supervisors at IPN Orsay, Prof. Fadi Ibrahim who has given me the opportunity to study at Institut de Physique Nucléaire, Orsay as well as spending his treasure time to help me through this work and Dr. Serge Franchoo who has always been ready to help me whenever I need, taught and supported me a lots. I am grateful to Prof. Tran Duc Thiep, my supervisor at IOP, Hanoi, who gave me the chance to work with him since I have graduated from University and led me to the research in nuclear physics.

I am very grateful to the members of my thesis review commitee, Prof. Muhsin Harake and Prof. Marie-Genevive SAINT-LAURENT who have read this thesis patiently and given many valuable comments, Prof. Tiina Suomijakvi who has accepted to be president of the commitee.

I am very grateful to Prof. Dominique Guillemaud-Mueller, who has been interested in my progress during the time I were studying in IPN Orsay. I would like to thank Dr. David Verney and Dr. Mathieu Lebois for their worthy helps, userful discussion and kind friendship. I express my thank to all members of the team of Tandem, especially, Dr. Said Essabaa, who always gave me the good conditions to perform my experiment. Laurence Berthier solved for me many administrative problems, for which I am very grateful.

I also would like to thank my colleagues and friends in Centre of Nuclear Physics, Institute of Physics, Hanoi for their friendships and encouragements.

I would like to give my deep gratitude to my parents, brothers for their encouragements at all time.

Finally, I express the most special thanks to my wife who has shared the difficulty with me and taken care my babies therefore I had the peace of mind to focus on my studying, to my beloved babies (Phan Le Phuong Linh and Phan Le Kien) who are the motivation for my working.

Contents

Chapter 1

Introduction

Among the nuclear physics community, there is nowadays a huge interest in nuclei that are located far away from the valley of stability. However, at a first glance at the nuclear chart, we can see vast unknown territories on the neutron-rich side of β stability, while research is impeded by experimental difficulties.

The study of these nuclei is expected to let us apprehend the behaviour of nuclear matter under extreme conditions as well as establish the evolution of the shell-model magic numbers for exotic nuclei. In order to study such nuclei, we often need intense and pure radioactive ion beams (RIB). To produce such beams, two complementary methods, the ISOL (Isotope Separation On-Line) and the in-flight method, are used in nuclear physics laboratories around the world.

For an ISOL-type facility, where the radioactive nuclei that are produced are stopped before being extracted, a powerful method is to use fission in thick targets, which can be induced by thermal neutrons, fast neutrons, protons or photons (see figure 1.1). A recent photo-fission experiment performed at CERN [15] has indicated that the photo-fission mode can be an attractive alternative to neutron-induced fission and this is the *raison d'être* for the ALTO project at IPN Orsay.

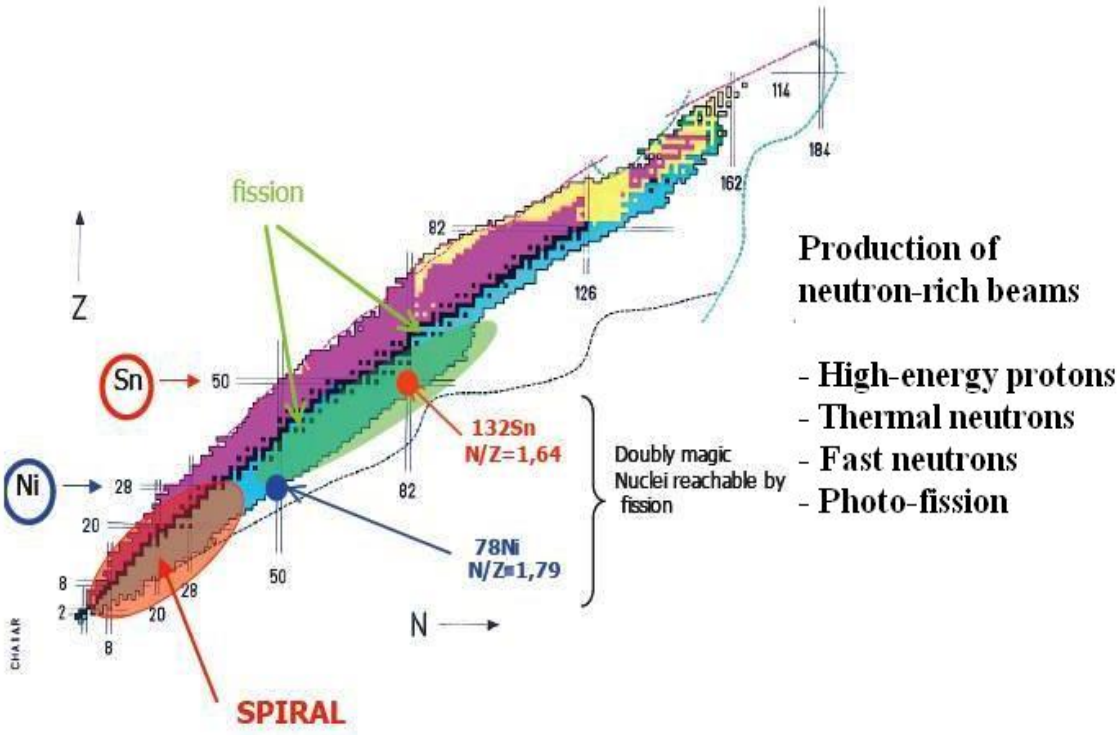

Figure 1.1: Nuclear regions that are reachable by fission [34]

At ALTO, a 50 MeV electron beam, which is delivered by a linear accelerator, interacts in a thick uranium target to produce bremsstrahlung. Fission is induced by those photons with an energy at the Giant Dipole Resonance (GDR) of ^{238}U. The GDR cross section of ^{238}U is shown in figure 1.2 and as can be seen, a maximum fission cross section of 160 mb is obtained for photons having an energy around 15 MeV. Besides, the results in [32] indicate that by increasing the energy of the electron beam the amount of bremsstrahlung and hence the photo-fission yield also grow, settling for 50 MeV as an optimal energy (see figure 1.2).

At the ALTO project, as at many others using the ISOL technique, it is crucial, when short-lived isotopes are produced in thick targets, to realise tar-

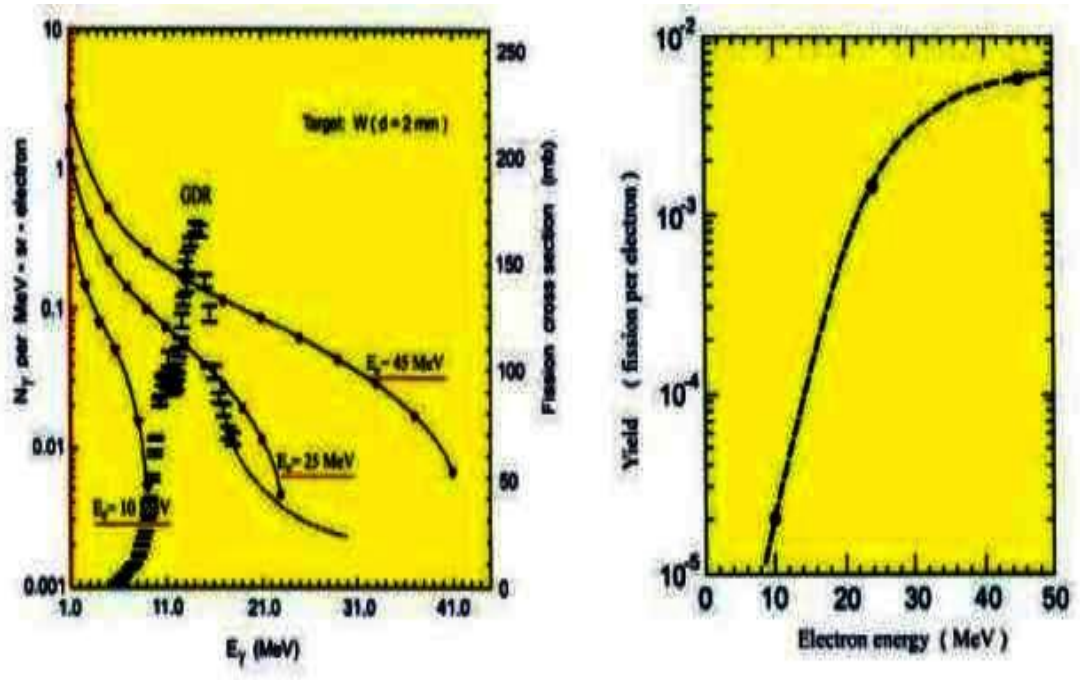

Figure 1.2: (a) The solid line is the γ spectrum produced by electrons of various energies. The dots are experimental data for the photo-fission cross section of ^{238}U. (b) Photo-fission yield per electron for ^{238}U as function of electron energy [32]

get and ion-source systems with good release properties and high efficiency. Therefore, R & D studies on target and ion source are very important for optimisation of the production, selectivity and release of the isotopes of interest. These studies are also needed towards the future SPIRAL-2 and EURISOL nuclear physics facilities [49, 57].

The present work is dedicated to the production of neutron-rich gallium isotopes by the ISOL thick-target technique using photo-fission and a surface ion source. We aim at the study of the structure of ${}^{82}_{32}Ge_{50}$, ${}^{83}_{32}Ge_{51}$, ${}^{84}_{32}Ge_{52}$ via the β decay of ${}^{82}_{31}Ga_{51}$, ${}^{83}_{31}Ga_{52}$, ${}^{84}_{31}Ga_{53}$.

We focus on the development of a new surface ion source made from materials with a high work function ϕ, which can give high ionisation efficiencies

for elements with low ionisation potentials, like alkalines as well as gallium and indium. For instance for gallium, its neighbour elements have a sufficiently higher ionisation potential and thus they are not ionised. As such a surface ion source can give us a very selective gallium ion beam. In accordance with the Saha-Langmuir theory, the ionisation efficiency does not only depend on the ioniser work function but also on the heating temperature. While the ionisation efficiency is proportional to the heating temperature, a high temperature of the ioniser also makes for a faster release of the short-lived isotopes and it reduces the decay losses. From these facts, the ioniser material must exhibit the following characteristics: high work function, high melting point and high electrical conductivity (for easy heating).

Apart from tungsten ($\phi = 4.55$ eV, $T_{melting} = 3422°$C) used at ISOLDE, rhenium ($\phi = 4.96$ eV, $T_{melting} = 3180°$C) and iridium ($\phi = 5.27$ eV, $T_{melting} = 2466°$C) are considered as good candidates for a surface ioniser because the Saha-Langmuir equation indicates for these materials high surface ionisation efficiencies. This has motivated us to equip the surface ion source at ALTO with rhenium and iridium-coated rhenium ioniser tubes of the same dimensions as the surface ion source at ISOLDE. We performed a test experiment to measure the ionisation efficiency for gallium. The present status and results of the experiment are described in chapter 4. We also built a simulation code for the ionisation efficiency of the different surface ionisation sources (different materials and dimensions), the result of which was compared with experimental data from CERN. The code can be used to optimise ion source dimensions in future designs (see chapter 4).

On the other hand, for future nuclear structure studies of refractory elements such as cobalt or nickel (atomic numbers $Z = 27$ and 28 respectively), of which it is expected that they may reveal much interesting structure information, the ISOL technique with a thick target is no longer suitable. Indeed, the high melting point of these elements makes it difficult to volatilise as well

as release them from a thick target. For such a situation, a technique based on thin targets is needed and the laser ion guide based on a gas cell to thermalise, neutralise and stop the recoiling nuclear reaction products combined with a laser beam to re-ionise them selectively, seems a good choice [53, 25].

However, in order to know whether the technique is suitable for ALTO, we need to answer the question as to what the ionisation rate is of the buffer gas by the primary electron beam and secondary charges? In other words, what is the ion-electron pair production rate in the gas cell? This is most important since the ionisation rate negatively affects the extraction efficiency of the laser ion guide whenever it becomes bigger than 10^{10} $s^{-1}cm^{-3}$ [23]. To answer this question, we built a code based on the Geant-4 toolkit to simulate the ionisation of the buffer gas. Furthermore, in a move towards the SPIRAL-2 project at GANIL, where fission of ^{238}U will be induced by neutrons produced in a carbon converter from a deuteron beam, we also wrote a Geant-4 code to simulate the production of neutrons, the neutron-induced fission and the energy deposit in a gas cell of similar dimensions as the proposed gas cell for ALTO. We likewise performed a simulation for the gas cell at Leuven to compare with published results [23]. This work is described in chapter 5.

In this work, we also briefly show the results of the photo-fission yield measurements at ALTO. The fission fragments were ionised in a hot plasma ion source, mass separated and detected by germanium and scintillator detectors. The measurements were carried out at masses 78 to 95, 117 to 144 and at mass 160. Finally, we summarise the first physics result from ALTO, during which a surface ion source with a tungsten ioniser was used to ionise selectively the neutron-rich gallium isotopes produced in the photo-fission of ^{238}U. A detailed description of the experiment and the observation of the β decay of these isotopes are presented in chapter 3.

Chapter 2

ISOL Technique and description of the ALTO project

2.1 Introduction

For studies of nuclei far from stability, it is often necessary to have intense, mass-separated radioactive ion beams (RIBs) uncontaminated by isobars from neighboring elements. In order to produce such beams, laboratories use one of two existing methods: ISOL (Isotope Separation On-line) and In-Flight methods. The schematic view of the ISOL and In-Flight techniques is shown in figure 2.1.

The ISOL technique was invented in Copenhagen over 50 years ago and eventually migrated to CERN where a suitable proton driver beam was available at the Synchro-Cyclotron [50]. The quick spread of the technique to many other laboratories has resulted in a large user community (for example ALTO at IPN Orsay, SPIRAL-1 at GANIL, TRIUMF, LOUVAIN-la-NEUVE...), which has assured the continued development of the method and the physics in the front-line of fundamental research and the application of the method to many applied sciences. The technique is today established

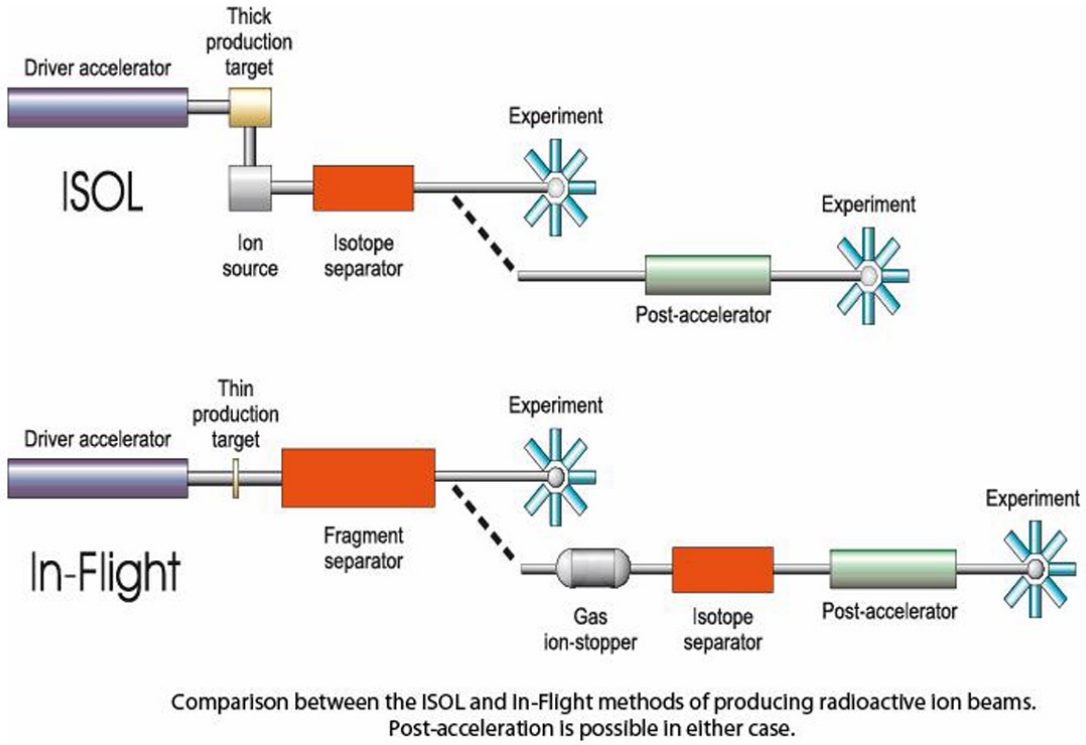

Figure 2.1: Schematic view of ISOL and In-Flight techniques [34].

as one of the main techniques for on-line production of high intensity and high quality isotopic beams. The thick targets used allow the production of unmatched high intensity radioactive beams. The fact that the ions are produced at rest makes it ideally suitable for low-energy experiments and for post- acceleration using well established accelerator techniques.

In the ISOL technique, the target, ion source and electromagnetic mass separation are very essential. Contrary to the In-Flight method, as referred to, the ISOL method has been associated with thick targets (the case of thin targets placed in a gas cell is discussed in section 5.1) such that the reaction products are thermalised in the target itself and diffuse out to an ion source for further acceleration and separation.

2.2 ISOL Technique

For an ISOL-type facility, a powerful method to produce the radioactive ion beams is by using fission reactions of actinide nuclei induced by thermal neutrons, fast neutrons, protons or photons, or by using spallation reactions (while the In-Flight method is mostly using fragmentation reactions). The great advantage of the thick targets is the large number of target atoms available for the production of the ions. The disadvantage with ISOL production in general is the difficulty to achieve high beam purity due to the many isobars of different elements produced simultaneously in the target. High beam purity can only be achieved with a combination of measures such as the right choice of target material, driver beam and ion source. Furthermore, refractory elements are in general difficult to produce due to the high temperatures required to make them volatile, see figure 2.2.

It is therefore crucial, when short-lived isotopes are produced in thick targets, to realize target and ion-source systems with good release properties and high efficiency. So in the ISOL technique, R&D studies of target and ion source are very important for optimization of production, selectivity and release of the isotopes of interest.

2.2.1 Target ion-source in the centre of ISOL technique

In the ISOL technique, the intensity of the separated radioactive beam of interest depends on many factors. It can be characterized as follows:

$$I = \phi.\sigma.N.\epsilon_{target}.\epsilon_{source}.\epsilon_{separ}.\epsilon_{det} \tag{2.1}$$

Here ϕ is the flux of the incoming beam, σ is the reaction cross section, N is the number of atoms in the target, ϵ_{target} is the element release efficiency from the target, ϵ_{source} is the efficiency of the ion source, ϵ_{separ} is the sepa-

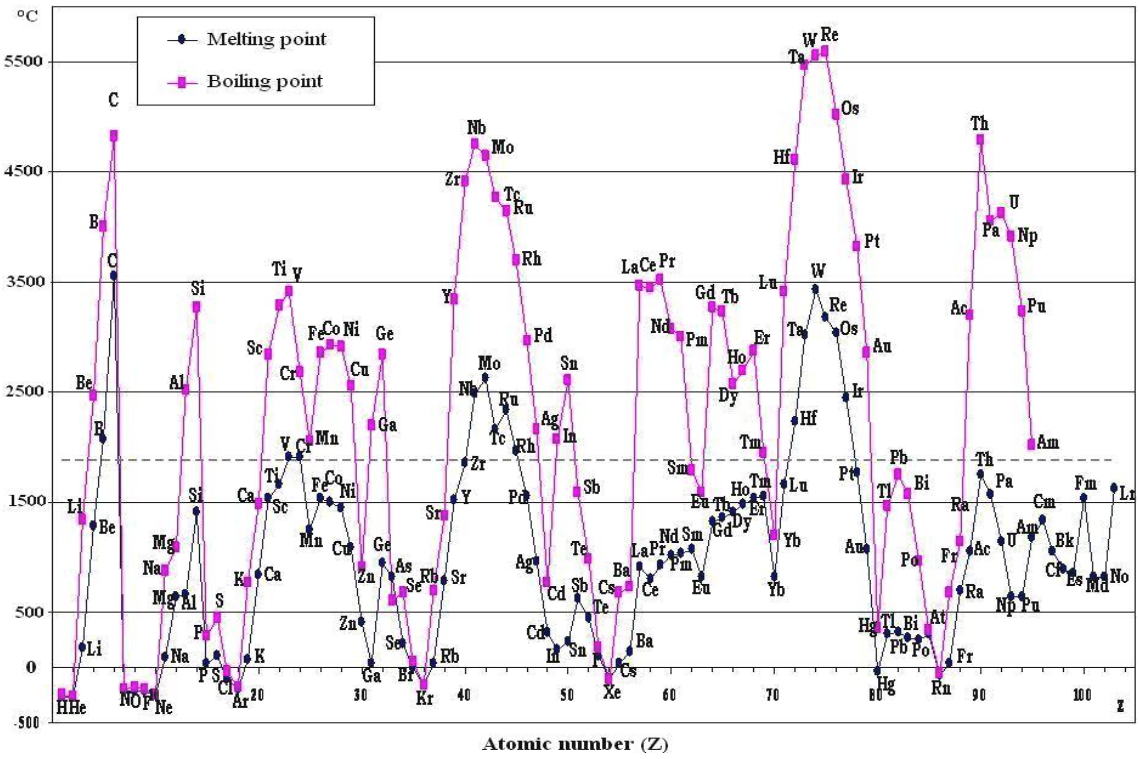

Figure 2.2: Boiling and melting point of elements

ration efficiency and ϵ_{det} is the efficiency of the detection system (see figure 2.3).

In the next sections, I am going to discuss the release from the target and the selectivity of the ion source.

The target: release of elements

Target-material selection begins by considering the physical, chemical, and thermal properties of the target material in relation to those of the product species. One of the principal problems lies in the availability of target materials that are sufficiently refractory so that they can be raised to the temperatures necessary for fast release of the product species without exces-

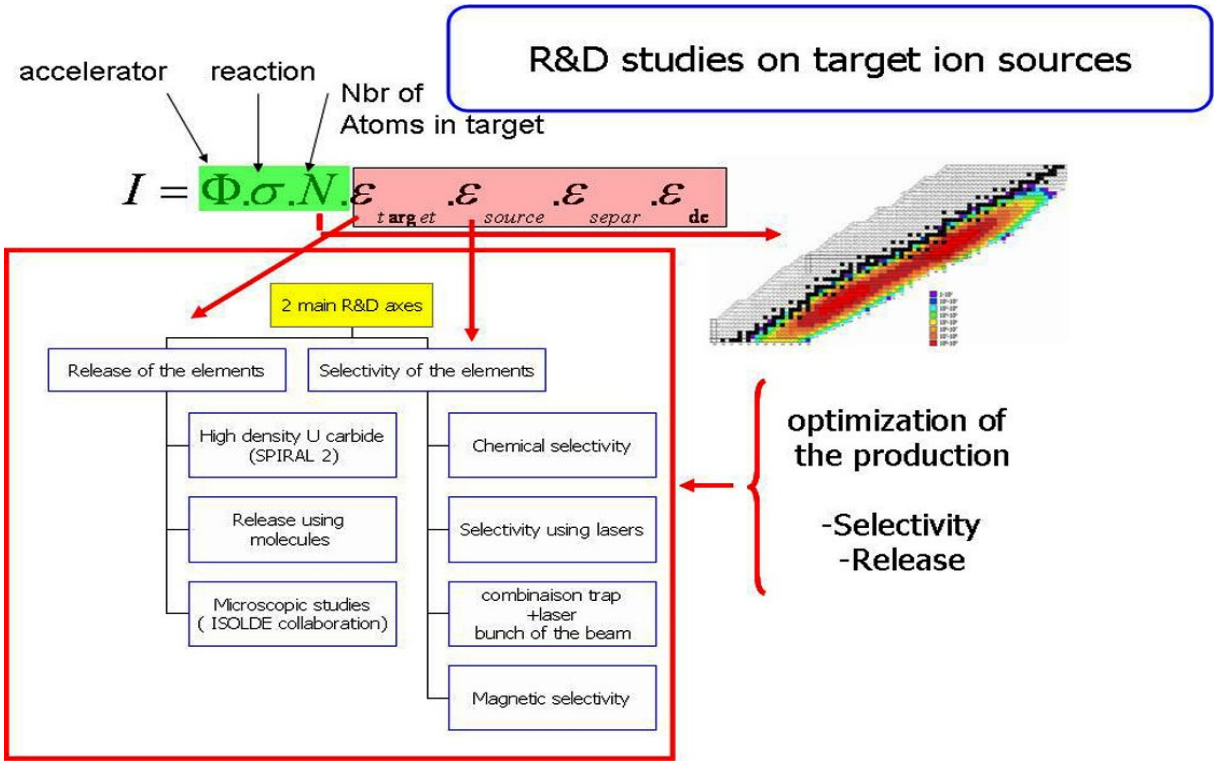

Figure 2.3: Target ion-source problematics [34]

sive vaporization or sublimation of the target itself. The choice of material is further restricted by the requirement that the radioactive species be easily diffused from the target material and readily volatilized for subsequent transport to the ionisation region of the source. Thus in the ideal case, the radioactive species should possess physical and chemical properties almost opposite to those of the target material itself. For release of the species of interest, the species should not form refractory compounds within the target material, should rapidly diffuse to the surface, and upon reaching the surface, the species should be readily desorbed. Obviously, for compound target materials, those with the highest percentage of the production nuclei are desirable in order to maximize the production rate of the species of interest.

One of the materials that can satisfy the mentioned criteria for production of neutron-rich radioactive species through fission is UC_x. By using this target, we can produce the species of interest from helium to neptunium (the latter through capture of an incident irradiating particle). The typical design of a target ion source is shown in figure 2.4, the fission target includes 148 pills of uranium carbide heated to 2200 °C for release of the elements [34].

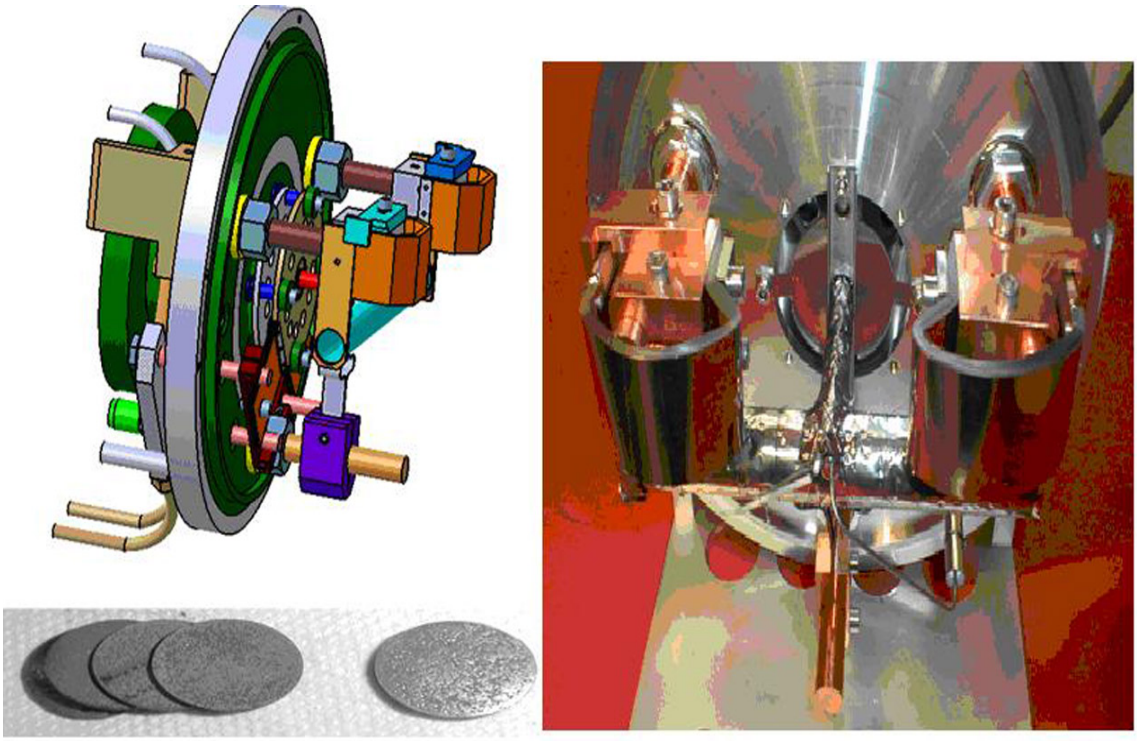

Figure 2.4: A typical design of the target coupled to the surface ion source [34].

The ion source: selectivity of the beams

- High-temperature plasma ion source

For isotopes of elements with ionisation potential $W_i > 7$ eV and for the creation of multiply charged ions, electron impact ionisation is mostly used [2]. The atoms or ions are bombarded by energetic electrons, thereby losing one or more of their outer electrons. In the plasma ion source, electron impact ionisation is used to ionise the atoms that are present in the gas phase inside the ion source. The electron flux is created by a discharge in a low-pressure environment. In this way plasma is produced in which the ions are confined, preventing them from wall collisions and neutralization. In general, plasma ion sources are not selective, since the energy spectrum of the electrons is broad and allows for the ionisation of virtually every element.

- Surface ion source

When an atom with low ionisation potential W_i hits the hot surface of a material with a high work function ϕ (e.g. noble metal), it has a high probability to give its valence electrons to the metal and get ionised (see figure 2.5). This process is called (positive) surface ionisation. An analogous process of negative surface ionisation exists for elements with high electron affinity which hit the hot surface of a material with low work function and get negatively ionised.

The single positive ionisation efficiency can be calculated with the Saha-Langmuir equation:

$$\epsilon_{surface} = \frac{1}{1 + \frac{g_0}{g_+} exp\left(\frac{W_i - \phi}{kT}\right)} \tag{2.2}$$

Here, g_0 and g_+ are the statistical weights of the atomic ground and ionic states, respectively, k is the Boltzmann constant and T is the temperature in Kelvin.

In practice, the positive surface ionisation source shows a high efficiency for elements which have a low ionisation potential when using high work

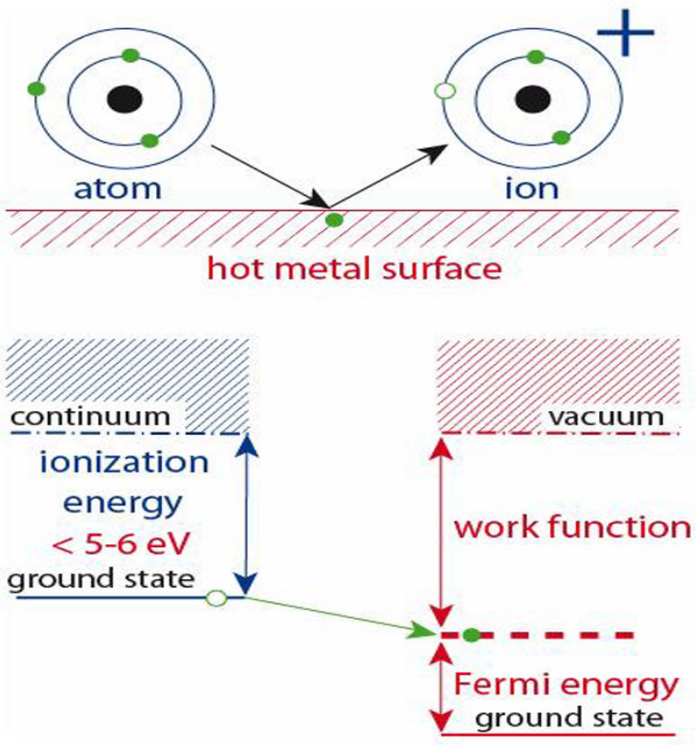

Figure 2.5: Surface ionisation principle [42].

function materials at high temperature ($\approx$ 2000°C) like Ta (ϕ = 4.1 eV), W (ϕ = 4.55 eV), Re (ϕ = 4.96 eV), Ir (ϕ = 5.27 eV), ... The efficiency of positive surface ionisation can be significantly enhanced when using a hot cavity in which a thermal plasma is created consisting of surface-ionised ions and thermionic electrons emitted from the cavity surface by heating. The tube and the inner space of the cavity close above the surface become slightly positive and the positive ions that are in the cavity are repelled. So they may be extracted from the cavity without wall collisions, or in other words, they will not recombine.

The positive surface ionisation source is selective if the neighbouring elements have a sufficiently higher ionisation potential. In particular, this ion

source results in high efficiency for alkalines which have the lowest ionisation potential as well as elements which have a little bit higher ionisation potential such as gallium, see figure 2.6.

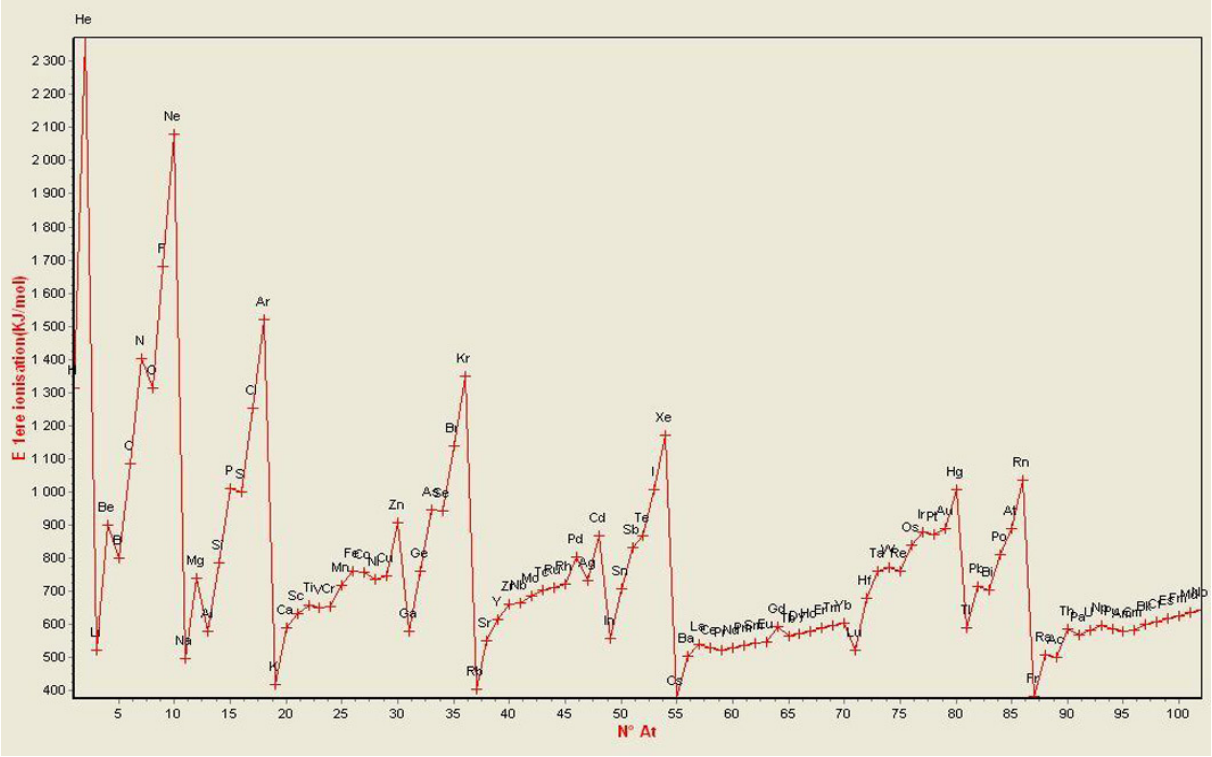

Figure 2.6: Ionisation potentials of the elements [34]

- Laser ion source

A method that has been successfully implemented at ISOL systems is resonant laser ionisation. For many metallic elements, the requirements of the ion source of an ISOL facility (efficiency, selectivity and rapidity) are ideally fulfilled by a resonance ionisation laser ion source (RILIS) [41]. Presently such ion sources have been used at the RIB facilities IRIS (Gatchina), ISOLDE (CERN), LISOL (Leuven), TRIUMF (Vancouver)... to provide beams with low isobaric contamination.

In a resonance ionisation laser ion source (RILIS) the valence electron is excited by resonant photo-absorption via several intermediate steps into the continuum, see figure 2.7. The position of the excited state is specific for each element. Tuning the laser wavelengths to this fingerprint provides an ionisation method with high intrinsic elemental selectivity.

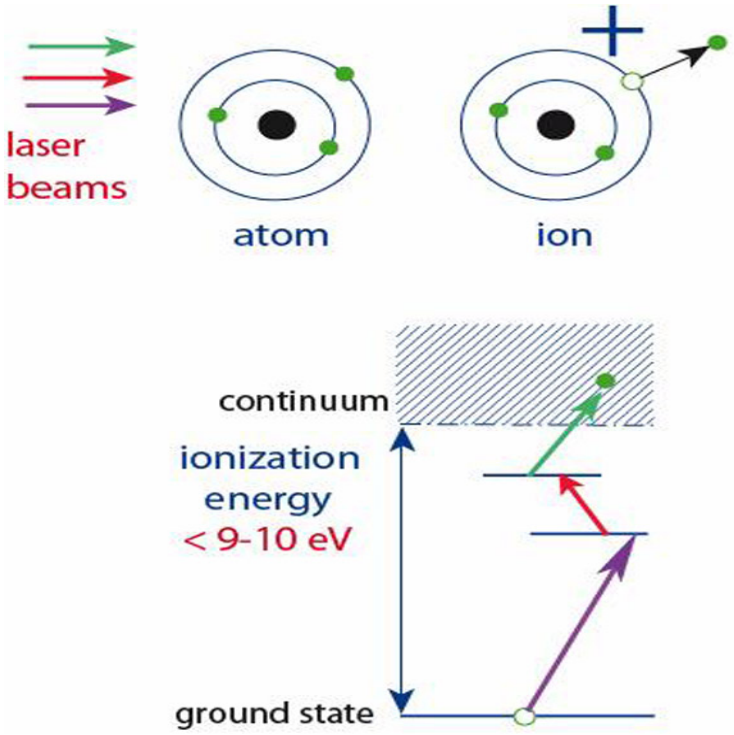

Figure 2.7: Schematic representation of resonant laser ionisation [41].

Resonance ionisation was already applied for many elements (see figure 2.8) [28, 29, 58].

However, for transitions to high-lying (> 6 eV) first excited states of non-metals, laser beams in the far ultraviolet ($\lambda < 200$ nm) are required. These can only be produced with low intensity and/or low duty cycle. Thus, these elements are less suitable for efficient laser ionisation.

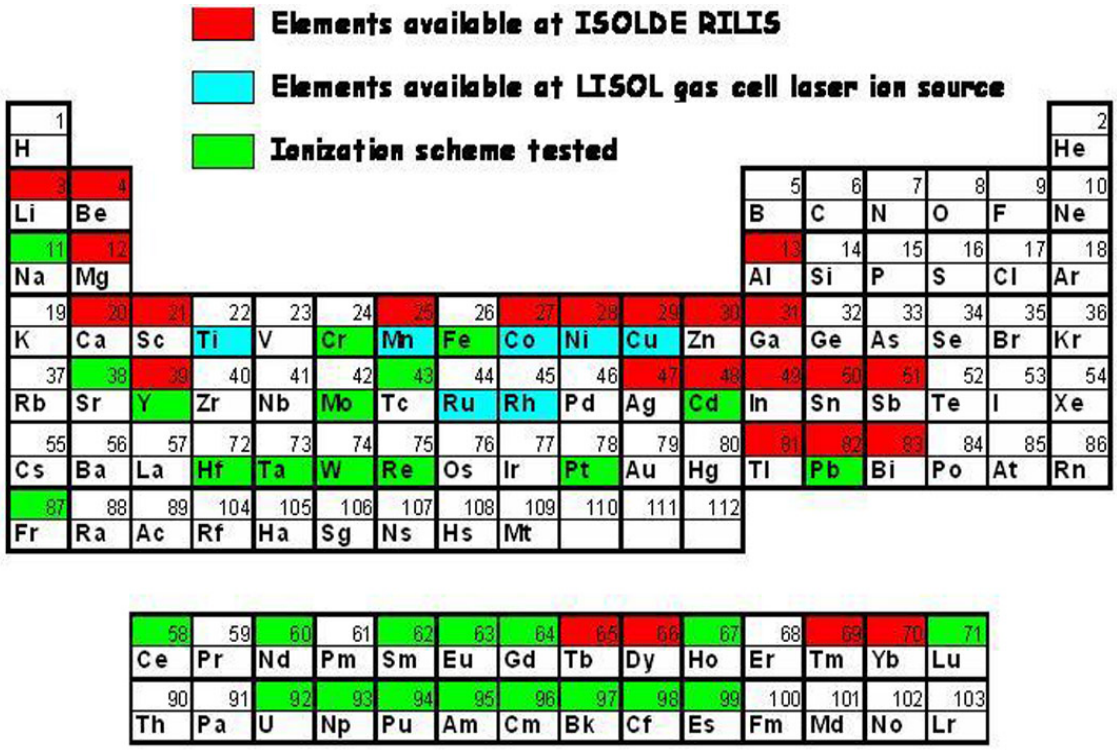

Figure 2.8: Elements that have been ionised with a laser ion source.

To achieve maximum ionisation efficiency, intense laser beams are used for excitation and ionisation. The laser beams need to have a sufficient overlap in time and space with the atomic beam of radio-isotopes. Since presently only pulsed lasers can provide sufficient beam power, the atoms have to be confined in the interaction region for a while. In order to store atoms, we can use a hot cavity with small outlet hole or a buffer gas. In the hot cavity that is commonly used, the average residence time of an atom is of the order of some 0.1 ms [41]. Thus, a laser system with a repetition rate of the order of 10 kHz is required to assure that each atom has a chance to interact with the laser beams. The simplest version of the ioniser cavity is identical to the ioniser tube of a surface ion source, like the Nb, Ta and W tubes which can

be well heated above 2000 °C. Thus, the delay in the target and ion source system is normally dominated by the target. Due to the high temperature of the ioniser cavity, most molecules are dissociated and the laser-ionised beam consists purely of atomic ions.

Unfortunately, the hot cavity acts simultaneously as a surface ioniser for elements with low ionisation potential, yielding an isobaric background. In order to suppress this contamination, ioniser cavities made from low work function materials (e.g. TaC and Y_2O_3) should be used [41].

However, it is necessary to consider that, before being ionised, the radioisotopes have to be released from the target. Thus, refractory elements could well be laser ionised when supplied as atomic beam, but they are practically not released from a thick ISOL target. To avoid such an undesired chemical selectivity of the target, it is better to use a buffer gas cell coupled to RILIS for refractory elements (see section 5.2).

2.3 Description of the ALTO Project

In this part, we are going to summarise the production experiment at the LPI machine of CERN and its results which are basic to build ALTO project. Also, a short description of the ALTO project will be presented.

2.3.1 The production experiment at the LPI machine

In order to study the feasibility of photo-fission at Orsay, a PARRNe-1 (Production d'Atomes Radioactifs Riches en Neutrons) the photo-fission experiment was carried out at CERN to investigate the production of neutron-rich radioactive noble gas isotopes by photo-fission [15] (see figure 2.9). The results of the experiment provided the information on the photo-fission yield of noble gas isotopes needed for the design of the ALTO project at Orsay.

In this experiment, an incident electron beam of 50 MeV was delivered by

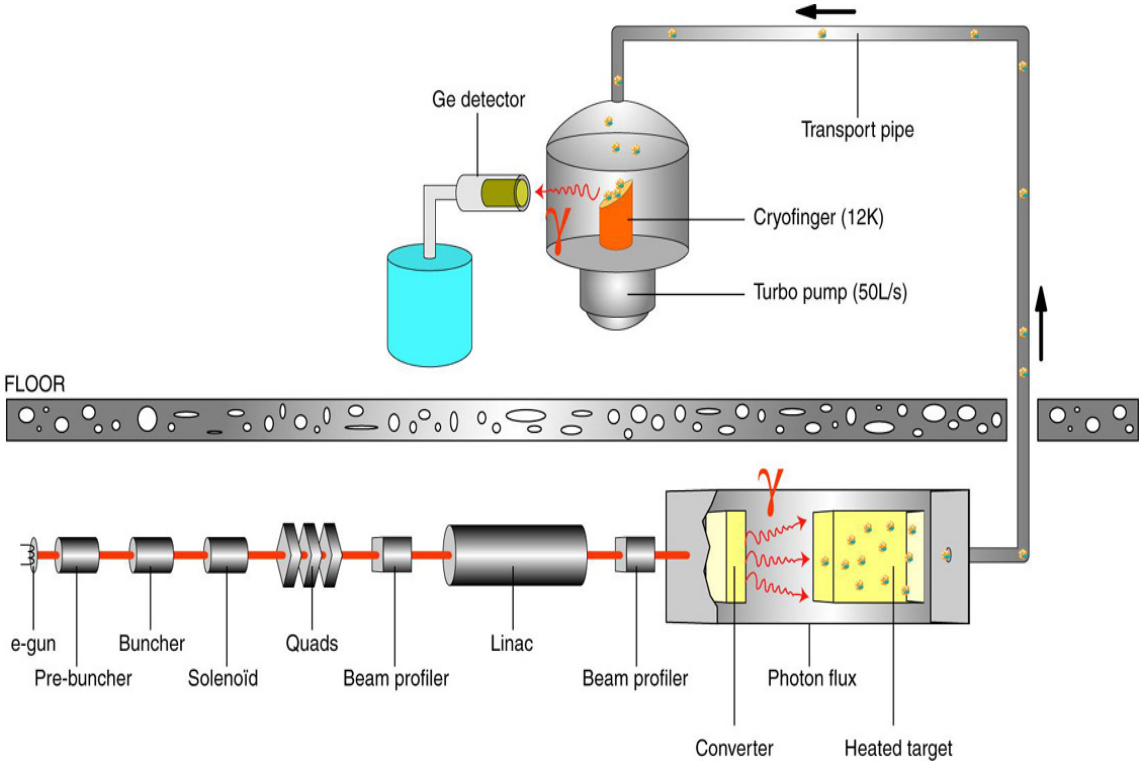

Figure 2.9: Schematic view of the experimental set-up at the LEP Injector Linac [15].

the LPI machine (LEP Pre-Injector). The 50 nA electron beam bombarded an intermediate tungsten converter with a thickness of 4 mm placed first at 4 cm and then at 8 cm from the UC_x target. The target (with a ratio of 4 carbon atoms for 1 uranium atom) included 67 UC_x pills of 14 mm diameter and placed in a 106 mm long graphite container. The target contains 23 g of ^{238}U and its density is 3.6 g/cm^3. A measurement without tungsten converter was also performed. In this case, a 10 nA primary electron beam bombarded directly the UC_x. During the experiment, the graphite container was heated at 1800 °C [15].

The obtained results (see figures 2.10, 2.11) for the production rates of the noble gas isotopes of Kr and Xe are compared with those obtained at KVI

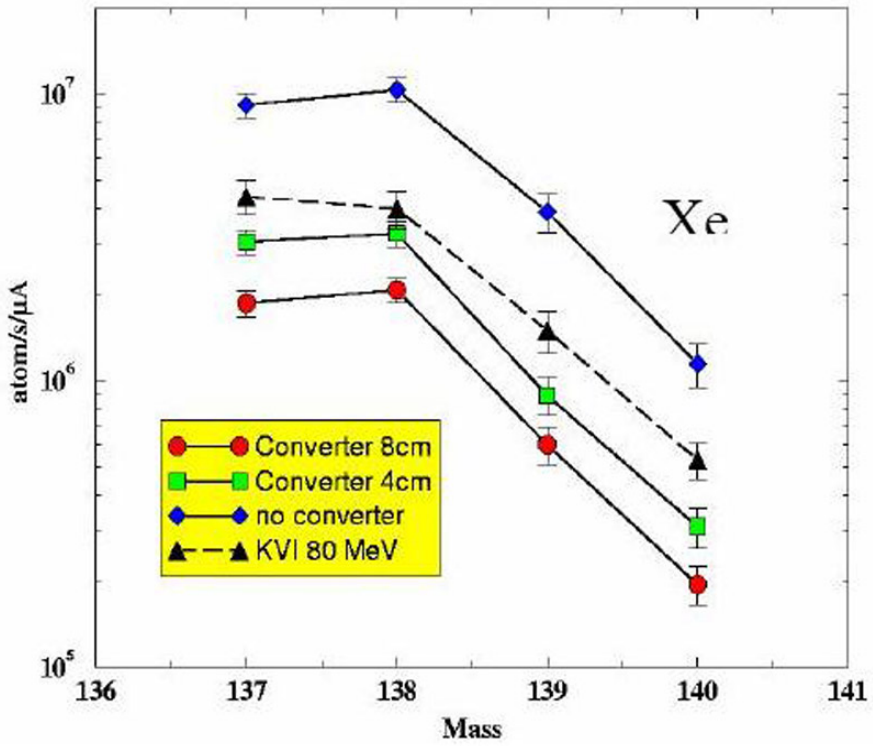

Figure 2.10: Production rates obtained for Xe isotopes at the LPI in different configurations compared with results obtained at KVI with deuterons of 80 MeV on a Be converter at 8 cm [15].

(Groningen) for the same experimental set-up and conditions (i.e. the same conditions for the release of the noble gases) but with a deuteron beam of 80 MeV (50 nA intensity). In the latter experiment, the deuteron-to-neutron converter was made of a 20 mm thick Be target and was placed at 8 cm from the UC_x target.

When the intermediate converter was used in the first experiment, fission was induced by the bremsstrahlung emitted from the tungsten converter. On the contrary, without intermediate converter, the bremsstrahlung produced from the UC_x itself will induce fission of the target. The obtained results first of all indicate that the production rate is higher when the target is placed

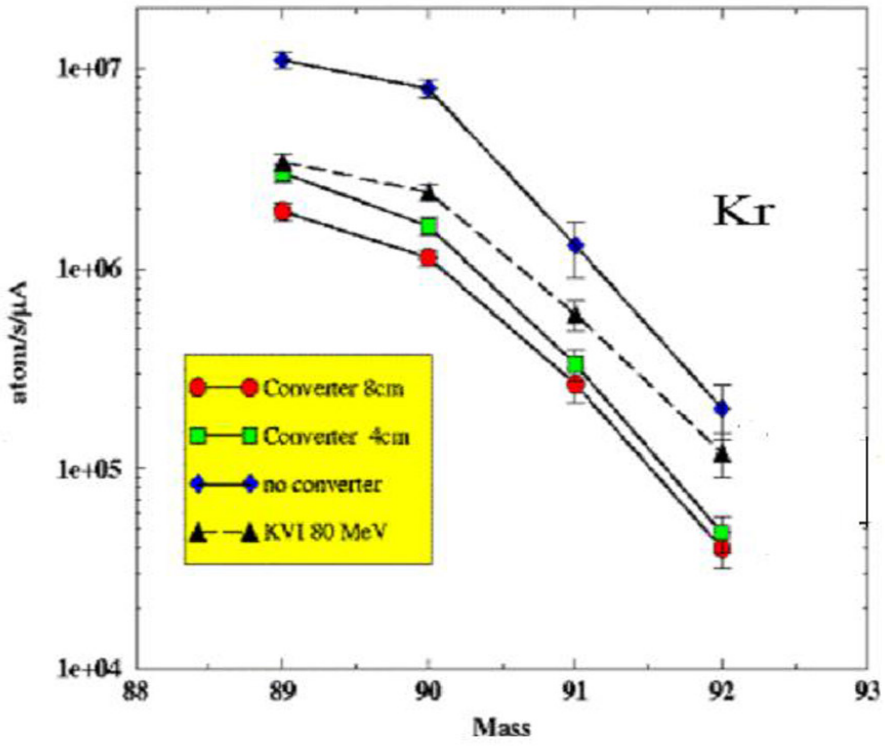

Figure 2.11: Production rates obtained for Kr isotopes at the LPI in different configurations compared with results obtained at KVI with deuterons of 80 MeV on a Be converter at 8 cm [15].

closer to the converter. This can be explained by the larger solid angle for a closer target. Without the converter, the production rate is even higher, because all of the bremsstrahlung produced in the target will travel through it and may induce fission. Finally, without converter, the production yields for noble gas isotopes are 3 times larger by photo-fission than by neutron-induced fission as measured at KVI. These results show that photo-fission is a promising method to produce intense neutron-rich ion beams.

The success of the photo-fission experiment is the basis of the ALTO project at IPN Orsay. The purpose of the project is to investigate necessary parameters for the construction of the ISOL-based SPIRAL-2 facility at

GANIL. Also, it opens the possibility to study neutron-rich nuclei produced in a thick actinide target by photo-fission.

2.3.2 Production of neutron-rich nuclei by photo-fission

The success of the PARRNe-1 experiment shows that photo-fission of ^{238}U could be an alternative to neutron-induced fission for the production of neutron-rich radioactive beams [13, 32].

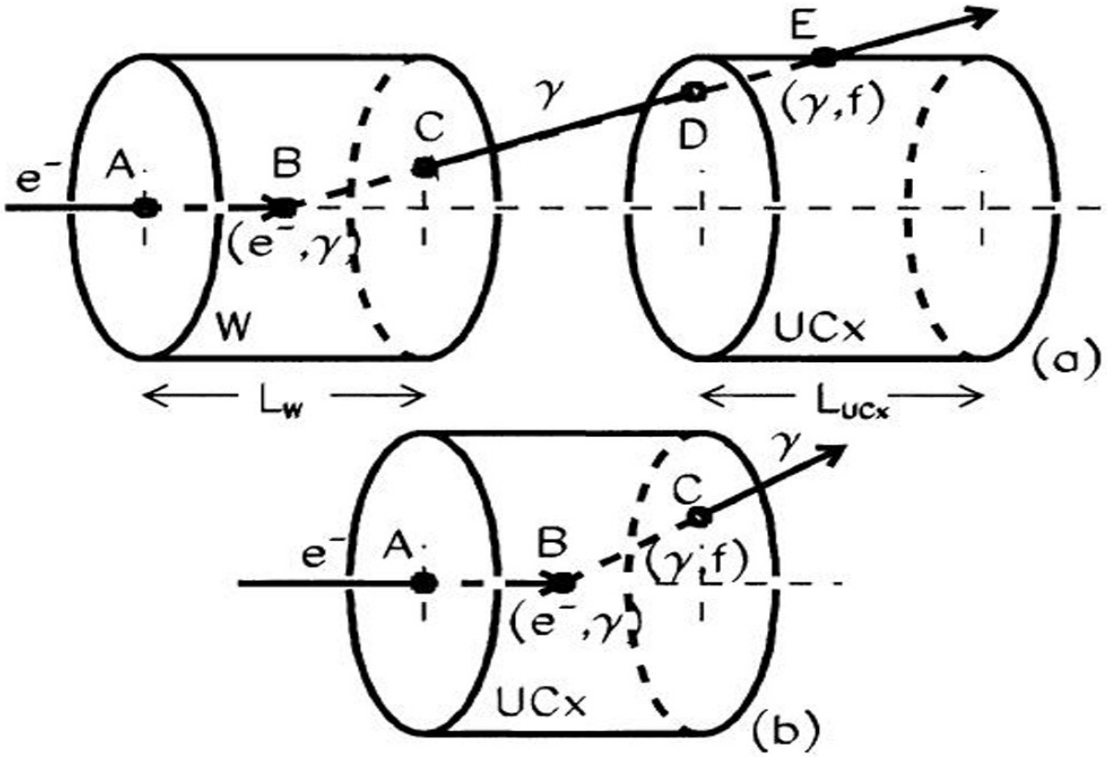

Figure 2.12: Two possible configurations of the ALTO project. (a) The intermediate converter produces bremsstrahlung radiation and these photons induce fission of ^{238}U. (b) The bremsstrahlung radiation is produced in the target itself.

With an electron driver, an electron beam can be focused onto a converter or onto a uranium carbide target directly to generate bremsstrahlung

radiation (see figure 2.12). Fission will be induced by those photons at the right energy to excite the Giant Dipole Resonance (GDR) of ^{238}U. Large fission event yields are thus expected at the GDR energy, which is around 15 MeV. At this energy the photo-fission cross section reaches 160 mb [16]. At that point the photo-electric and the Compton scattering cross sections are starting to fall off rapidly so the main contributions to γ absorption are e^+e^- pair production and the photonuclear reactions (γ, f), (γ, n) and $(\gamma, 2n)$. Although the absolute fission cross section is rather small (compared to 1 barn for neutron-induced fission), the fission yield can be enhanced by neutrons from the (γ, n) and $(\gamma, 2n)$ reactions. Therefore, in a thick target, photo-fission may be a rather interesting way of producing radioactive fission fragments.

Since for the ALTO project a linear accelerator delivers a 50 MeV electron beam, simulations of the bremsstrahlung spectra from a UC_x cylindrical target with a thickness of 30 g/cm^2 and a density of 3.6 g/cm^2, as well as those for 7.5 g/cm^2 and 30 g/cm^2 thick tungsten converters, for a 50 MeV incident electron beam, were carried out by means of the Fortran code FICEL [24]. Also, the photo-fission yields for several configurations (with a 30 g/cm^2, 7.5 g/cm^2 thick tungsten converter placed at 4 cm and 8 cm from the UC_x target, or without converter) as a function of the target thickness were calculated. The results are shown in figures 2.13, 2.14 and 2.15.

From these figures, we can see that the bremsstrahlung spectra in the forward direction corresponding to the tungsten converter and the UC_x target are quite the same. However, the simulated results are consistent with the experimental ones from the PARRNe-1 experiment at LPI in that the photo-fission yield is highest for the configuration without an intermediate converter, since no photons are lost for fission when the generation of the bremsstrahlung happens inside the target. In all configurations, the number of fission events increases with the thickness of the UC_x target and it reaches

saturation at a thickness of 8 cm.

2.3.3 The ALTO facility

The core of the ALTO facility is a linear accelerator that was obtained from CERN, the LEP (Large Electron-Positron collider) Pre-Injector, also known as LPI. This accelerator provides an electron beam with an energy of 50 MeV and nominal intensity of 10 μA. The schematic lay-out, given in figure 2.16, presents an overall view of the main components of the ALTO accelerator.

The electron beam from the ALTO accelerator is focused onto a thick target of uranium carbide (UC_x). The bremsstrahlung produced by the interaction of the incoming electrons and the target induces photo-fission. The fission fragments are ionised by an ion source (the accelerator is operated in combination with various types of ion source, including plasma, surface ionisation or laser ion sources, see section 2.2.1), mass-separated by a magnetic spectrometer and sent to the detection area. An overview of the ALTO facility is shown in figure 2.17. ALTO is expected to produce 10^{11} fissions per second at 10 μA beam current.

The ALTO accelerator was put in operation in December 2005 and the first photo-fission yield measurements with a uranium target were carried out in June 2006. For radioprotection issues, the intensity of the accelerated electron beam was limited to 100 nA instead of the 10 μA nominal current. These measurements are presented in the following chapter, along with the perspectives for physics experiments at ALTO.

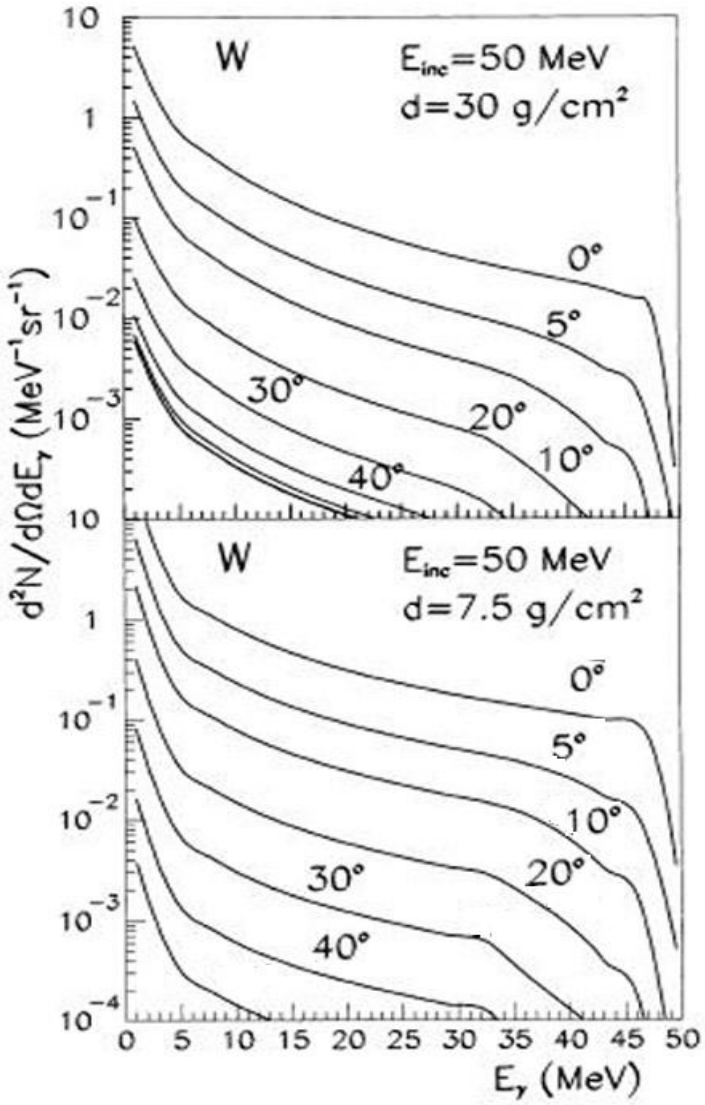

Figure 2.13: Angular and energy distributions of the bremsstrahlung emission per 50 MeV incident electron. The cylindrical converter is made from W. Top: the thickness is 30 g/cm^2. Bottom: the thickness is 7.5 g/cm^2 [24].

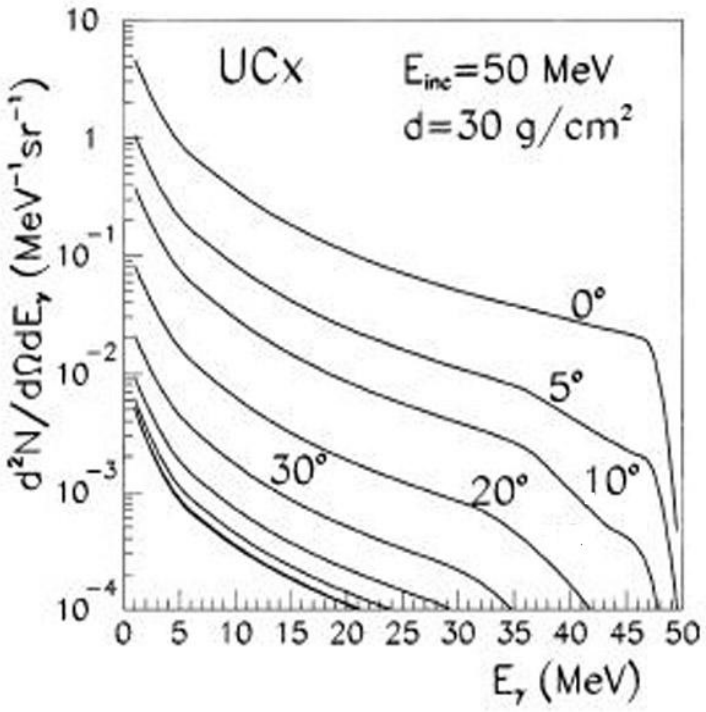

Figure 2.14: Angular and energy distributions of the bremsstrahlung emission per 50 MeV incident electron. The cylindrical converter is made from UC_x, the thickness is 30 g/cm^2 [24].

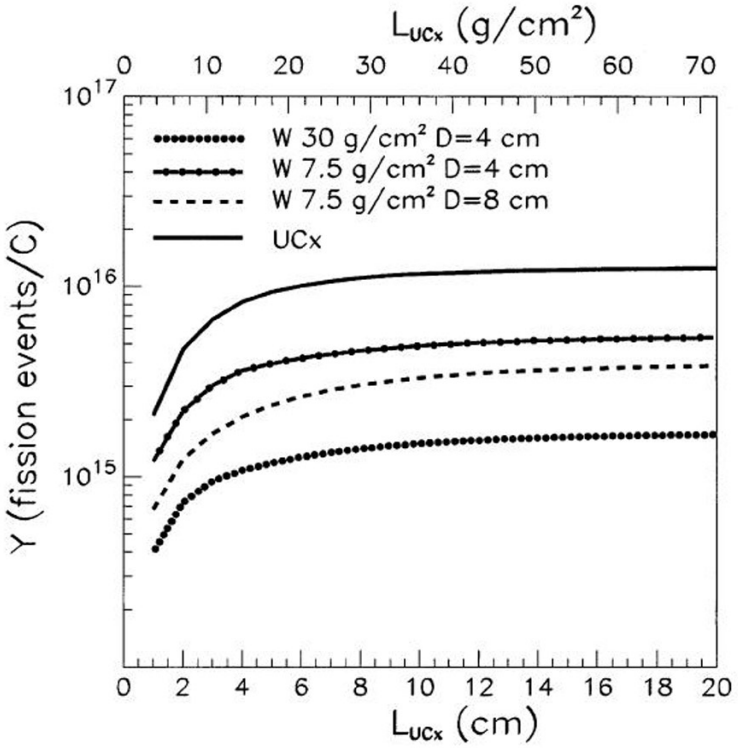

Figure 2.15: Number of fission events Y produced in the target per unit of 50 MeV incident electron current as function of target thickness. The radius of the UC_x target is 0.7 cm. Four configurations are considered: a 30 g/cm^2 W converter (approximately twice the electron range) was placed at 4 cm from the target, a 7.5 g/cm^2 W converter (approximately half the range) was placed at 4 and 8 cm from the target, and a configuration without converter [24].

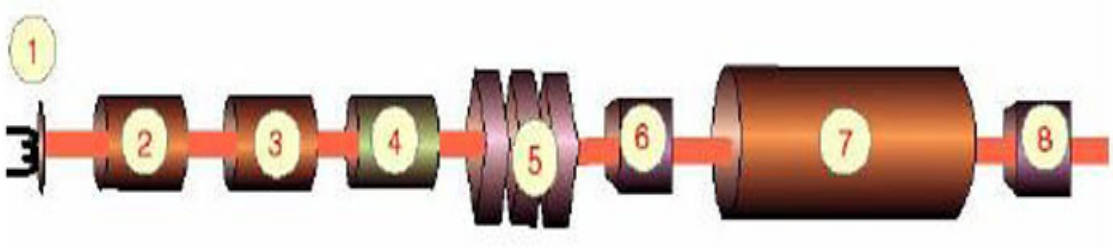

Figure 2.16: Overview of the ALTO accelerator. (1) Electron-gun, (2) pre-buncher, (3) buncher, (4) solenoid, (5) quadrupoles, (6) beam profiler, (7) acceleration section, (8) beam profiler [38].

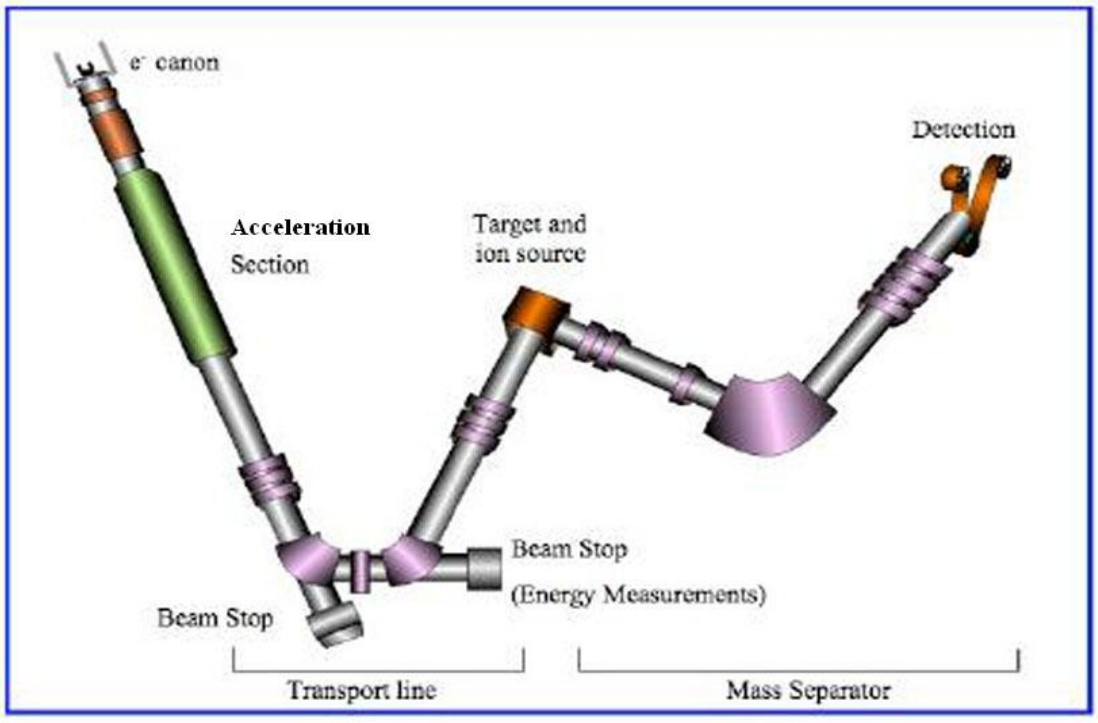

Figure 2.17: Overview of the ALTO facility [45].

Chapter 3

Production measurements and nuclear structure studies at ALTO

3.1 Production measurements at ALTO

3.1.1 Description of the experiment

In order to confirm the expected improvement of the production yields for photo-fission with the 50 MeV and 10 μA electron beam at ALTO with respect to the PARRNe setup that was based on the 26 MeV and 1 μA deuteron beam, an experiment dedicated to the measurement of the production yields was carried out with the electron current provisionally limited to 100 nA. The uranium carbide target was composed of 143 disks of 14 mm in diameter. It contained approximately 73 g of ^{238}U, which corresponds to a density of 3.36 g/cm^3. To allow for a fast release of the fission fragments, the UC_x target was heated to 2200 °C. The measurement was performed with a MK5 ISOLDE type hot plasma ion source.

As mentioned in the previous chapter (see section 2.3.1), with a 50 MeV electron beam of 10 nA hitting directly the UC_x target at LPI, one could observe a gain in the production yield of noble gases of a factor 3 times bigger

than with the 80 MeV deuteron beam of 50 nA on a beryllium converter at KVI (20 mm thick converter at 8 cm from the UC_x target). So extrapolating the results from LPI and KVI, we expected to obtain yields that are similar to what had been measured with the 1 μA deuteron beam during the PARRNe experimental program [45].

The measurements relied on the observation of the β decay of mass-separated isotopes that were implanted in a mylar tape at the collection point during a given time. Around the collection point we placed a 4π plastic scintillator and a germanium detector (see Fig. 3.1). The activity was periodically removed to avoid the build-up of background radiation. The cycle was repeated until enough statistics were accumulated for the characterisation of one isobaric chain and the collection time was optimised for each isobaric chain in order to enhance the activity of interest. The measurement was performed for the masses 78 to 95, 117 to 144 and at mass 160.

The data-acquisition system was based on a COMET-6X (Codage et Marquage En Temps) module, which allows to encode signals delivered by up to six detectors per module with a capacity to chain five modules together. With each amplitude that is encoded an absolute time information is associated with 400 ps resolution. From the triggerless data stream we can rebuild single γ spectra as well as β-γ coincidences.

3.1.2 Experimental production yields

The production yields were determined from the areas of the photo-electric absorption peaks of the characteristic γ rays emitted by the different isotopes. The γ lines were identified in β-γ coincident spectra. We use the following equation for the production rate ϕ:

$$\phi = \frac{N_d}{t_{coll} - \frac{1-e^{-\lambda t_{coll}}}{\lambda}} \tag{3.1}$$

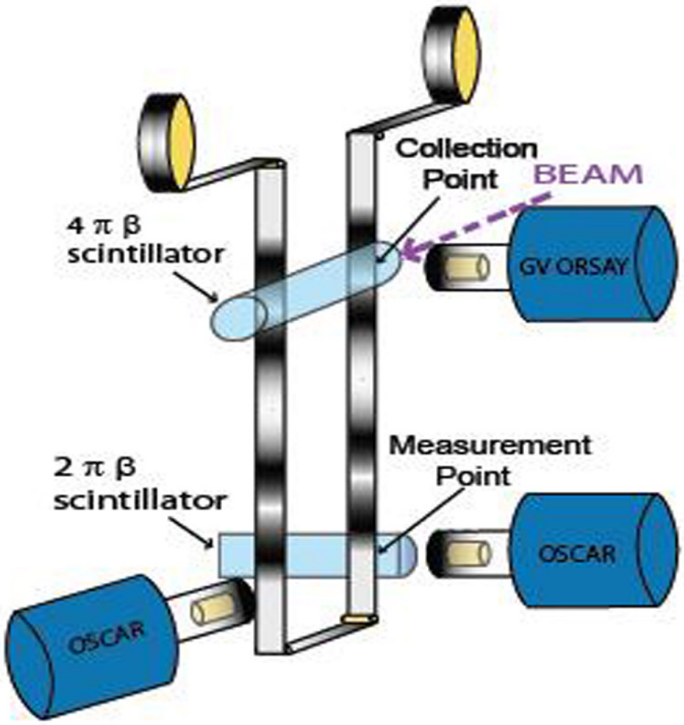

Figure 3.1: Experimental setup of the yield measurements [45].

Here, t_{coll} is the collection time in a measurement cycle, λ is the decay constant of the nucleus, and N_d is the number of disintegrations during n_{cy} cycles of measurement. It is given by:

$$N_d = \frac{A}{n_{cy}\tau\epsilon I_\gamma} \tag{3.2}$$

In this formula, A is the area of the γ line, $\tau = 0.9$ is a correction for the dead time of the electronics and the dat acquisition system, ϵ is the detection efficiency, and I_γ is the absolute intensity of the γ line taken from literature. The measurement of 47 isobaric chains was thus performed during the experiment.

In figure 3.2 we show the results for the production yields of the isotopic

krypton and xenon chains together with related measured and calculated data for comparison [45]. As we can see, the production yields obtained at ALTO are compatible with the yields measured at PARRNe for 1μA. We remind that the experiment was performed at an electron beam current of 100 nA. Therefore, at the nominal intensity of 10 μA, the ALTO yields should be a hundred times better than at PARRNe.

In figures 3.3 and 3.4, we plot the production yields for the isotopic chains of tin, indium, and iodine. Also, these results indicate that the production yields at ALTO for an electron beam current of 100 nA are close to the PARRNe rates [45].

3.2 Nuclear structure studies at ALTO

Once the production measurements were completed, the current of the electron beam was increased to 1μA. As such the photo-fission yield became sufficient for the observation of the β decay of ^{83,84}Ga.

3.2.1 The β decay of the nuclei ^{83,84}Ga

Experimental setup

For this experiment, a surface ion source with a tungsten transfer line instead of a hot plasma ion source was used for the first time at ALTO. From the results that were obtained during the production measurements, a total in-target photo-fission yield of 10^{10} per second was expected at 1μA. Although the ionisation efficiency for gallium in a surface ion source is lower than in a hot plasma ion source (0.7 % compared to 3 % as measured at ISOLDE, Cern [56]), the surface ion source delivers a better selectivity for the gallium beam (see chapter 4).

The detection setup can be summarised as follows. Around the collection point, clover and coaxial germanium detectors are mounted in close geometry.

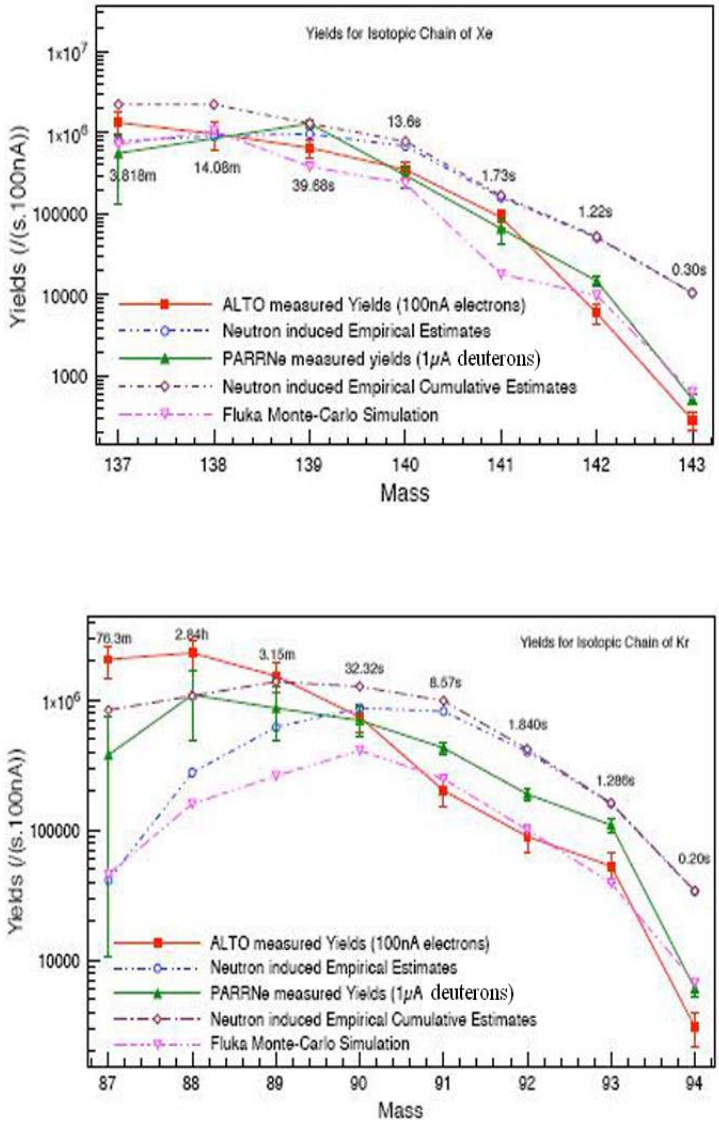

Figure 3.2: Production yields at ALTO for the isotopic xenon and krypton chains. The values for the ground-state half-lives are indicated.

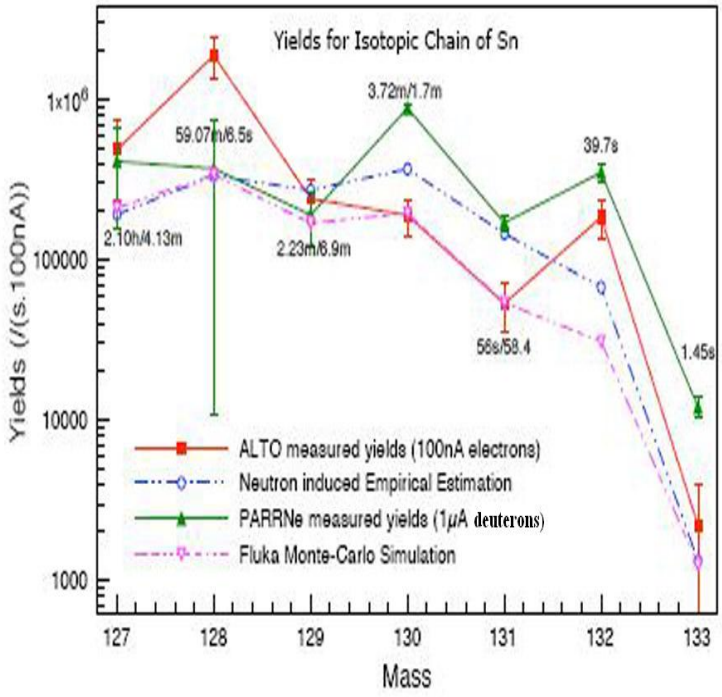

Figure 3.3: Production yields at ALTO for the isotopic tin chain. The values for the ground-and isomeric-state half-lives are indicated.

A plastic scintillator to detect β particles serves for the creation of the β-γ coincident spectrum. The detection system was calibrated with the standard ^{152}Eu source. The physical information is contained in three spectra: the γ spectrum gated by an event in the β detector, the time-energy matrix, and the γ-γ coincidence matrix gated by an event in the β detector. Further details of the experimental setup and the measurement method can be found in [46].

Experimental results

Decay of ^{82,83}*Ga*

The decay scheme of the ^{82}Ga is shown in figure 3.5. For the study of

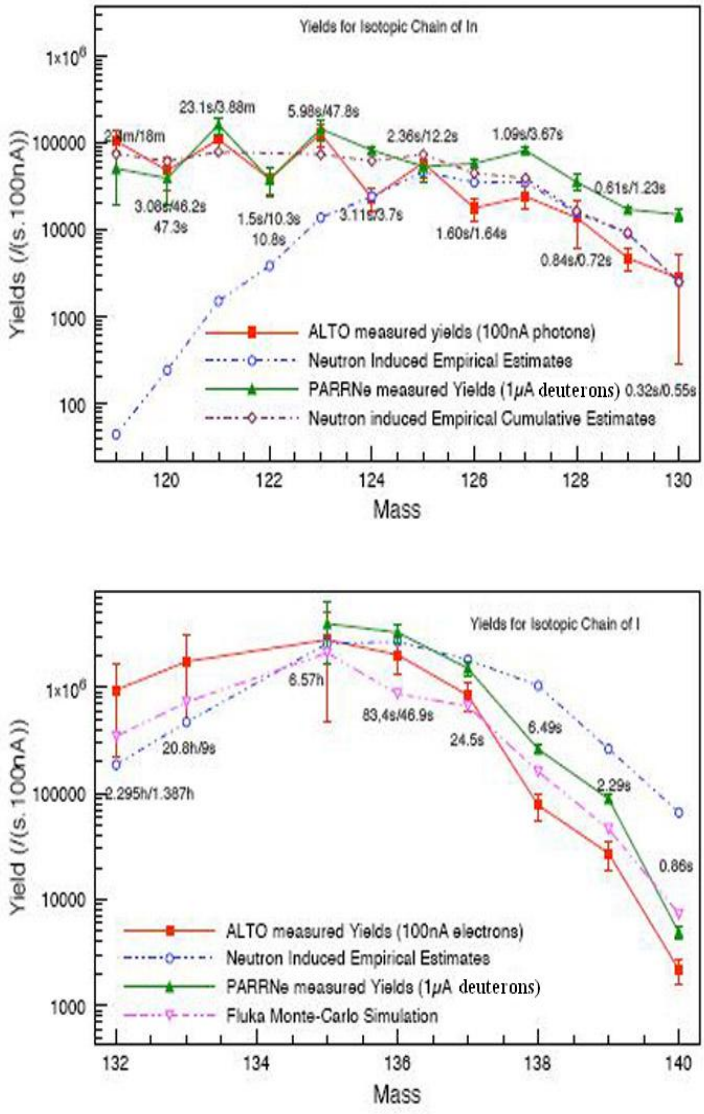

Figure 3.4: Production yields at ALTO for the isotopic indium and iodine chains. The values for the ground- and isomeric-state half-lives are indicated.

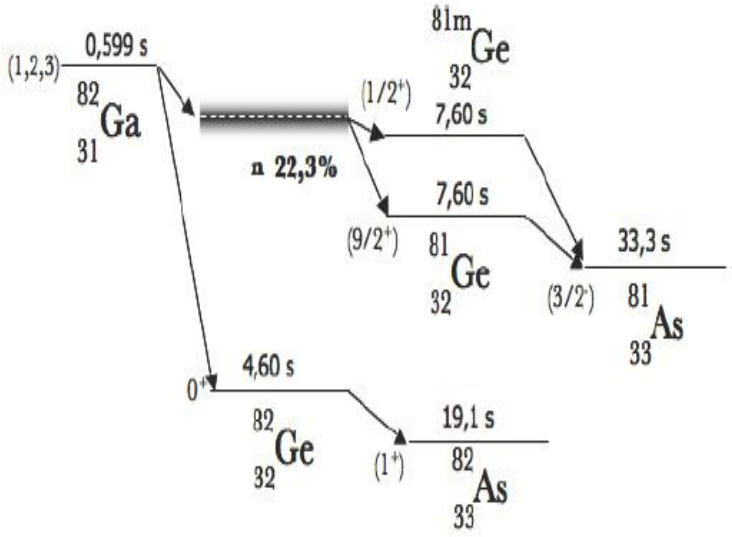

Figure 3.5: Scheme of the β and βn decay of $^{82}_{31}Ga_{51}$.

^{82}Ga, the tape did not move. Due to the selectivity of the surface ion source, we avoid most of the isobaric contamination and the activity in the tape is dominated by the decay of ^{82}Ga into ^{82}Ge and ^{81}Ge (by the βn path, see Fig. 3.5). The γ spectrum gated by a β event is presented in figure 3.6. All of the photo-peaks belong to masses 82 and 81. One deduces that an excellent beam of ^{82}Ga was ionised and extracted.

At mass 83 (the decay scheme is shown in Fig. 3.7), several cycles of collection and detection were used. A first cycle included 9 s collection and 1 s detection. Next we used a cycle with 2 s collection and 1 s detection. The γ spectrum gated by β-event with all statistics for all cycles is shown in figure 3.8. In a similar way as for mass 82, we find in this spectrum the known peaks for mass 83.

Decay of ^{84}Ga

At this mass, a cycle with 9 s collection and 1 s decay is used. The γ

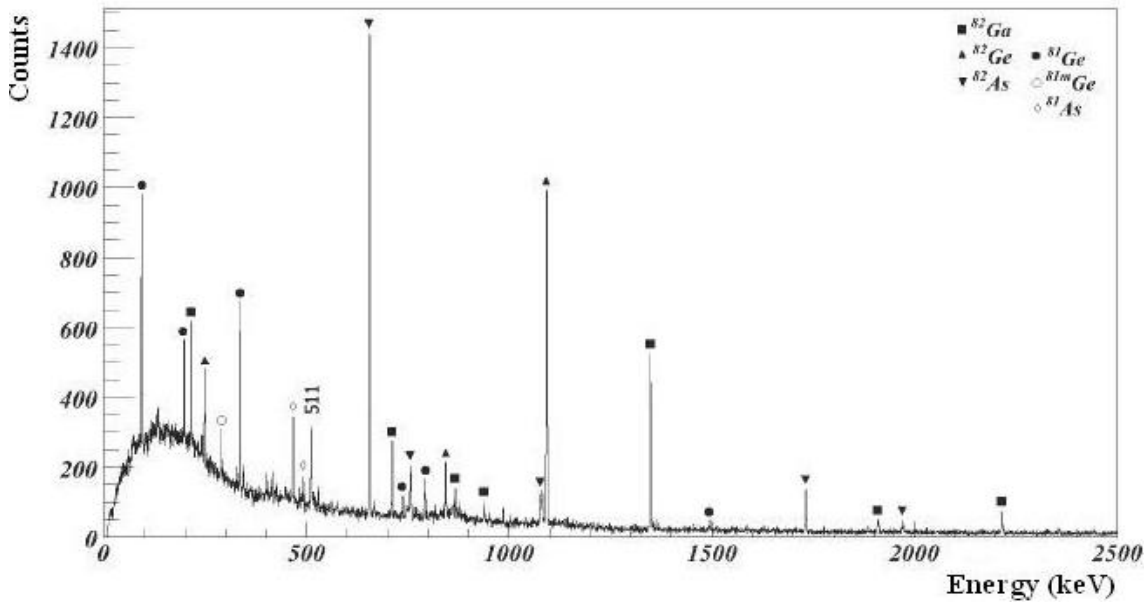

Figure 3.6: Gamma spectrum gated by β events obtained during the measurement of the β decay of ^{82}Ga.

spectrum gated by events in the β scintillator is reproduced in figure 3.9. Statistatics were accumulated for 15 hours of beam time at a current of 1 μA. We can see the presence of two peaks at 100.0 keV and 242.4 keV, known to stem from the β decay of ^{84}Ge [19]. We observe two peaks at 42.7 keV and 386.0 keV, previously not reported in the literature, which are in coincidence with the 100.0 keV line. We assign them to transitions between states of ^{84}As. We confirm the existence of two γ rays in the decay of ^{84}Ga, one at 624.3 keV and the other at 1046.1 keV, which were detected before at ISOLDE.

From these observations, we conclude that mass 84 was collected on the tape. However, we also observe characteristic γ rays of rubidium and its daughter isotopes. Indeed, the rubidium isotopes are produced in large amounts by photo-fission and since they belong to the chemical alkali group, they are strongly ionised (the ionisation efficiency approaches 80% [3]) and extracted from the source. They were stopped in the separator magnet but

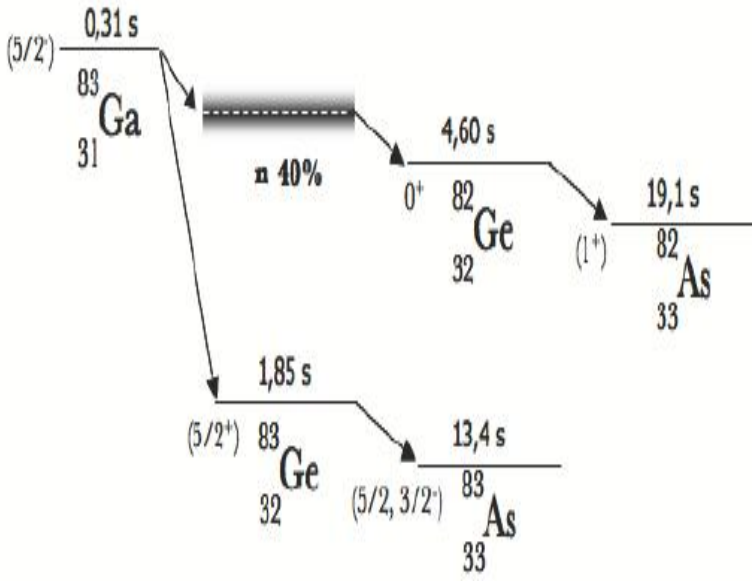

Figure 3.7: Scheme of the β and βn decay of $^{83}_{31}\mathrm{Ga}_{52}$

because of their huge production rate and insufficient shielding of the magnet their radiation could still reach the detectors and appear in the spectra as random coincidences with β events.

Furthermore, the βn decay path is known as a dominant channel in the decay of ^{84}Ga (the quoted branching ratio P_n varies between 47(10) % [60] and 70(15) % [20]). Therefore, γ rays from transitions in ^{83}Ge and its daughters must be present in the spectrum. As a matter of fact, the 306.3 keV line in ^{83}As and the 1238.2 keV line in ^{83}Ge are visible. In addition, a peak close to the energy of the $\frac{1}{2}^+$ excited state in ^{83}Ge at 280(20) keV, as observed in the ^{82}Ge(d,p) direct reaction, was expected to appear in the spectrum [18].

We assert the existence of a peak at 247.8 keV in our data, which was previously reported in the decay of ^{83}Ga and attributed to the $\frac{1}{2}^+ \rightarrow \frac{5}{2}^+_{gs}$ transition in ^{83}Ge [60].

The peak is among the most intense ones in our spectrum and its half-life

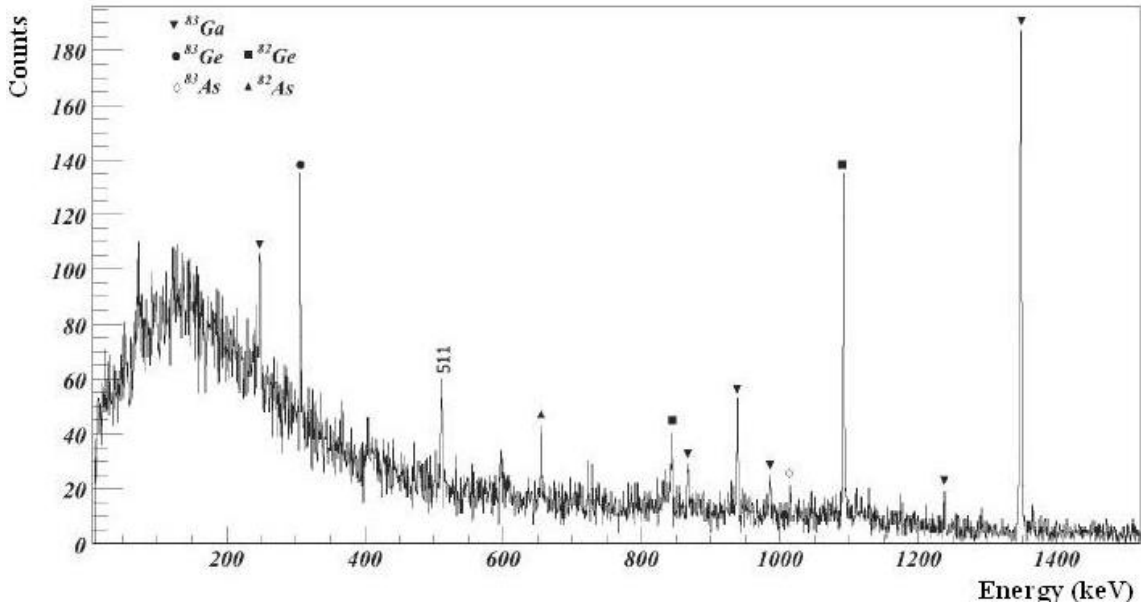

Figure 3.8: Gamma spectrum gated by β events obtained during the measurement of the β decay of ^{83}Ga.

was determined as 76(48) ms (see figure 3.10), which is consistent with the previously measured ^{84}Ga half-life of 85(10) ms. So for our experiment, this allows us to attribute the 247.8-keV peak to the βn activity of ^{84}Ga.

The list of the γ rays that are attributed to the decays of the ^{84}Ga population and its β and βn daughter populations is reported in table 3.1. All assignments are in good agreement with results obtained at other laboratories with different production and identification techniques except the line at 1046.1 keV, for which we need to discuss in detail the γ activity balance.

Firstly, we start from the assumption that there is a unique β-decaying state in ^{84}Ga (see figure 3.11). From the observed intensity of the 247.8 keV transition in ^{83}Ge and the P_n branching value from literature, we can calculate the production ϕ of the ^{84}Ga population. Based on the obtained ϕ value, the expected intensity I_{242} of the 242.4 keV peak in ^{84}As can be computed. With $P_n = 70(15)$ % [20] we find $I_{242} = 5(2)$ and with $P_n = 47(10)$

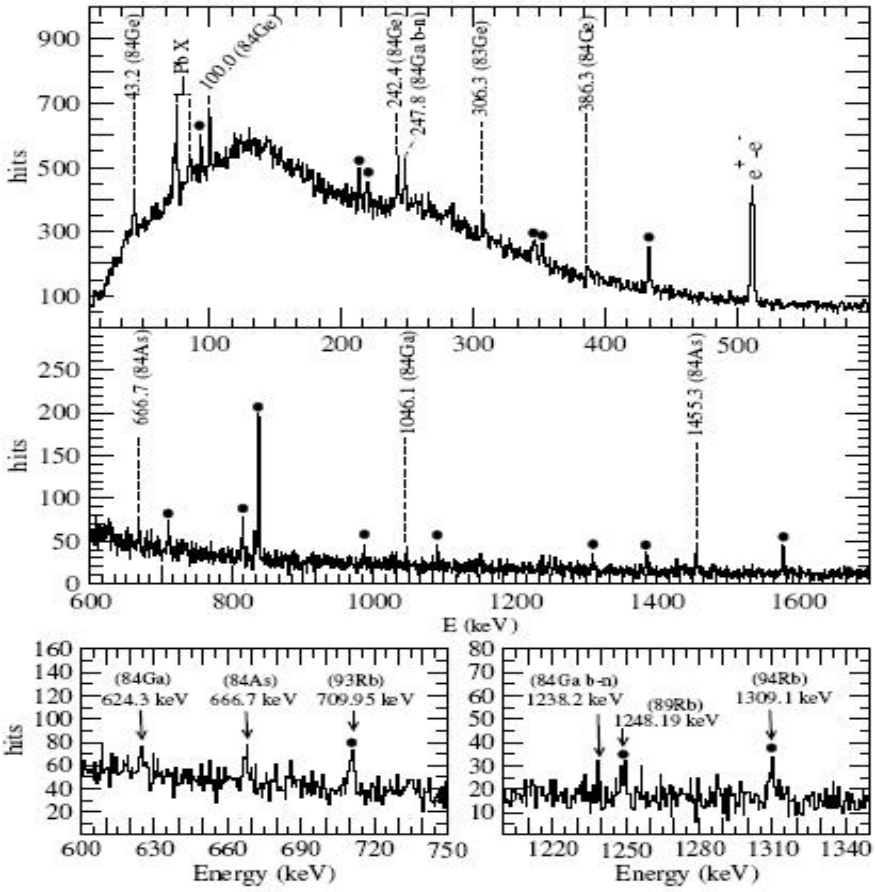

Figure 3.9: Upper part: β-gated γ spectrum recorded at mass 84. Peaks marked with dots correspond to the decay of $^{89-96}$Rb stopped in the mass separator. Lower part: Zoom of the spectrum for the 600-750 keV and 1200-1350 keV energy ranges [44].

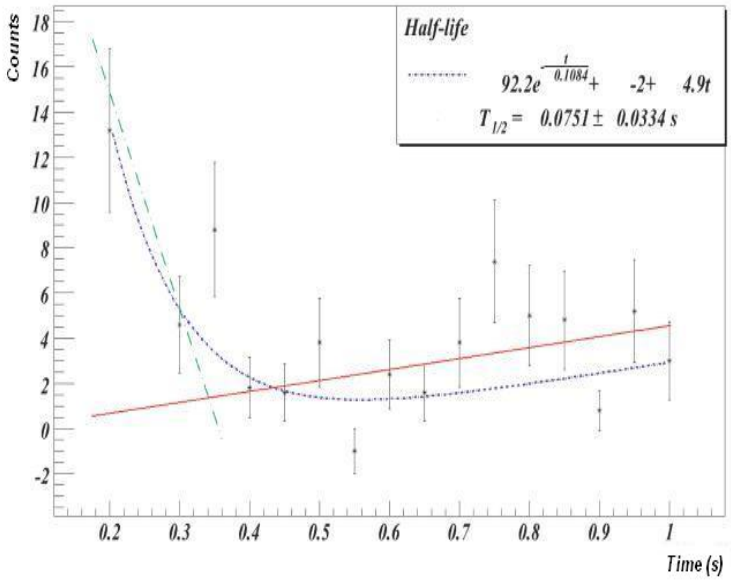

Figure 3.10: Number of events in the 247.8-keV peak during the 1-s decay time of the tape cycle. The solid line represents background from the focal plane.

% [60], $I_{242} = 13(6)$. The intensity extracted from our data is $I_{242} = 92(7)$. Furthermore, a clear unbalance in the γ intensities is observed in our spectra: the intensity of the 624.3 keV line in ^{84}Ge is rather weak but the intensities of the 100.0 keV and 242.4 keV transitions in ^{84}As and the 247.8 keV transition in ^{83}Ge are rather high, for instance $I_{624}/I_{248} = 38/100$. In the data taken at ISOLDE [40], the intensities of the 624.3 keV and 247.8 keV transitions are equal. Also, in the $A = 84$ spectra from ISOLDE, an 866 keV transition is clearly observed, which was attributed by the PARRNe collaboration to the $\frac{7}{2}^+ \rightarrow \frac{5}{2}^+_{gs}$ transition in ^{83}Ge [26].

The preceding arguments appear at odds. If ^{84}Ga were of high spin then it would feed, after neutron emission, the $\frac{5}{2}^+$ ground state of ^{83}Ge rather than the $\frac{1}{2}^+$ excited level. The absolute intensity of the 247.8 keV transition would be small and if it were of the order of some percent one could explain

Table 3.1: List of main γ lines observed in ^{84}Ga β and βn decay in this experiment.

Energy (keV)	Rel. int.	Attribution	Notes
42.7(3)	81(3)	^{84}Ge β	ALTO
100.0(3)	79(5)	^{84}Ge β	
242.4(3)	92(7)	^{84}Ge β	
247.8(3)	100	^{84}Ga βn	
306.3(3)	78(6)	^{83}Ge β	
386.0(5)	53(5)	^{84}Ge β	ALTO
624.3(7)	38(5)	^{84}Ga β	
666.7(7)	50(6)	^{84}As β	
1046.1(7)		^{84}Ga βn	
	42(6)	^{84}Ga β	ALTO
1238.2(7)	30(5)	^{84}Ga βn	
1455.3(7)	83(9)	^{84}As β	

the I_{242} intensity mismatch. The weak feeding of the 624.3 keV line, on the other hand, points to a low-spin structure in ^{84}Ga that would bypass the 2^+ level in ^{84}Ge and proceed directly to the ground state. Also the absence of the 866 keV transition at ALTO would be natural if one puts forward a low-spin β-decaying state.

To explain these facts it is proposed that there exist two β-decaying states in ^{84}Ga: one with low spin, dominant at ALTO, which would feed primarily the ^{84}Ge ground state, and a second, more intensely produced at ISOLDE, of spin $I \geq 3$ and contributing most of the intensity of the 624.3 keV $2^+ \rightarrow 0^+_{gs}$ transition in ^{84}Ge (see figure 3.12).

Finally, in our experiment, we observe a weak 1046.1 keV transition with about the same intensity as the 624.3 keV line. It is not observed at other masses. We may assume four possible origins for it, these are:

1. β decay of the low-spin state in ^{84}Ga;

2. β-n decay of the low-spin state in ^{84}Ga;

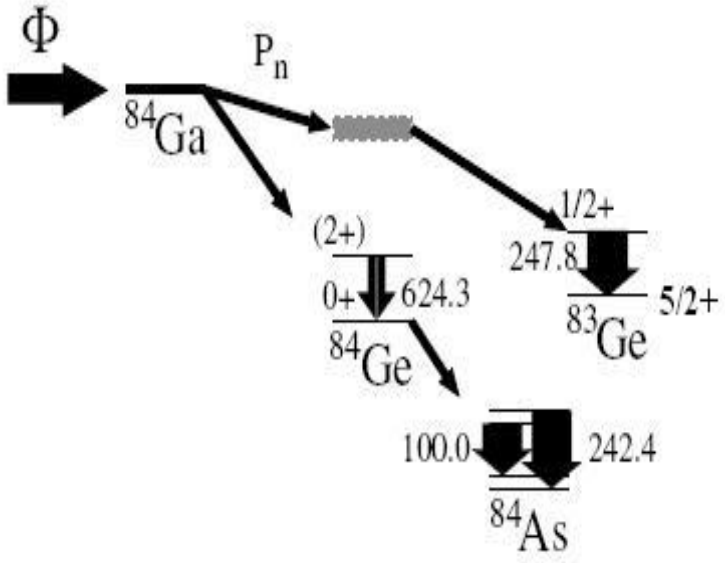

Figure 3.11: Decay paths for the hypothesis of a unique β-decaying state in ^{84}Ga [44].

3. β decay of the high-spin state in ^{84}Ga;

4. β-n decay of the high-spin state in ^{84}Ga.

We evaluate the individual cases:

1. β decay of the low-spin state in ^{84}Ga: The 1046.1 keV transition would, for instance, de-excite a second 2^+ state to the ground state in ^{84}Ge. However, unlike the 624.3 keV $2^+ \rightarrow 0^+_{gs}$ transition, such a γ line was not observed in the βn decay of ^{85}Ga at ISOLDE.

2. β-n decay of the low-spin state in ^{84}Ga: Considering that no 1046.1 keV peak was observed in a former ^{83}Ge decay experiment at PARRNe [26], the 1046.1 keV transition could instead connect a second $\frac{1}{2}^+$ state to the ground state in ^{83}Ge. It would then have been seen in the $A = 84$ spectra of the present experiment in the same way the 247.8 keV βn peak was seen. We measure an intensity of the 1046.1 keV line that is a factor of two lower

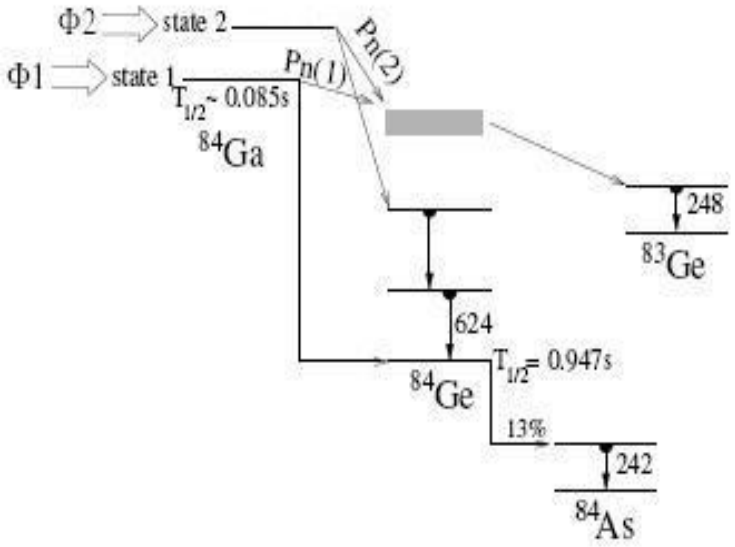

Figure 3.12: Decay paths for the hypothesis of two β-decaying states in ^{84}Ga [44].

than for the 247.8 keV line.

3. β decay of the high-spin state in ^{84}Ga: The 1046.1 peak would belong to the ^{84}Ge level scheme. Since it shows the same relative intensity as the 624.3 keV peak, we could propose to attribute it to the $4^+ \rightarrow 2^+$ transition in ^{84}Ge.

4. β-n decay of the high-spin state in ^{84}Ga: Again considering that no 1046.1 keV peak was observed in the former ^{83}Ge PARRNe experiment, the 1046.1 keV transition could instead connect a high-spin state to the $\frac{5}{2}^+$ ground state in ^{83}Ge. It would possibly be connected to the $\frac{7}{2}^+$ state at 866 keV in ^{83}Ge.

If the 1046.1 keV transition would be fed by the high-spin state in ^{84}Ge, and since both the 1046.1 keV and 624.3 keV lines are seen rather weakly, it would imply that the high-spin β-decaying state is much less produced at ALTO than the low-spin state.

3.3 Conclusion

In this chapter we have shown that the available theoretical predictions as well as the production yield measurements lead us to the conclusion that photo-fission is a viable alternative to neutron-induced fission for the production and study of neutron-rich isotopes. At ALTO, once the full nominal current is reached (10 μA), we are able to obtain radioactive ion beam intensities that are 100 times bigger than the ones achieved at PARRNe. So we can stipulate that the arrival of the ALTO accelerator opens a new opportunity to study exotic nuclei at Orsay. The exploratory experiment that took place at a current of 1 μA demonstrates that the $^{82,83,84}Ga$ isotopes can be produced at ALTO by combining the photo-fission with a surface ion source. From this experiment, we propose moreover the existence of two β-decaying states in the nucleus ^{84}Ga.

Chapter 4

New Surface-Ionisation Source at the ALTO Project

4.1 Theoretical basics

In order to study the nuclear structure of the neutron-rich germanium isotopes at ALTO via the β-decay of the neutron-rich gallium mother isotopes, it is necessary to be able to produce a highly intense and pure gallium beam. To obtain such a beam, we use the ISOL technique for fissioning ^{238}U in a thick UC_x target (see section 2.2.1). In this approach, the ion source plays a key role and for gallium isotopes the positive surface ion source is a good candidate because the ionisation potential of the neighbouring elements is sufficiently higher than its own one (see figure 2.6). Hence, for our case, the surface ion source can provide us with high selectivity. The highest efficiency will be obtained when refractory metals with a high work function are chosen as ioniser cavity. High work function materials include [59]:

1. Oxygenated surfaces, e.g. WO_x.

2. High work function faces of single crystals, e.g. the (110) face of W reported as 7 or 8 eV.

3. High work function metals, e.g. Re, Os, Ir, Pt.

However, oxygenated surfaces pose several problems. One of these is the enhanced emission of inherent impurity ions from the ioniser surface, especially alkalis. There may also be a chemical reaction between the oxygen and the element being ionised, e.g. Al or Ga at the surface, resulting in the gradual deposit of an oxide, e.g. Ga_2O_3, on the ioniser surface, provoking the ultimate failure of the ioniser. Moreover, the oxygen may react in a deleterious way with other components of the ion source.

On the other hand, single crystals pose the problem of obtaining single crystal faces of large area and maintaining them at the high operating temperatures that are needed for surface ionisation.

Because of the mentioned disadvantages, the use of high work function metals is the most suitable solution. Among these, the highest work function metal, Pt ($\phi = 5.65$ eV), has too low a melting point (1768 °C) and it cannot be used in the high-temperature environment of the ion source. The next highest work function metal, Ir ($\phi = 5.27$ eV), has a melting point of 2466 °C and it can be used well if we limit the temperature to 2000 °C. The element Re ($\phi = 4.96$ eV) has a melting point of 3180 °C, which is well adapted to the high temperatures of the ion source.

For gallium, the ground-state electron configuration is $^2P_{1/2}$, hence the statistical weights of the atomic ground and ionic states g_0 and g_+, which count the number of spin states, are 2 and 1, respectively. Its ionisation potential being I = 5.99 eV, the single surface ionisation efficiencies against W, Re, and Ir surfaces depend on the surface temperature and they are computed by using formula 2.2 and shown in figure 4.1. From the figure, we can see that the ionisation efficiency for gallium is 140 times larger when using rhenium rather than tungsten and this value grows to 875 when iridium is used. Also, an iridium surface at 2000 °C can give us the same efficiency as a rhenium surface at 2800 °C.

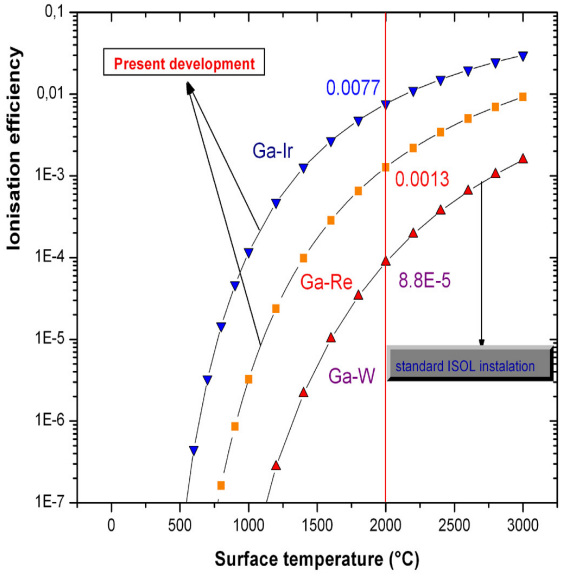

Figure 4.1: Surface ionisation efficiencies of Ga for W, Re and Ir ionisers as a function of cavity temperature.

In our off-line experiments, we shall test the surface ionisation efficiency of gallium by using a cylindrical cavity that is made of rhenium with a coating of 10 μm of iridium. The coating was performed by chemical vapour deposition (CVD, see appendix A). Some pictures of the coated surface of the Ir-Re tube obtained by secondary electron emission as well as backscattering from a scanning electron microscope are shown in figure 4.2.

4.2 Surface ionisation in a hot cavity

In a hot cavity where the area of the extraction orifice is small compared to the inner surface of cavity, the observed ionisation efficiency is many orders of magnitude higher than the prediction of the Saha-Langmuir equation. This efficiency can be evaluated by the expression [41]

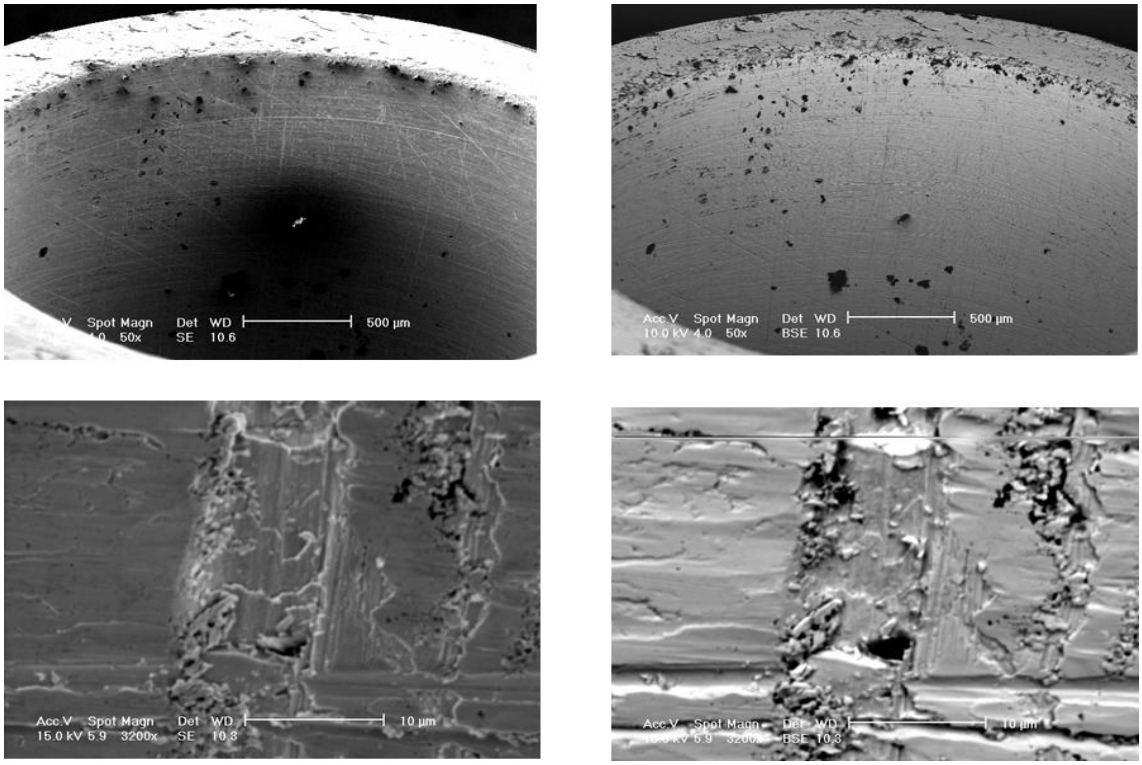

Figure 4.2: Secondary electron (left) and backscattering (right) images of the coated Ir-Re surface. Scales are indicated on the figure.

$$\eta = \frac{\epsilon_{surface}\omega K}{1 - \epsilon_{surface} K} \tag{4.1}$$

In this equation, $\epsilon_{surface}$ is the surface ionisation efficiency according to the Saha-Langmuir equation, ω is the probability for the surface ionised atoms to leave the cavity as ions, and K is the mean number of wall collisions. However, for a given cavity, the values of ω and K are unknown. Estimates exist: at GSI, the orifice diameter of the thermal ion source measures 0.8 mm and K reaches several hundreds, while for the ISOLDE surface ion source, with a tube diameter of 3 mm, it is about 40. The parameter ω has been deduced in an indirect way in a few cases only and typically fluctu-

ates between 0.1 and 0.5 [41]. In order to calculate the ionisation efficiency of the cavity to be used at ALTO and specify the optimised cavity geometry, we have used a Monte-Carlo method.

4.3 Monte-Carlo simulation of the ioniser cavity

4.3.1 Simulation algorithm

We know that for the ISOL technique, the intensities of the radioactive beams depend on many parameters, among which the efficiency of the ion source plays a key role. It is defined as follows:

$$\epsilon_{\left({}^{A}_{Z}X \rightarrow {}^{A}_{Z}X^{+}\right)} = \frac{N\left({}^{A}_{Z}X^{+}\right)_{exit}}{N\left({}^{A}_{Z}X\right)_{input}} \tag{4.2}$$

Here, $N\left({}^{A}_{Z}X\right)_{input}$ is the number of isotopes of interest coming into the ion source and $N\left({}^{A}_{Z}X^{+}\right)_{exit}$ is the number of isotopes of interest that are ionised and released from the ion source. The number $\epsilon_{\left({}^{A}_{Z}X \rightarrow {}^{A}_{Z}X^{+}\right)}$ can be calculated by the Monte-Carlo method.

In the surface ion source, the fate of the atoms of interest flying through the cavity can be described as follows. First of all, the neutral atoms effuse and at some point they may hit the wall of the cavity. There is a probability for the collision to lead to the ionisation of the atoms. The ionised atoms are then transported towards the exit of the tube by an applied electric field that may penetrate the tube, but thermal motion may also make them hit the wall once more, with a finite probability that they recombine and neutralise. The process is repeated until the atoms of interest escape from the cavity. The position and velocity (direction and speed) of the atoms when they fly through the cavity as well as after each collision can be sampled from the calculated distributions.

4.3.2 Determination of the initial position (x, y, z) and velocity (v_0, θ, ϕ) of the neutral atoms

In order to track particles in the ionisation tube, we define an initial co-ordinate system as follows (see figure 4.3):

- The origin of the co-ordinate system is the centre of the input circle
- The XOY plane coincides with the input surface of the ion source
- The Z axis coincides with the tube axis.

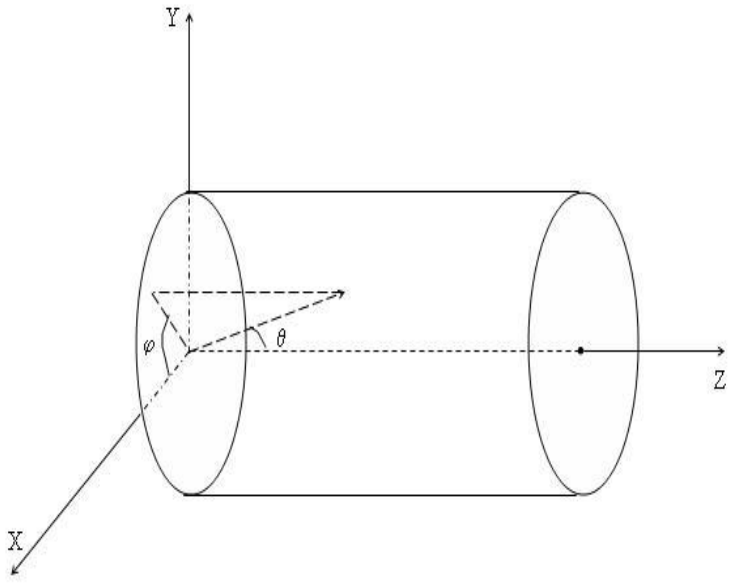

Figure 4.3: The initial co-ordinate system.

The atoms of interest are released from the target and transported to the ion-source cavity through a transfer line. Therefore their incident positions (the initial positions of the neutral atoms) within the input surface are random. For a cavity radius $R = 1.5$ mm, we obtain an initial beam spot as in figure 4.4.

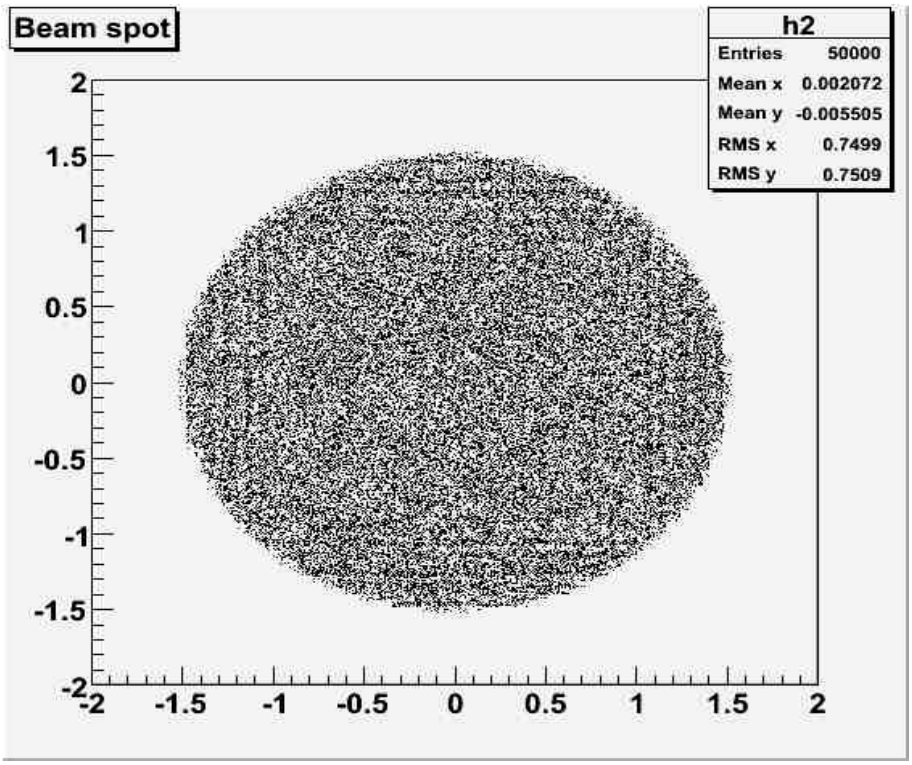

Figure 4.4: Beam spot of the incident particles.

The initial direction of the velocity vector can be specified by polar and azimuthal angles (θ, ϕ). Here, ϕ is a random number that obeys a uniform distribution in the range $(0,\ 2\pi)$.

The flux through the tube, which is the number of particles that passes through the tube per unit of time, for a solid angle $d\Omega$ and defined by an opening angle θ of a cone in the forward direction parallel to the axis of the tube, is given by

$$N(\theta)d\Omega = \frac{nv_{mean}A_s}{4\pi}\cos\theta d\Omega \tag{4.3}$$

Here, n is the number of particles per unit of volume, $v_{mean} = (8kT/\pi M)^{1/2}$ the mean particle velocity for an ideal gas, k the Boltzmann constant, T the absolute temperature in Kelvin, M the mass of the atom and A_s the cross

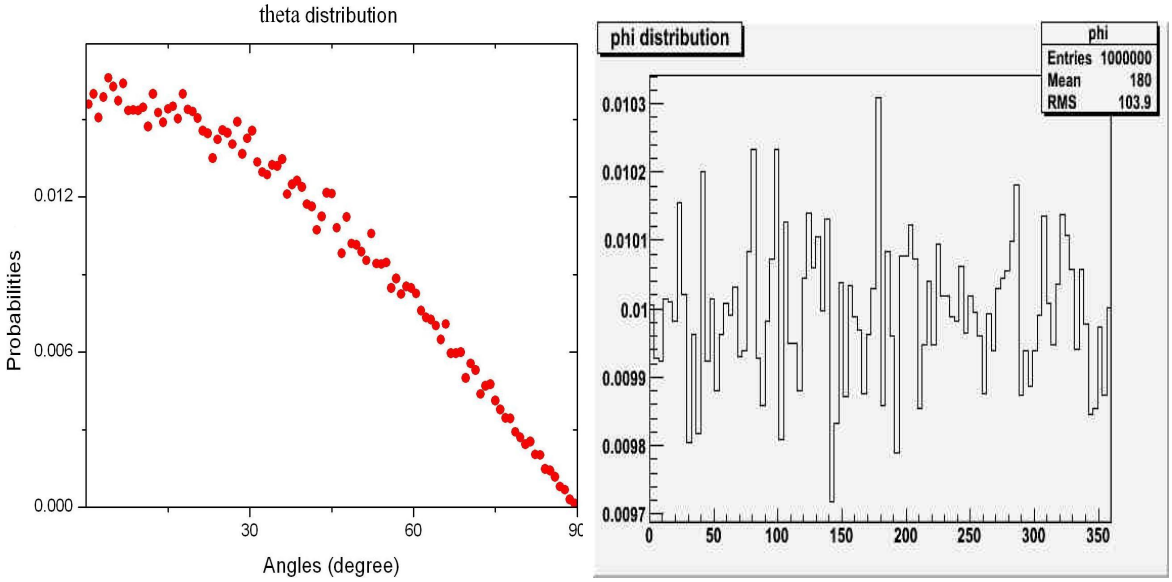

Figure 4.5: Initial angles (θ and ϕ).

section of the tube. The angle θ is a random quantity in the range (0,π/2). The distribution of initial angles (θ, ϕ) is shown in Fig. 4.5.

The initial conditions of the atoms of interest will be fully determined if we also know their speed. The velocity distribution of the thermal motion of the atoms is given by the Maxwell-Boltzmann distribution, that is:

$$D_{MB}\left(v, M, T\right) = 4\pi \left(\frac{M}{2\pi kT}\right)^{3/2} v^2 e^{-\frac{Mv^2}{2kT}} \tag{4.4}$$

Here, v and M are the speed and the atomic mass respectively, T is the temperature of the volume in which the atom is placed. The initial speed of the atom is sampled from this distribution by an exclusive method. First, we determine the value of v_{max} at which D_{MB} reaches its maximum. For a Maxwell-Boltzmann distribution $v_{max} = \sqrt{2kT/M}$. Next we calculate the velocity, obeying a uniform distribution in the range (v_{min}, v_{max}):

$$v = v_{min} + \left(v_{max} - v_{min}\right) q_1 \tag{4.5}$$

Here, q_1 is a uniform random number. In the second step, we select a uniform random number q_2. If

$$q_2 < D_{MB}(v) / D_{MB}(v_{max})$$

then v is accepted. Assuming a temperature $T = 2673$ K, the speed distribution of ^{84}Ga sampled by the above algorithm is shown in figure 4.6.

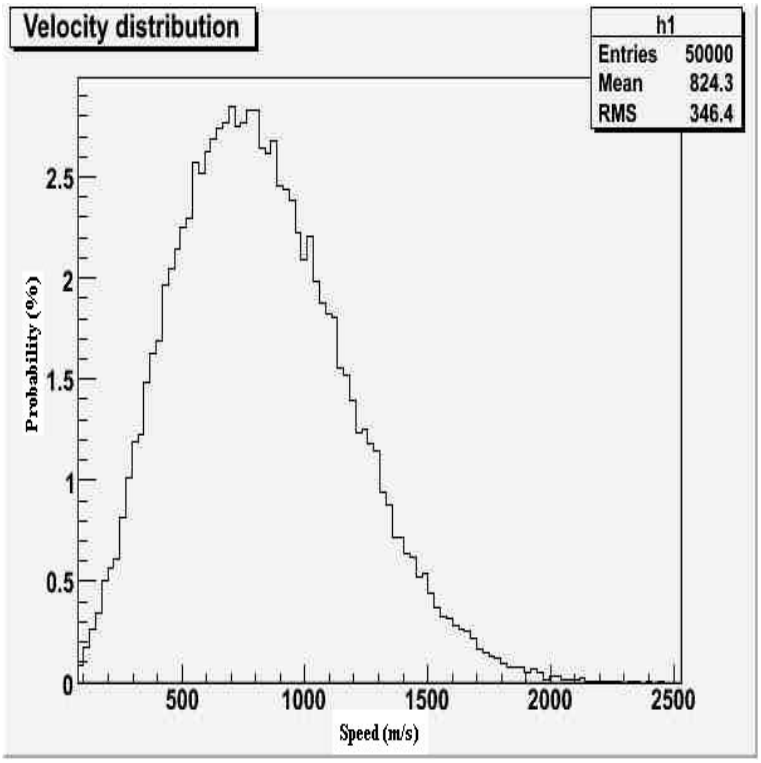

Figure 4.6: Speed distribution of ^{84}Ga at heating temperature $T = 2673$ K.

4.3.3 Effusion and collision model

The incoming atoms with their specific initial velocity and position can be tracked with the assumption that the environment in the cavity is an absolute vacuum. Hence, the atoms will effuse freely in the ionisation tube, hit the

wall and undergo a probability of ionisation. The velocity of the atoms (speed and direction) after each collision can be described by the statistical distributions from a Monte-Carlo approach.

Snell model

The Snell model of elastic reflection is known as mirror-like collision. In this model, the kinetic energy of the atom is conserved and the outgoing angle is the same as the incoming one (see figure 4.7).

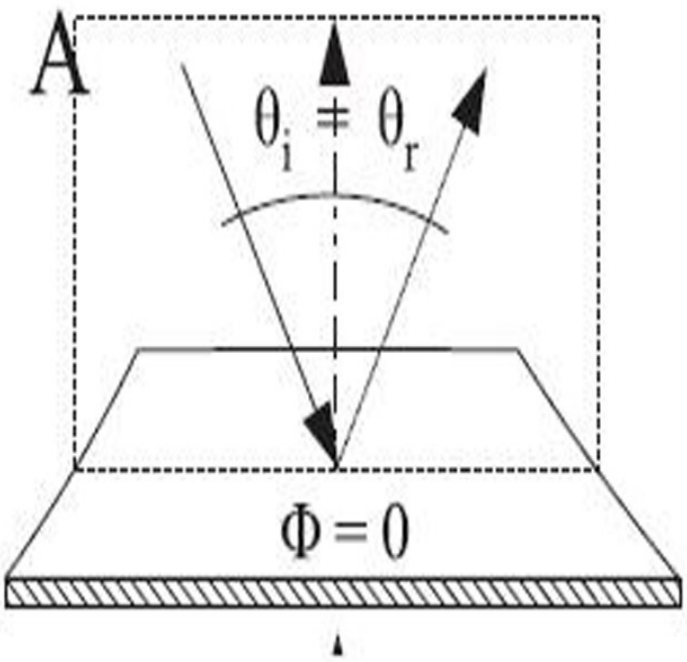

Figure 4.7: Elastic reflection of an atom in the Snell model.

The Snell model can be applied when the atom of interest does not chemically or otherwise interact with the cavity surface. This type of collision is favored for light atoms and very hot and polished surfaces [48].

Lambertian model

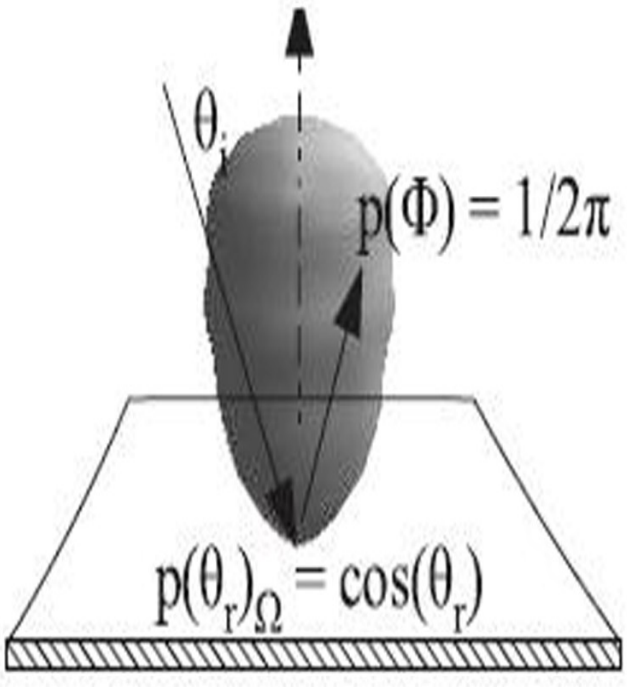

Figure 4.8: Specular cosine law of the collision in the Lambertian model.

The elastic reflection model of Snell is an ideal model and can be applied for smooth surfaces. However, in practice, there is always some roughness in the surface of the cavity. At the same time there may be some absorption of energy in the tube walls so that the atoms lose the memory of the incoming information. In this case, the collision of the atom with the wall can be described by diffuse reflection, named the Lambertian model also known as the cosine law [48]. The atoms are then emitted from the cavity walls (see figure 4.8)under a polar angle θ with a probability as follows:

$$p(\theta) = \cos\theta \tag{4.6}$$

Here, θ is in the range $(0,\ \pi/2)$. The azimuthal angle ϕ is a random quantity uniformly distributed from 0 to 2π. In our calculation, we sample θ after every collision from distribution 4.6 until it fulfils the condition, for a random number q in the range (0, 1),

$$q \leq \cos\theta \tag{4.7}$$

the result of which is presented in figure 4.9.

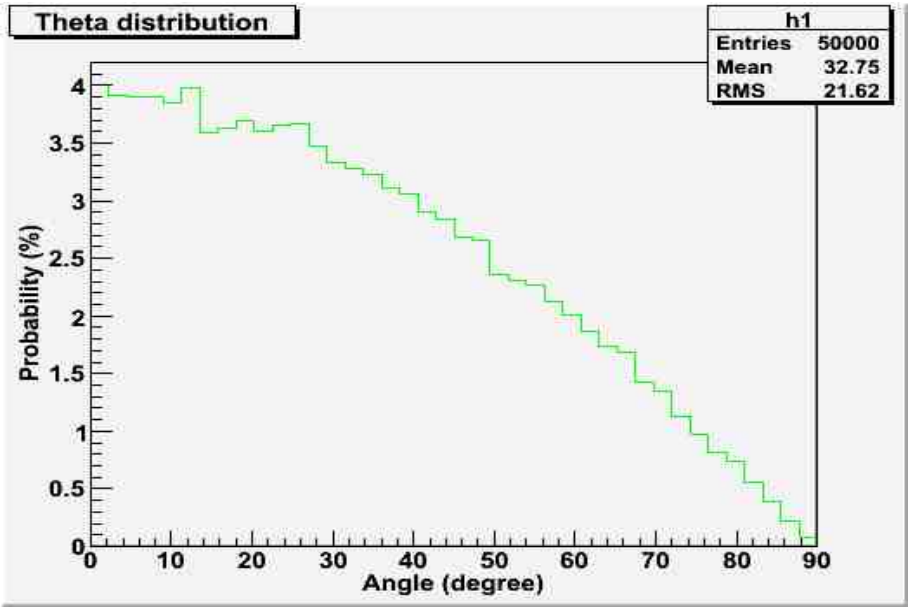

Figure 4.9: Distribution of the angle θ sampled by the Lambertian model.

Regarding the energy, we assume thermalisation of the atoms so the speed of the outgoing atom is sampled from the Maxwell-Boltzmann distribution.

4.3.4 Particle tracking in the cavity

In the ionisation cavity, we track the particles by defining a directional vector (u, v, w):

$$\begin{aligned} u &= \sin\theta\cos\phi \\ v &= \sin\theta\sin\phi \\ w &= \cos\theta \end{aligned} \tag{4.8}$$

The angles θ and ϕ are defined with respect to the original co-ordinate system. The particle co-ordinates (x, y, z) are given by:

$$\begin{aligned} x &= x_0 + v_0 u dt \\ y &= y_0 + v_0 v dt \\ z &= z_0 + v_0 w dt \end{aligned} \tag{4.9}$$

The above equation is valid for neutral atoms, which move in the cavity with constant speed. For ionised ions we need to take into account the acceleration a that is induced by the heating voltage that is applied to the tube. This voltage will induce an electric force F_z along the z axis. Therefore, we have:

$$\begin{aligned} a_x &= 0 \\ a_y &= 0 \\ a_z &= \frac{F_z}{M} = \frac{Vq}{LM} \end{aligned} \tag{4.10}$$

Here, V is the heating voltage, L the ioniser length, q and M are the particle charge and mass, respectively. The (x, y, z) co-ordinates can be calculated by:

$$\begin{aligned} x &= x_0 + v_0 u dt \\ y &= y_0 + v_0 v dt \\ z &= z_0 + (v_0 w + a_z dt) dt \end{aligned} \tag{4.11}$$

After a collision with the ioniser wall the direction of the particle is changed. Thus, we define a local reference system that satisfies the conditions that the origin of the system O' is the collision point on the wall and

the X'O'Y' plane and the O'Z' axis coincide with the tangential plane and the normal to the tangential plane respectively. The local reference system can be obtained from the original one through translation of the origin and Euler rotation (counterclockwise) as follows:

1. Rotate an angle α around the z axis
2. Rotate an angle β around the new y axis
3. Rotate an angle γ around the new z axis

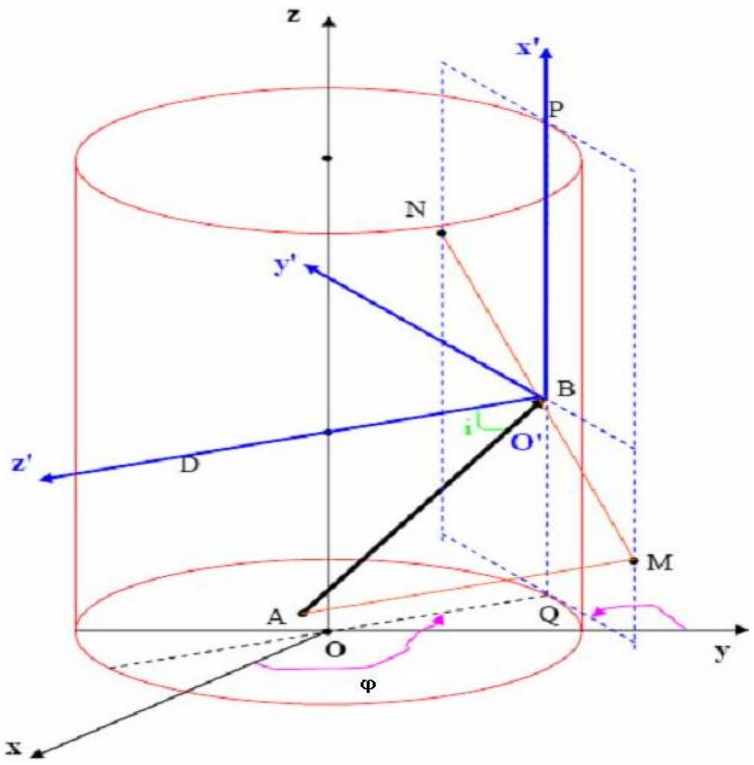

Figure 4.10: The local reference system relative to the original one.

To obtain the local co-ordinate system we use the Euler angles $(\alpha, \beta, \gamma) = (\varphi, -\pi/2, 0)$ (see figure 4.10). Here, φ is the azimuthal angle of the collision point in the original reference system.

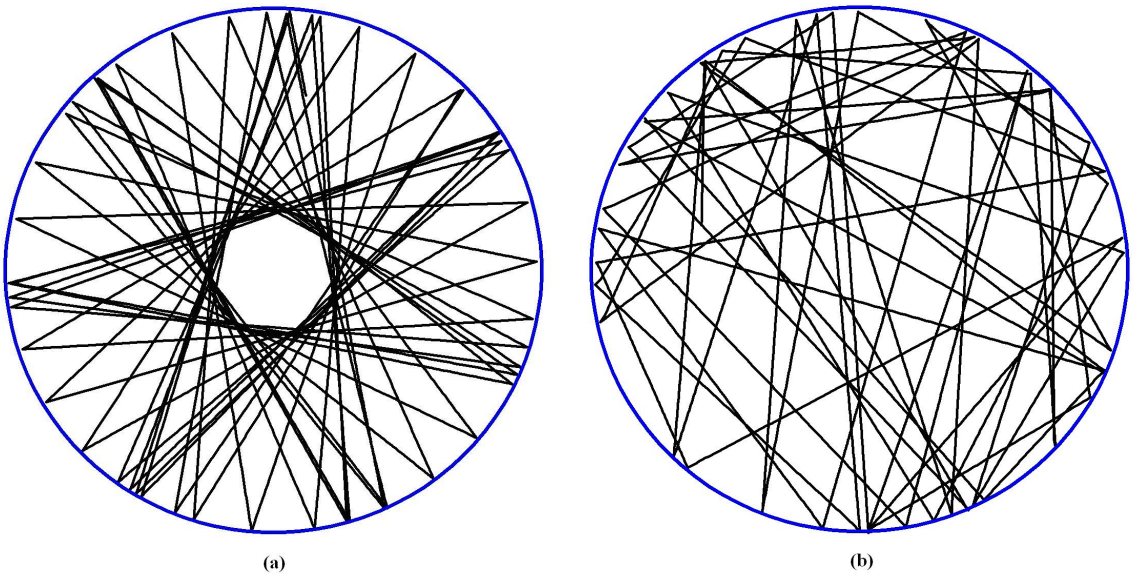

Figure 4.11: Projection of particle trajectories in the XOY plane. (a) Snell model, (b) Lambertian model.

The Euler rotation matrix is given by the expression:

$$\begin{aligned} R &= R_{z,\varphi} R_{y,-\pi/2} R_{z,0} \\ &= \begin{pmatrix} 0 & -sin\varphi & -cos\varphi \\ 0 & cos\varphi & -sin\varphi \\ 1 & 0 & 0 \end{pmatrix} \end{aligned} \tag{4.12}$$

The projections of particle trajectories in the XOY plane corresponding to the Snell and the Lambertian models are shown in figure 4.11.

4.3.5 Surface ionisation and recombination

For calculating the ionisation efficiency of the cavity by the Monte-Carlo method, in a first step, we calculate the single ionisation efficiency of the atom of interest against the cavity material at a given temperature by means of formula 2.2. Every time an atom hits the wall, we sample a uniform random number q and we consider the condition:

$$\text{if } q \leq \epsilon_{surface} \text{then } N_{ion} = N_{ion} + 1 \tag{4.13}$$

Similarly, for ionised atoms, we perform the same algorithm to specify the probability of recombination. Under the hypothesis of a chemical equilibrium for the reaction $X^+ + e^- \rightleftharpoons X$, we assume that this value is equal to the ionisation efficiency from the Saha-Langmuir equation.

4.3.6 Simulation results

Based on the above algorithm, a code in C++ was written to calculate the surface ionisation efficiency of the ioniser tube made from the different materials Ir, Re and W. An operating temperature $T = 2400°$ C was taken. For the standard design of the ISOLDE surface ion source (made from W, length and radius of the tube are 34 mm and 1.5 mm, respectively). Based on the temperature calibration at ISOLDE [48], the heating current was 700 A which corresponds to the heating voltage of 0.11 V. In addition, we have also assumed that the heating current is 700 A for the Re and Ir tubes (with the same dimension as the ISOLDE surface ion-source) which are corresponding to heating voltages of 0.38 V and 0.10 V, respectively.

We have investigated the dependence of the surface ionisation efficiency of gallium on the length and the radius of the ioniser. We have calculated the efficiency for atoms with different ionisation potentials. For ISOLDE's surface ion source, we have performed a calculation of the collision number as well as the flight time of the particles in the ioniser and the obtained results were compared with previously published results. The calculations were done with both the Snell and Lambertian models.

Results with the Snell model

In this section, the results of the calculations with the Snell model are presented. As mentioned before, this model relies on the hypothesis of mirror

reflection, thus particles only move forward in the tube toward the exit hole of the ioniser. In figure 4.12, the distributions for the number of collisions and the flight time of gallium (^{84}Ga)in the ISOLDE standard surface ion source are shown.

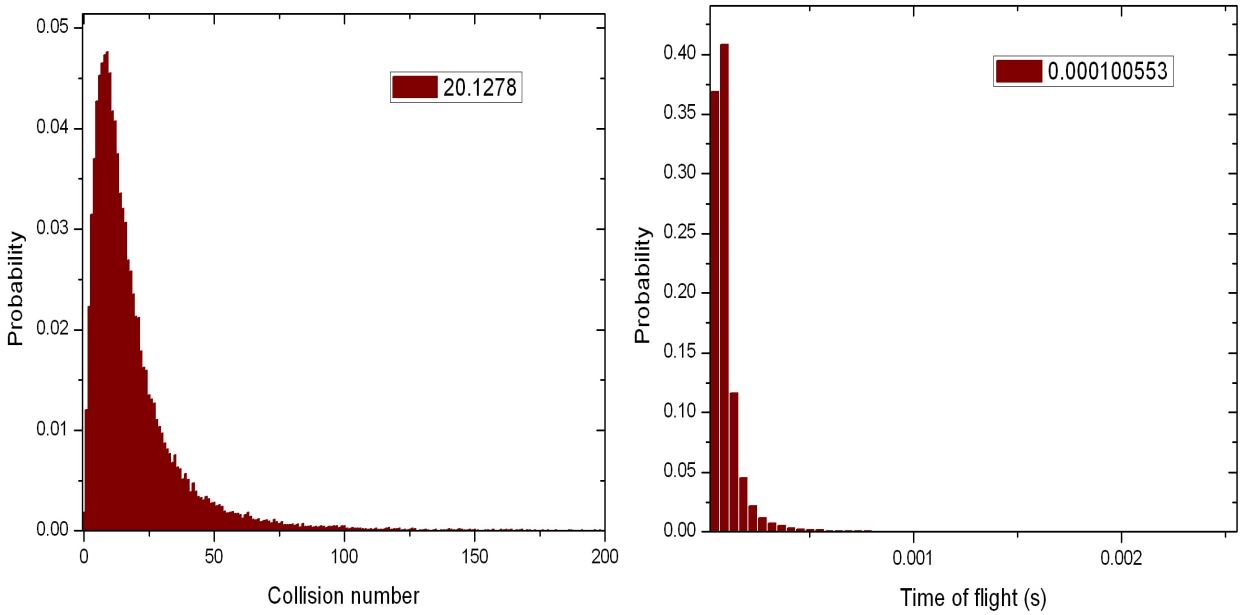

Figure 4.12: Calculated distributions for the number of collisions and the flight time of gallium (^{84}Ga)in a cavity with length of 34 mm and radius of 1.5 mm.

In our calculation, the run includes 50000 events and the obtained average number of collisions N_b is 20.1278. Still with the standard design of the surface ion source, the ionisation efficiencies calculated for different ionisation potentials are shown in figure 4.13. Here, for simplicity, we keep the mass M unchanged (M=84).

The simulation results indicate that the ionisation efficiency drops rapidly when the ionisation potential reaches a specific threshold value W_{th}. These values are approximately 4.4, 5.0 and 5.2 eV for W, Re and Ir, respectively. The work functions for these materials are 4.55, 4.96 and 5.27 eV, so the

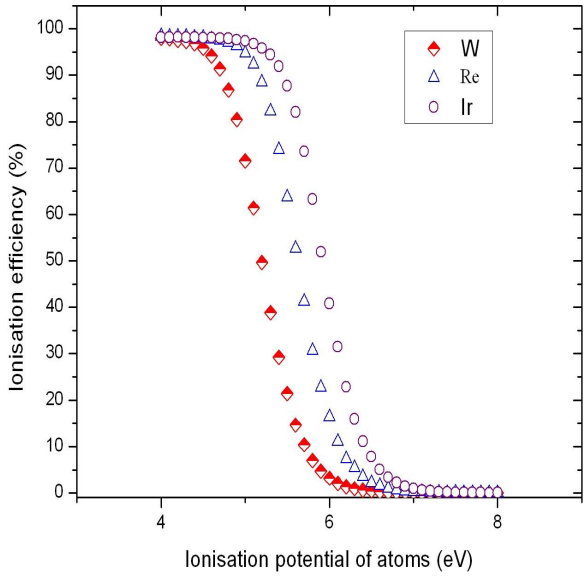

Figure 4.13: Surface ionisation efficiency as function of ionisation potential. The length of the ioniser is 34 mm and its radius is 1.5 mm.

results validate our Monte-Carlo algorithm. In figures 4.14 and 4.15, we show the simulation results for the dependence of the ionisation efficiency of gallium on the length and radius of the tube. From these figures, we can see a clear tendency for the ionisation efficiency to increase with the length of the ionisation tube and decrease with its radius. The result is easily explained by the fact that increasing the length of the tube and decreasing its radius leads to an increase of the mean number of collisions. The simulation results for the Snell model show that the ionisation efficiency of the standard ISOLDE ion source for gallium is 3.36 % while the measured value is 0.7 % [56]. It means that the Snell model, which assumes a perfectly polished surface, is not sufficiently realistic and overestimates the ionisation efficiency. This fact motivates us to pursue the calculations based on the Lambertian model.

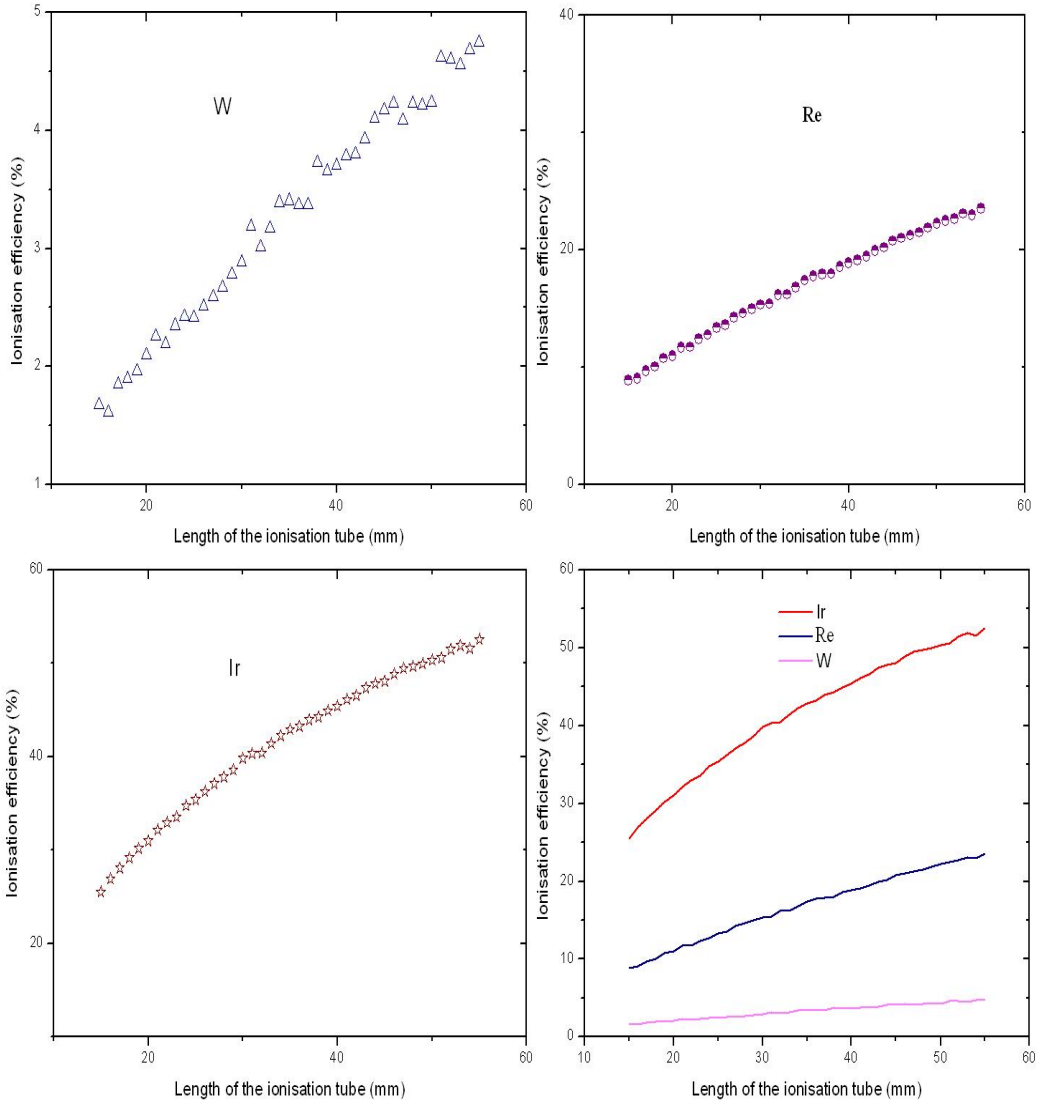

Figure 4.14: Surface ionisation efficiency for gallium as function of ioniser length.

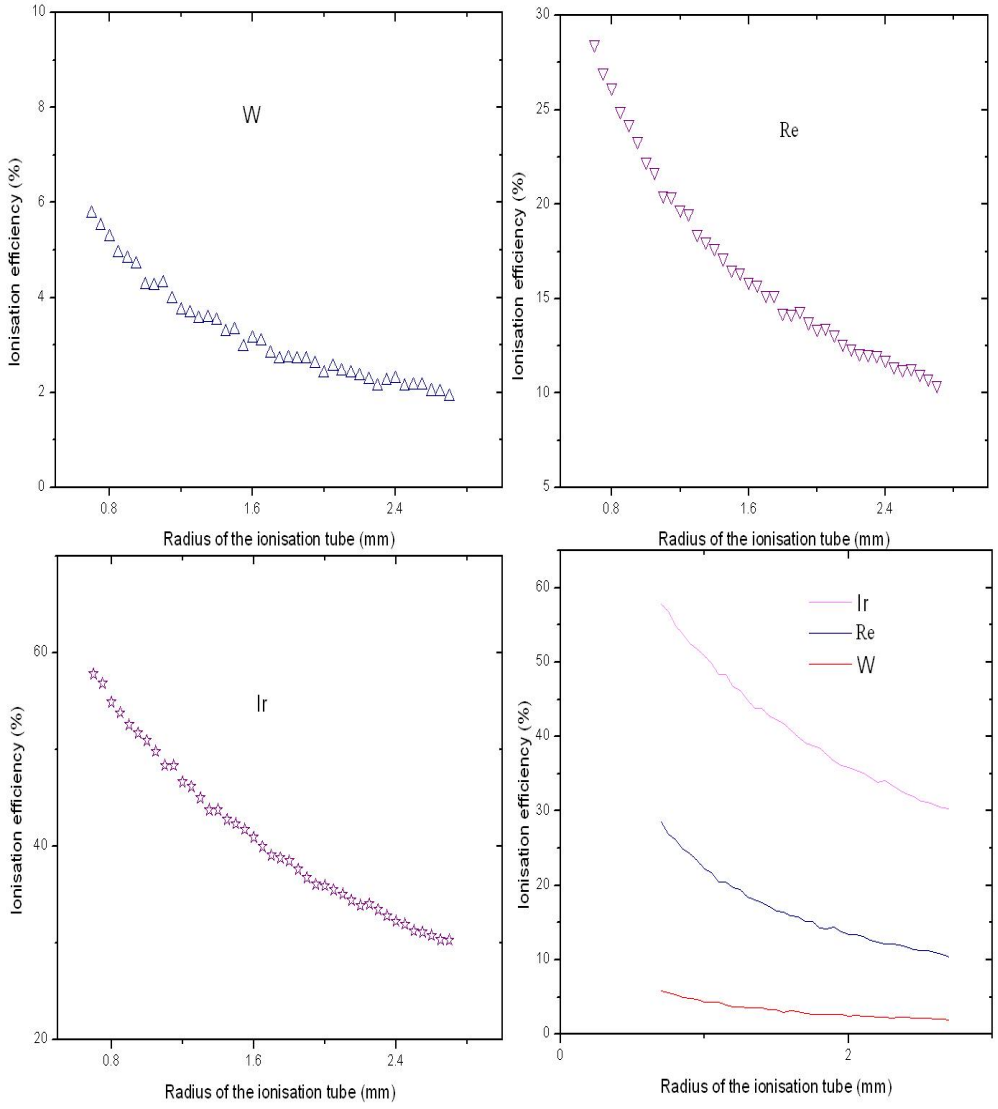

Figure 4.15: Surface ionisation efficiency for gallium as function of ioniser radius.

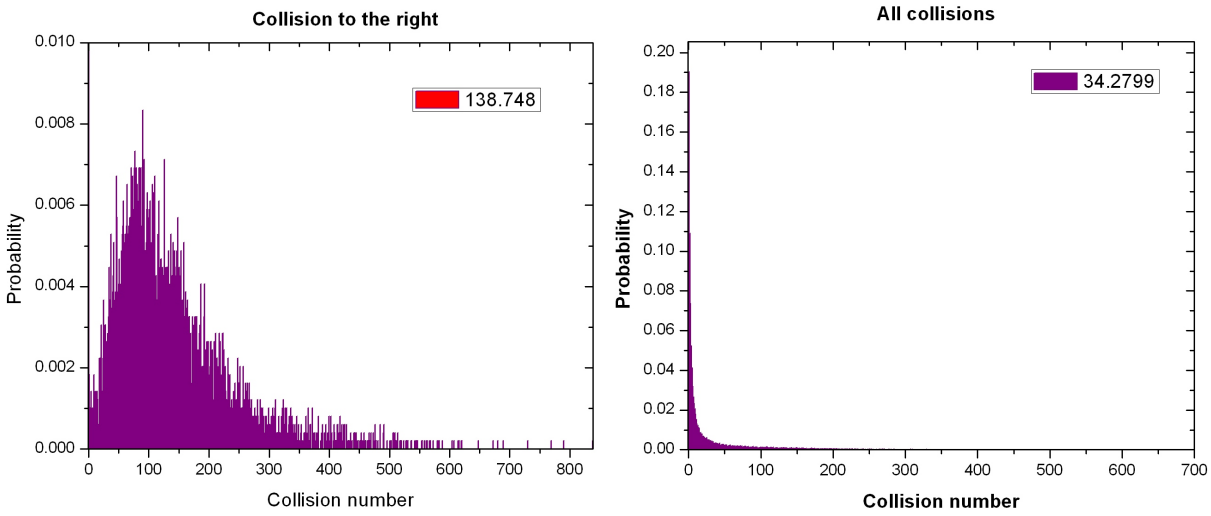

Figure 4.16: Distribution of the number of collisions in a cavity with length of 34 mm and radius of 1.5 mm.

Results with the Lambertian model

For the Lambertian model, we have performed similar calculations as for the Snell model. However, in the Lambertian model, the particle can be backscattered after a wall collision. Therefore, we need to be careful in our calculations whether we take into account all particles or only those that exit from the tube in the forward direction. The resulting distributions for the flight time and the number of collisions for gallium simulated with the standard design of the ISOLDE surface ion source are shown in figures 4.16 and 4.17.

The calculation included 50000 events. The average total number of collisions N_b, average number of collisions of forward particles N_{bf}, average number of collisions of backward particles N_{bb} and ionisation efficiency (taking into account only the forward particles) are shown in table 4.1.

The dependence of the surface ionisation efficiency on the ionisation potential is shown in figure 4.18. As can be seen, the efficiency drops rapidly

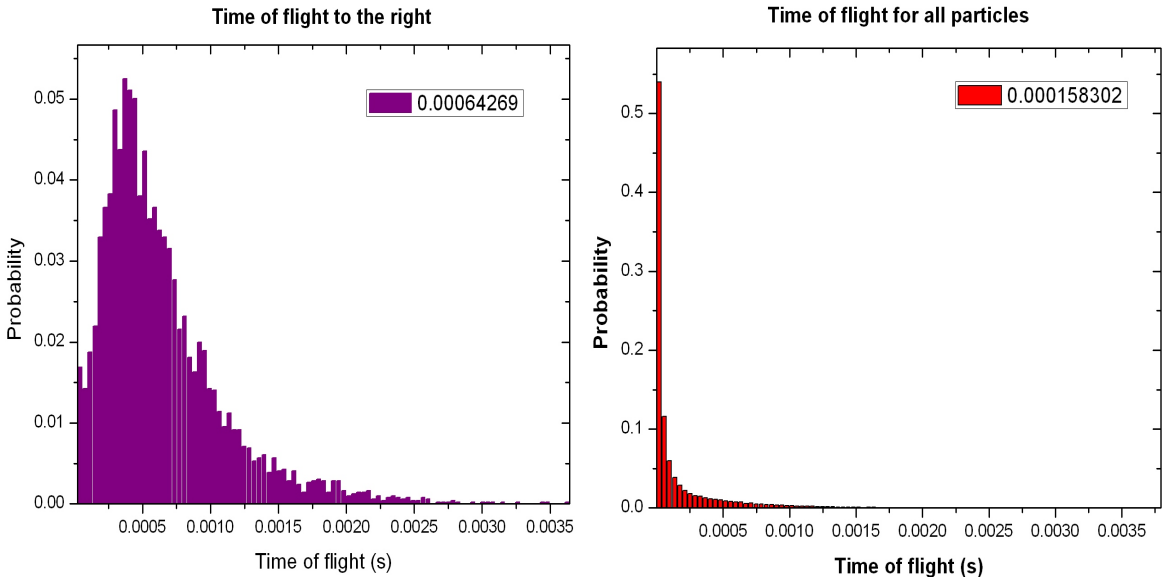

Figure 4.17: Distribution of the flight time in a cavity with length of 34 mm and radius of 1.5 mm.

Table 4.1: Number of wall collisions and ionisation efficiency for Ga in W, Re and Ir ionisation tubes with length 34 mm and radius 1.5 mm.

Material	N_b	N_{bf}	N_{bb}	Ionisation Efficiency [%]
W	34	138	23	0.96
Re	34	125	27	7.73
Ir	36	136	22	9.26

when the ionisation potential reaches a specific value, being 4.2 eV, 4.5 eV and 4.9 eV for W, Re and Ir tubes, respectively. These values are 0.2 to 0.5 eV lower than those obtained with the Snell model and they imply that ionisation is more difficult in the Lambertian model.

In order to investigate the dependence of the surface ionisation efficiency on the length and radius of the ionisation tube, we performed calculations for different length and radius. The results are shown in figures 4.19 and 4.20. Like for Snell model, the ionisation efficiency increases when the length of the tube increases and its radius decreases. However, saturation is reached

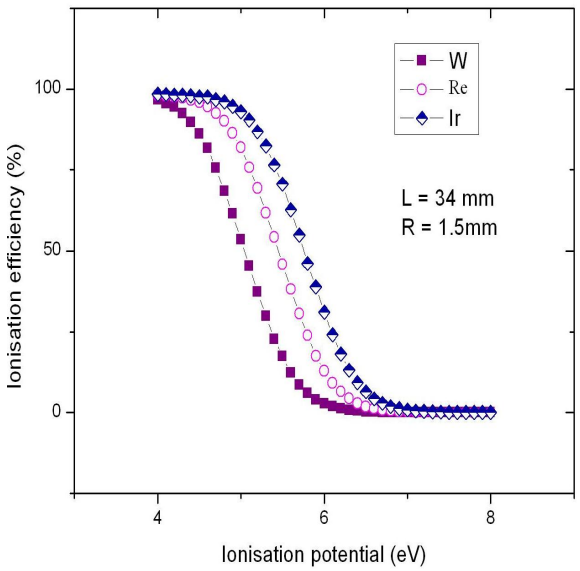

Figure 4.18: Surface ionisation efficiency as function of ionisation potential. The length of the ioniser is 34 mm and its radius is 1.5 mm.

for lengths of 34 mm, 30 mm and 23 mm for W, Re and Ir, respectively.

Discussion of simulation results

From the simulation results of the Snell and Lambertian models, we can see that the Lambertian model reproduces the experimental ionisation efficiency better than the Snell model. However, there still is a discrepancy between the simulated result (0.96 %for Ga in W) and the measured one (0.7 %). This we may explain by the fact that the recombination efficiency put into the calculation (equal to the single ionisation efficiency from the Saha-Langmuir equation) may underestimate the real value and it is necessary to find a better theory to describe the recombination phenomena.

The number of wall collisions calculated by the Lambertian model is 138 for ions that are extracted from the tube to the right, seven times larger than for the Snell model (note that the relevant parameter to compare is indeed

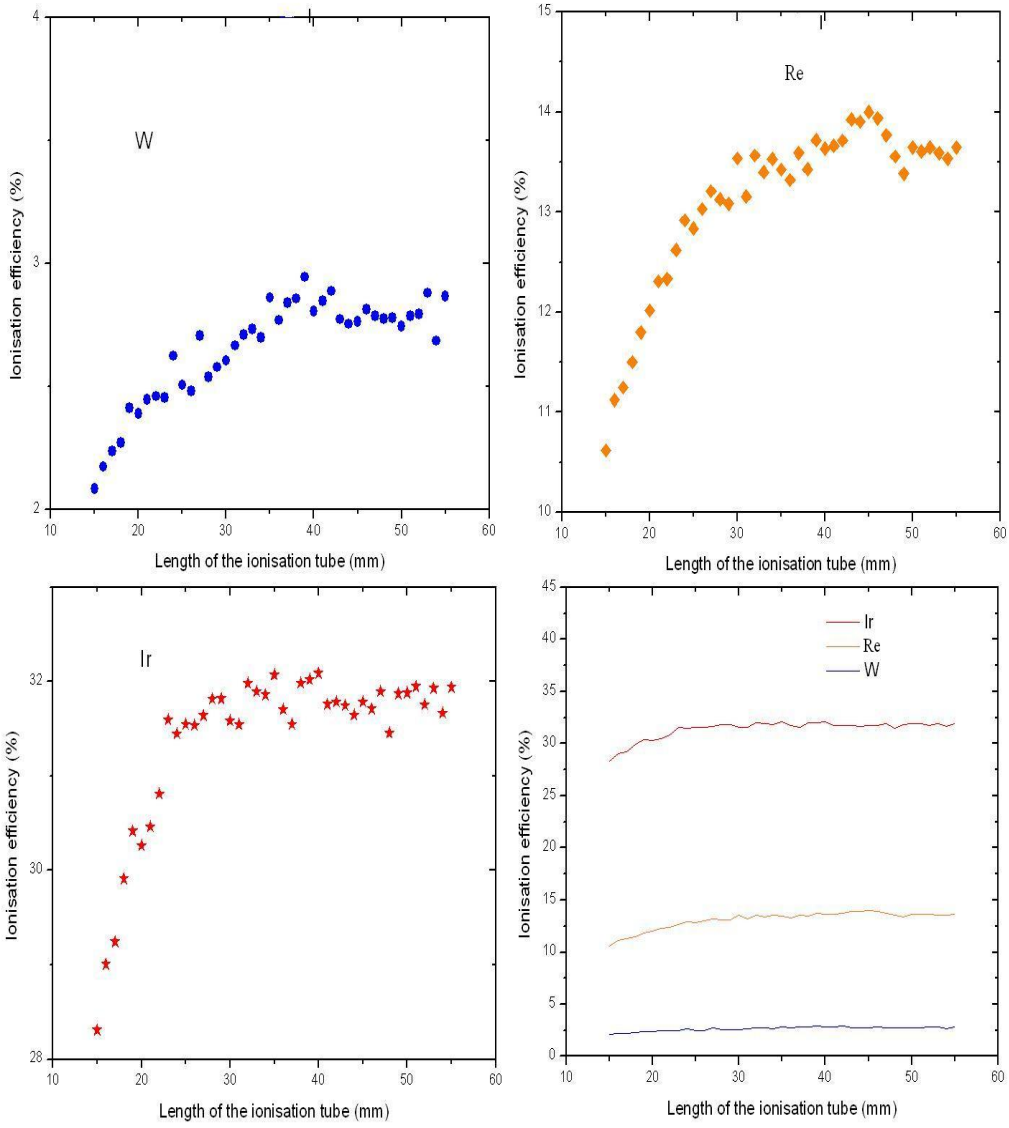

Figure 4.19: Surface ionisation efficiency for gallium as function of ioniser length.

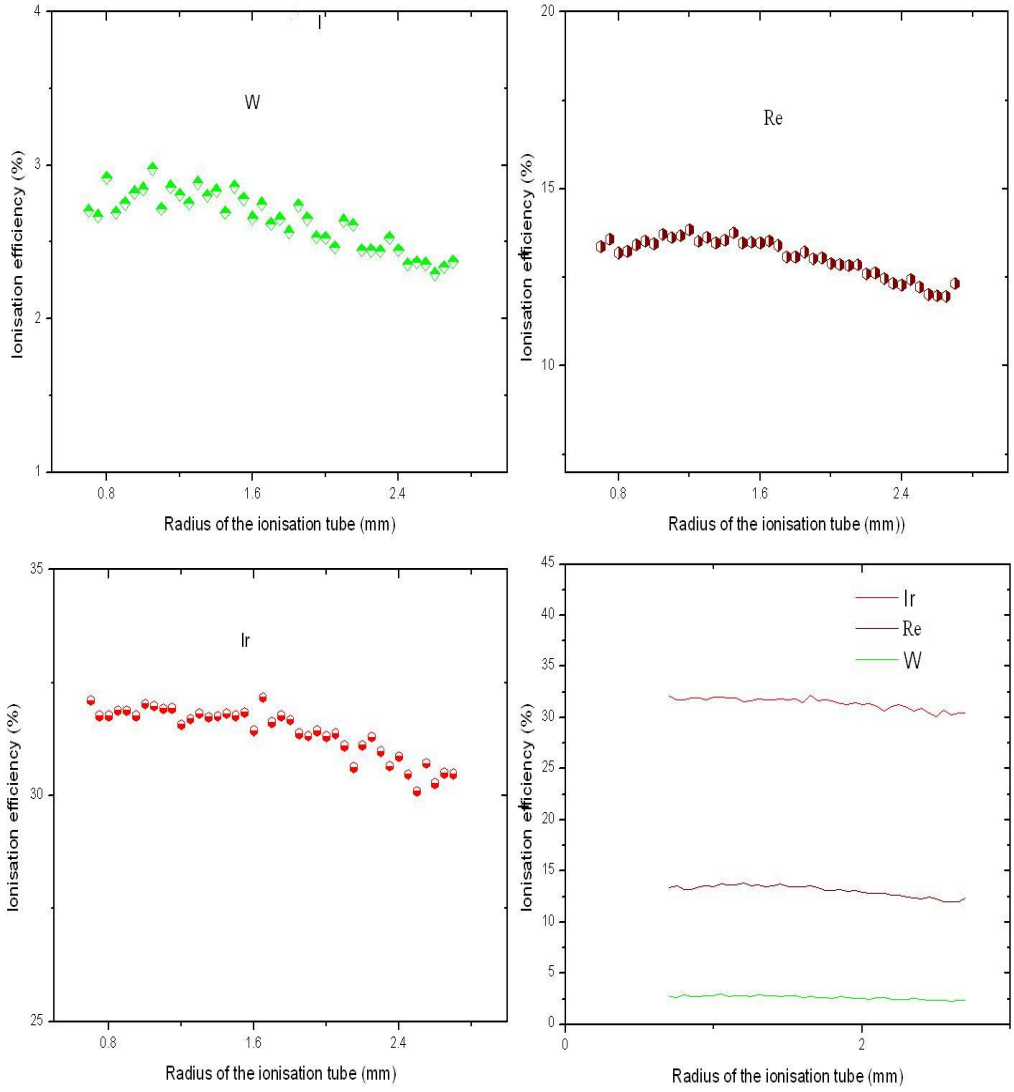

Figure 4.20: Surface ionisation efficiency for gallium as function of ioniser radius.

N_{bf} and not N_b). This is a direct consequence of the inherent Lambert cosine reflection law. The value given in [42] is 40. However, we need to point out that in this reference, the author does not mention whether it is an experimental or a calculated result. On the other hand, a calculation with the fit formula described in [9]:

$$N_b = \left[-0.1019 - \frac{0.103}{a}\right] \times l \times ln(a) + 0.4207 \times l + 0.4253 \times \frac{l}{a}$$
$$+0.4148 \times a + \frac{0.8}{a} - 0.195 + \left[11.85 + \frac{12}{a}\right] \times l^{2.31} \times 2.40 \times 10^{-5} \quad (4.14)$$

in which l is the length of the ioniser and a is the radius of ioniser (this formula is valid over a range of the ioniser dimension $5cm \leq l \leq 50cm$, $0cm \leq a \leq 2cm$), gives us a value of N_{bf} equal to 21. This fact indicates the difficulty to determine the number of collisions accurately.

4.4 First test of a surface ion source efficiency measurement at ALTO

A first test experiment was performed in December 2007, the purpose of which was to measure the surface ionisation efficiency of an iridium-coated rhenium ioniser for gallium as well as investigate the behaviour of the material under extreme conditions like high temperature and chemical attack by other materials that constitute the ion source.

4.4.1 Description of the surface ion source

Figure 4.21 shows the installation of the surface ion source at Orsay. In the off-line test experiments, the element of interest is placed in an external boron nitrite crucible or an internal graphite container. By heating the tantalum oven to which the crucible is attached or in which the container is placed,

the atoms will effuse, first through a tantalum transfer line and then into the ioniser.

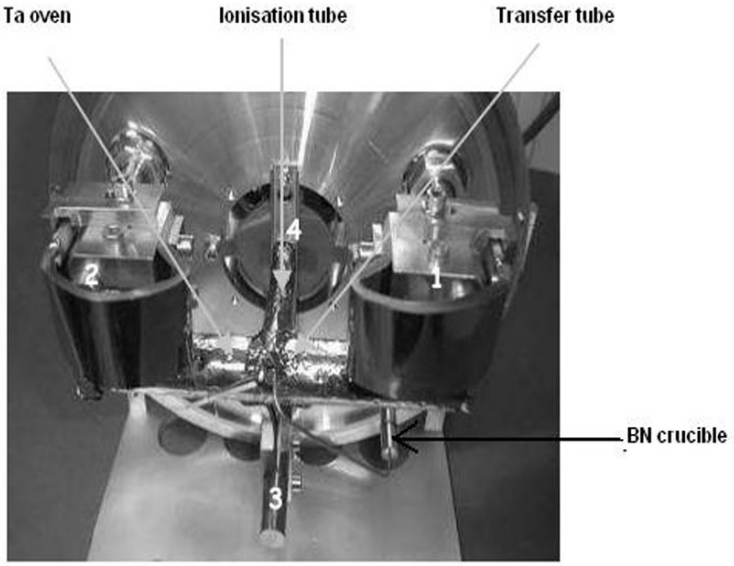

Figure 4.21: Surface ion source installation at Orsay.

The ioniser is a cylindrical tube with the same dimensions as the standard surface ion source at ISOLDE, of which the length is 34 mm, the internal diameter 3.1 mm and the external diameter 5 mm. The ioniser was made from iridium-coated rhenium.

4.4.2 Principle of the off-line efficiency measurement

In order to measure the efficiency of the surface ion source, we put a given amount of the element of interest (gallium) into the target container or the attached crucible. By heating, the atoms effuse thermally into the ionisation tube and there is a probability for them to be ionised into positively charged 1^+ particles. The extracted current of the mass-separated ion beam is measured by a Faraday cup or a microchannel plate. After complete evaporation

of the sample, the ionisation efficiency is given by the ratio between the integrated current and the number of atoms that were put in the container (or attached crucible):

$$\epsilon_{surface} = \frac{\int I dt}{n N_A q} \tag{4.15}$$

Here, I is the measured current, n is the molar quantity of the isotope of interest, and q is the charge of the ion.

To avoid isobaric contamination in our method, we should use a sample of high purity of the element of interest.

4.4.3 Evaporation properties of gallium

The electromagnetic mass separator only operates properly when its vacuum pressure is below 10^{-5} mbar. It is therefore necessary to investigate the vapor pressure of gallium as function of the temperature so we may calculate an upper limit for the heating temperature we apply. The vapor pressure of gallium as function of the temperature is shown in figure 4.22.

From the figure, we can see that the temperature of the container should be kept below 740 °C.

4.4.4 Temperature calibration of the ion-source components

In order to determine the temperature of the various ion-source components (ionisation tube, tantalum oven and boron nitrite crucible), we performed a temperature calibration as function of the heating current that is applied to the ion source. The temperature measurements are done by tungsten-rhenium thermocouples for high temperatures and iron-constantine thermocouples that have high sensitivity for low temperatures. Figure 4.23 shows the relationship between the measured potential and the temperature for

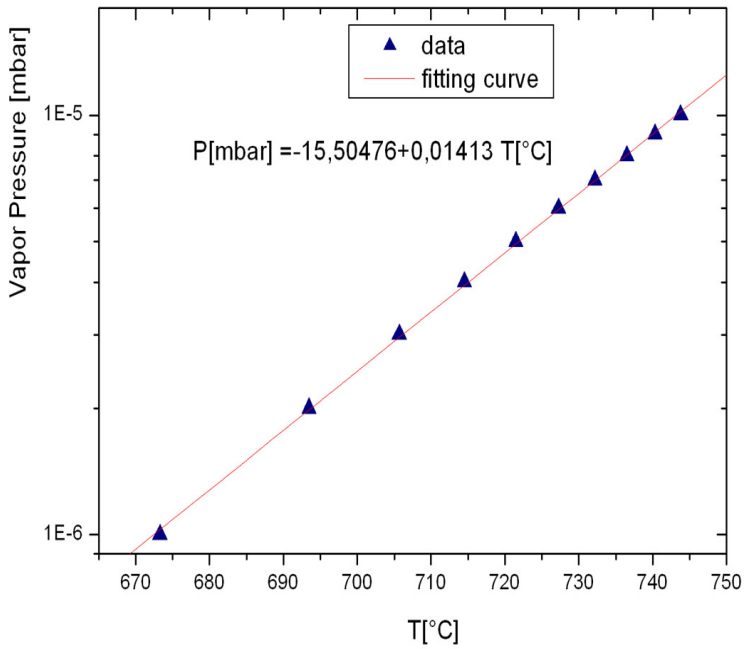

Figure 4.22: Vapor pressure of gallium as function of the temperature, data are taken from [36].

tungsten-rhenium and iron-constantine. For the first thermocouple, the application range is from 1650 °C to 2315 °C and for the second one, from 95 °C to 760 °C.

Tantalum oven

In figure 4.24 we plot the temperature of the tantalum oven and the rhenium-iridium ioniser tube as function of the power and current that is applied on the oven. We can see that at a power of 3900 W (or a current of 650 A), the temperatures of the oven and the ioniser tube reach values of 1700 °C and 820 °C, respectively. We stress that in this measurement no current is applied directly on the ioniser. Since the temperature of the ioniser nevertheless reaches quite a high value, it means that it is strongly affected in an

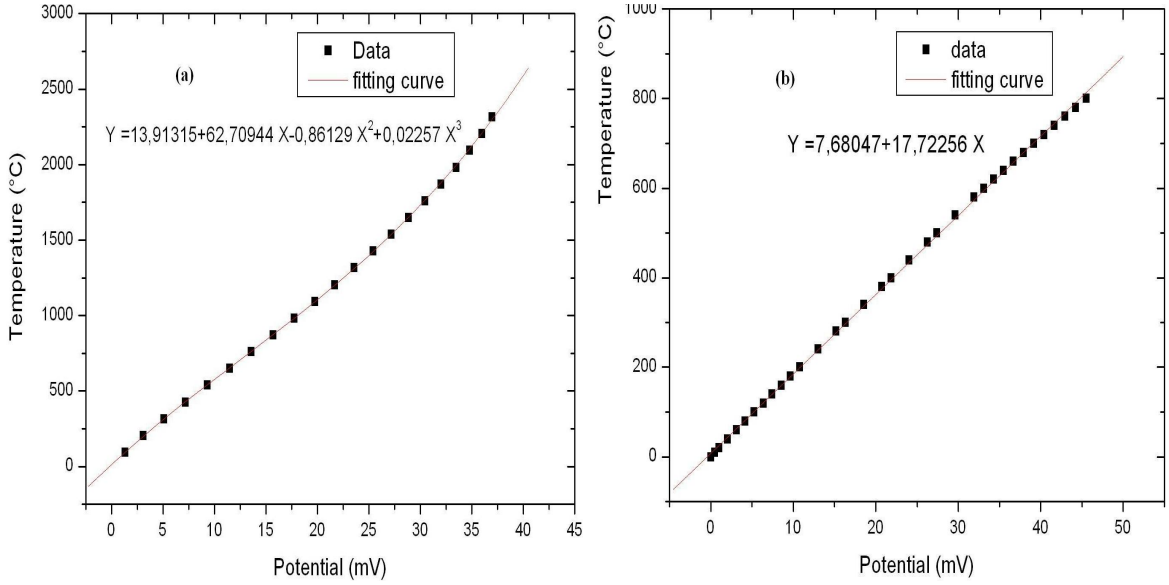

Figure 4.23: Relationship between thermally induced potential and temperature for (a) tungsten-rhenium thermocouple and (b) iron-constantine thermocouple [1].

indirect way by the heating of the tantalum oven. This result tells us that the temperature calibration of the ioniser as function of the current applied on it, should be done at various temperatures of the oven, such that we may evaluate the effect of the heating of the oven on the ioniser (see next section).

Rhenium-iridium ioniser tube

As mentioned above, in order to evaluate the effect of the heating of the oven on the ioniser tube, we have fixed the current of the tantalum oven at 200 A ($T_{oven} = 650\,^{\circ}\mathrm{C}$) and then 500 A ($T_{oven} = 1485\,^{\circ}\mathrm{C}$). For each case we measured the temperature of the ioniser as function of the power and current applied on the ioniser. The experimental results are shown in figure 4.25.

From this figure we can see that at low temperature, the heating of the oven affects strongly the temperature of the ioniser but when the temperature

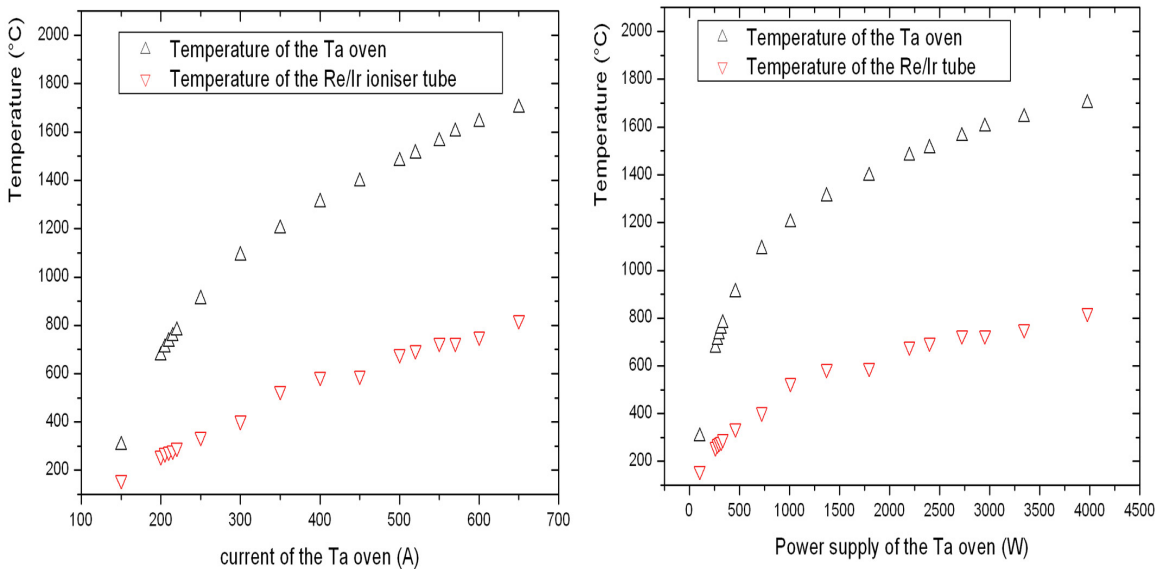

Figure 4.24: Temperature calibration of the tantalum oven and the ioniser tube as function of power and current applied on the oven.

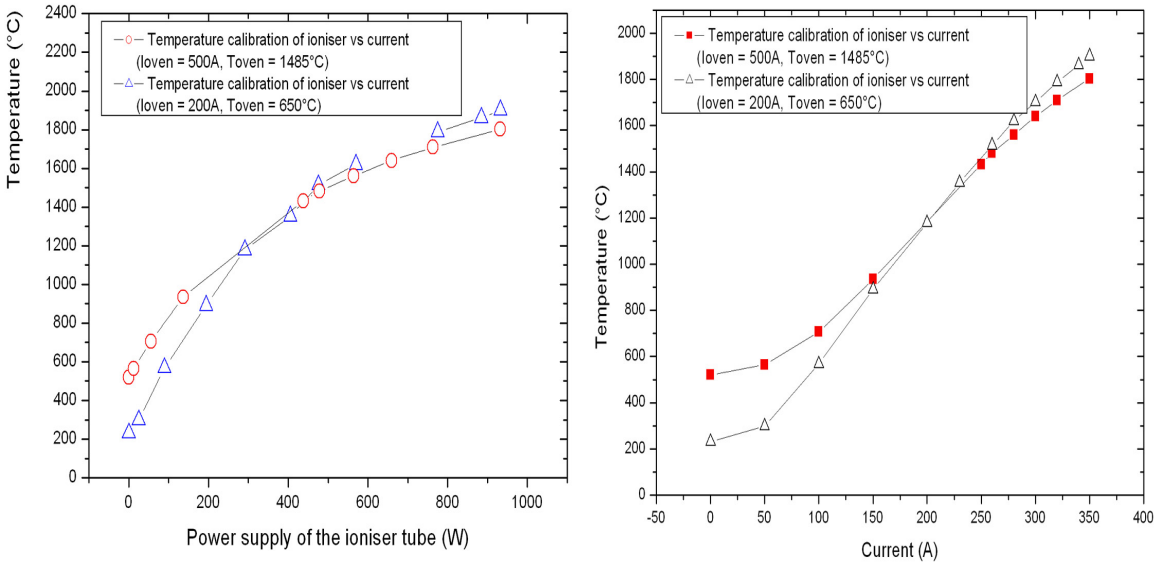

Figure 4.25: Temperature calibration of the rhenium-iridium ioniser tube as function of power and current applied on it.

of the ioniser reaches values above 1000 °C its temperature is quite the same for both oven currents of 200 A and 500 A. This independent heating of the oven and the ioniser at high temperature is confirmed when we look at the evolution of the oven temperature as function of the current applied on the ioniser, drawn in figure 4.26.

The calibration results also show that at the highest power applied to the ioniser of 930 W (current of 350 A), its temperature is 1900 °C.

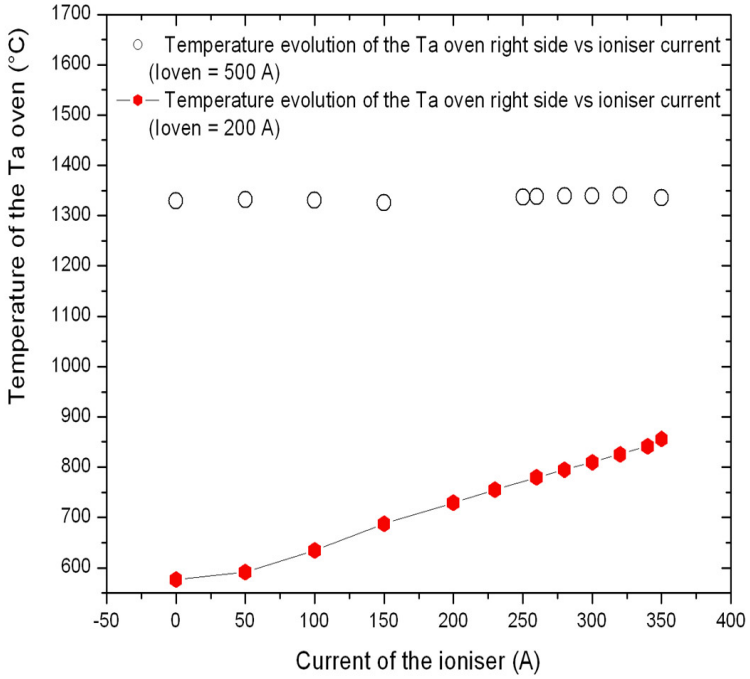

Figure 4.26: Temperature of the tantalum oven versus current of the ioniser.

Boron nitrite crucible

The boron nitrite crucible is heated indirectly in the ion source by thermal interaction with the oven and ioniser tube. As such we fixed a current on the tantalum oven of first 200 A and then 500 A, as was done for the calibration of

the ioniser. The temperature calibration of the crucible was then performed as function of the current applied on the ioniser. It is shown in figure 4.27.

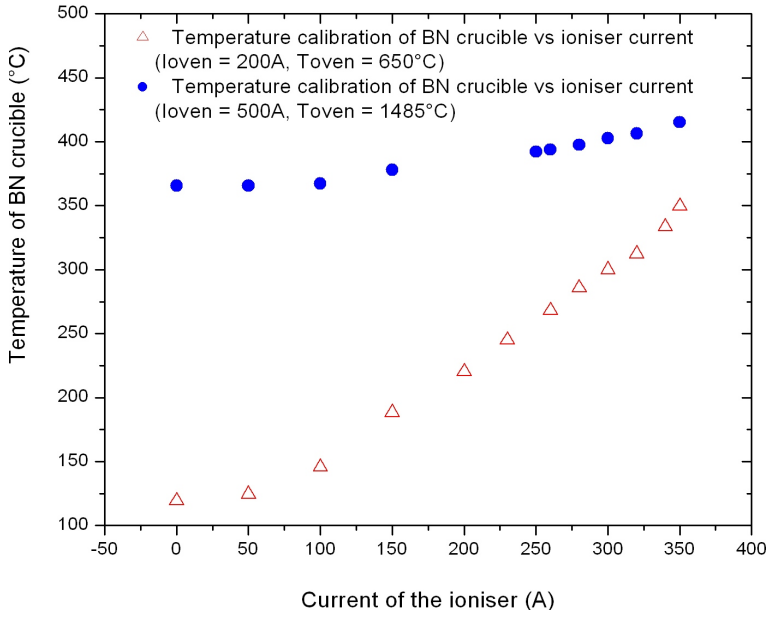

Figure 4.27: Temperature calibration of the boron nitrite crucible versus ioniser current

4.4.5 Results and present status

We put into the boron nitrite crucible 62 mg of high purity (99.99 %) stable gallium, which includes the two isotopes ^{69}Ga and ^{71}Ga with natural abundances of 60.11 % and 33.89 %, respectively. We increased the current of the tube and the oven stepwise up to 200 A ($T_{tube} \approx 1000\,^{\circ}$C and $T_{BN} \approx 230\,^{\circ}$C). At this temperature, gallium is expected to effuse slowly into the ioniser through the transfer tube and proceed to ionisation. The separator was calibrated to select ^{69}Ga or ^{71}Ga. Under these conditions we detected separated ionised gallium with a current of several nA.

Subsequently the current of the ioniser tube was increased to 250 A ($T_{tube} \approx 1500\,^{\circ}$C and $T_{BN} \approx 300\,^{\circ}$C). The separated gallium current that was

detected increased to about 100 nA. The rapid increase can be explained by the fact that for higher heating temperatures, more gallium is evaporated and effuses into the ioniser, while also the ionisation efficiency is bigger for higher temperatures (Saha-Langmuir equation). Moreover, particles that stick to the walls of the ion source will effuse out of it more easily at higher temperatures.

Finally, the current of the ioniser was increased to 300 A ($T_{tube} \approx 1800°$C). At this temperature, the ioniser tube suddenly melted (see figure 4.28).

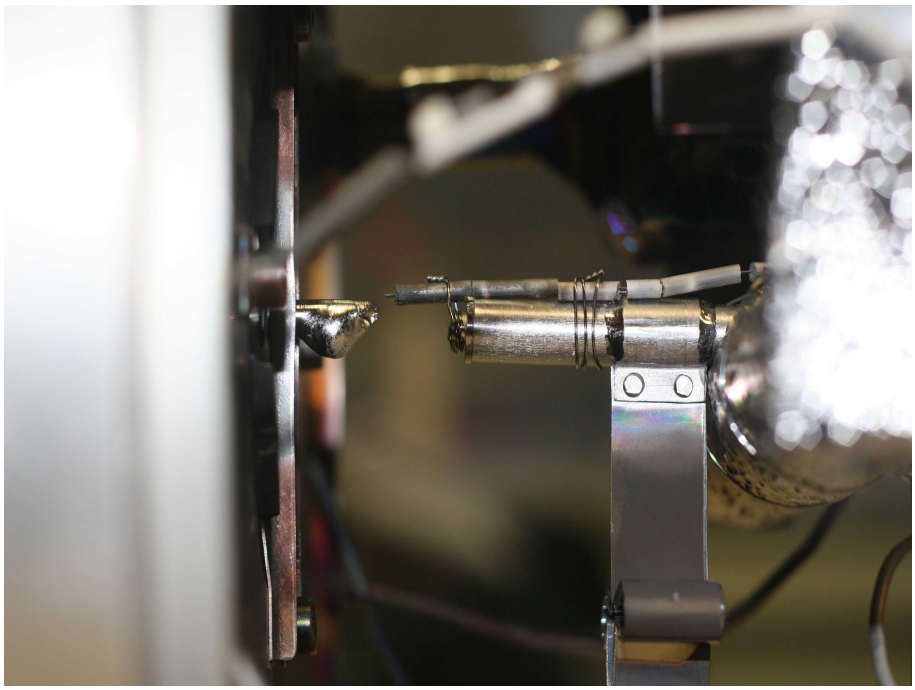

Figure 4.28: The ioniser tube after heating by a 300 A current.

The failure of the tube was not understood, considering that the melting point of iridium is at 2443 °C while for rhenium it is at 3180 °C. Contamination of the tube material, however, could have led to the formation of a compound with lower melting temperature, called a eutectic. A eutectic point of iridium with carbon is reported in the literature at 2296 °C and for

an Ir-Rh alloy with carbon at 1932 °C [39]. Contamination with silicon would furthermore lower the eutectic point, in the case of Ir-C to 2150 °C. Tantalum and rhenium are known to form a eutectic at 2690 °C. An RBS analysis of the molten tube was carried out at the CSNSM laboratory in Orsay but it did not show the presence of any element other than rhenium and iridium (see figure 4.29). It is to be said that the RBS technique, unfortunately, was not sensitive to carbon because of the low backscattering energy for carbon and therefore the diagnosis is not conclusive.

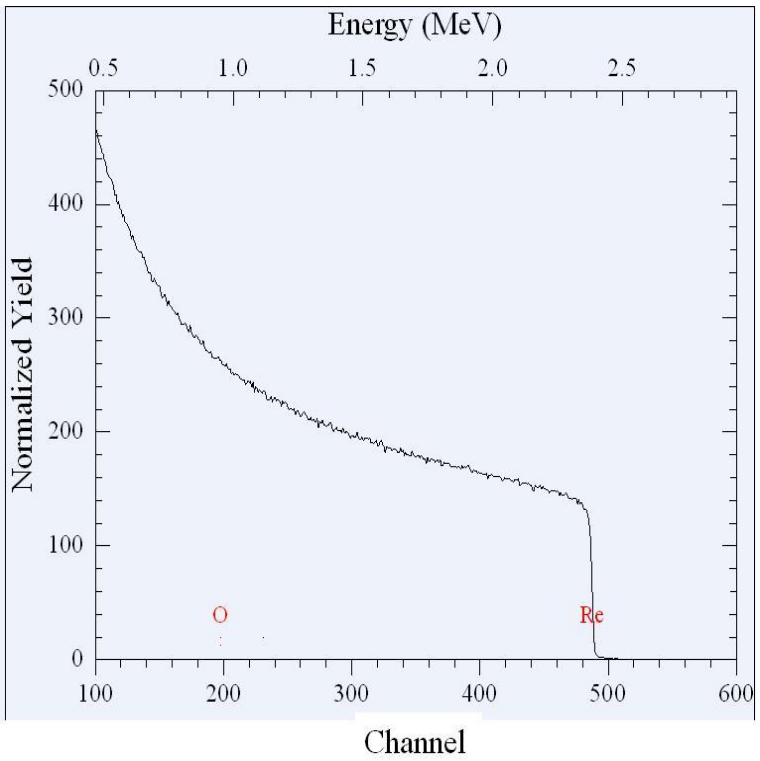

Figure 4.29: RBS spectrum of the molten rhenium-iridium tube.

Another explanation could be that mechanical tensions created a gap between the tube and the tantalum transfer line to which it was attached. The current could then have arced across the gap and this melted the tube.

Chapter 5

Theoretical Study of an Ion Guide for ALTO

In this chapter, we review the development and the characteristic properties of the IGISOL (Ion Guide Isotope Separator On-Line) technique and its coupling to a laser ion source. Besides, we investigate the possibility to implement a gas cell filled with argon noble gas for thermalisation of radioactive ions at the ALTO facility at IPN Orsay and SPIRAL-2 at GANIL through a GEANT-4 simulation. The calculation is dedicated to the design and development of a future generation of ion sources for the ALTO and SPIRAL-2 projects. In order to validate the simulation by means of comparison with published results and furthermore evaluate the rate of ionisation of the noble gas by the primary beam, we also performed the calculation for the case of an impinging proton beam.

5.1 The ion guide among the ISOL technique

5.1.1 Introduction

As mentioned in section 2.1, over 50 years ago, the development of the Isotope Separator On-Line (ISOL) technique opened a major perspective for the

study of short-lived and rare radioactive isotopes [11]. In an ISOL system, the nuclear reaction products are stopped after production, then extracted, accelerated (typically to an energy of a few tens of keV) and mass-separated. Figure 5.1 illustrates a classification of different ISOL concepts according to the way the reaction products are stopped.

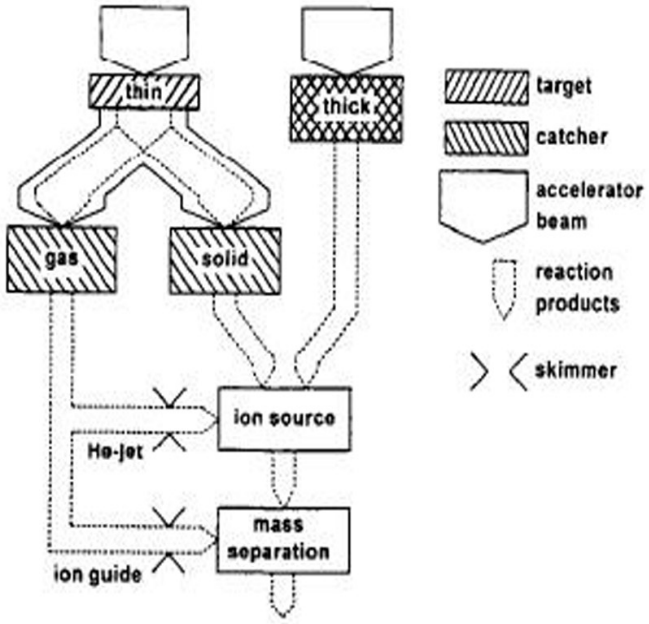

Figure 5.1: A classification of different ISOL concepts according to the way the reaction products are stopped [11].

If the target is much thicker than the recoil range of the reaction products, most of these are stopped in the target. For thin targets, on the other hand, most reaction products recoil out of the target and are stopped in a solid or gaseous catcher. Reaction products that are stopped in solid material (target or catcher) are released through diffusion and transported to an ion source. Often, the target or catcher are an integral part of the ion source. The technique in which one uses a thin target combined with a gas cell (filled

with a noble gas, in particular helium or argon) for stopping and thermalising the recoiling nuclear reaction products as well as transporting them by the gas flow through a differential pumping system directly into the acceleration stage of the mass separator, is called the Ion Guide Isotope Separator On-Line (IGISOL) method. The losses of short-lived exotic ions due to the long delay that is induced by the relatively slow gas flow can be reduced by applying electrical DC or RF fields in the gas cell that guide the ions towards the exit hole. This process can be made fast enough (of the order of 10 ms) for a considerable fraction of the reaction products to survive as 1^+ ions.

The IGISOL technique has been used to study short-lived ($T_{1/2} > 0.1$ ms) exotic isotopes for more than 20 years now. The first experiments on the transport of radioactive ions in a gas flow were carried out with an α recoil source [7] and soon after that, on-line with a 20 MeV proton beam at the University of Jyväskylä in Finland [4]. These early experiments showed that in order to achieve a reasonable transport efficiency a fast flow rate was necessary and delay times of the ions in the gas cell less than 10 ms could be reached. It was demonstrated that with this technique ion beams can be produced of radionuclides of virtually all elements, including the most refractory ones [5, 6].

A variant of the method is based on the selective laser ionisation of the short-lived radioactive species that are thermalised in the buffer gas as neutral atoms. This will be discussed in section 5.2.

5.1.2 Principle of the ion-guide method

In figure 5.2 we illustrate the IGISOL technique in its most basic form. The idea of the ion guide is that the reaction products that are produced by the interaction of the accelerator beam and the target recoil out of the target and slow down and thermalise in the gas cell to a 1^+ charge state. The buffer gas is typically helium or argon. The ions are transported by the gas flow

out of the cell and injected through a differentially pumped electrode system into the high vacuum section of the isotope separator, where they are further accelerated and mass-separated.

The electrode system can consist of a single conical skimmer with an electrical field of the order of 500 V/cm or a drift electrode sequence at a low voltage of some 10 V/cm, called a squeezer. Due to space-charge effects, the skimmer electrode is suitable for the extraction of high-intensity beams, whereas the low-voltage devices are better suited for weak ion beams [8]. Because of the energetic collisions with the buffer gas atoms near the exit aperture of the gas cell at high electrical fields, the ion beams extracted by the skimmer are associated with an energy spread that can be as large as 10 to 100 eV. For this reason, other approaches employing linear radio-frequency cooler devices have been proposed and developed at the University of Louvain in Belgium [31].

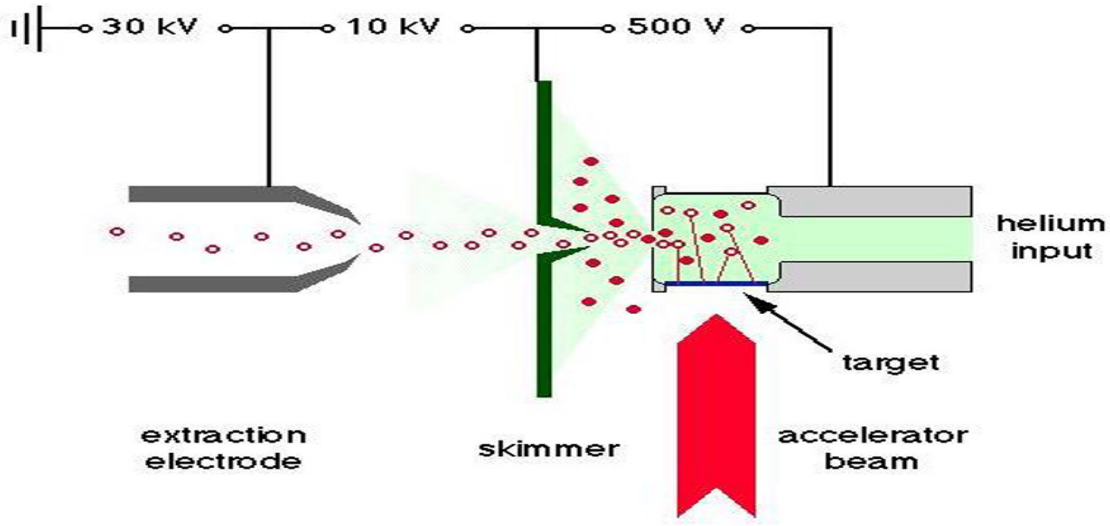

Figure 5.2: Principle of the ion guide. Primary reaction products are thermalised as ions and are transported in the gas flow and by electrical fields into the accelerating stage of the mass separator [8].

The technique is limited to thin targets with a thickness equal to the range of the recoil ion in the target, which is of the order of 1 mg/cm^2 for fusion-evaporation residues and 15 mg/cm^2 for fission fragments [8].

The slowing down of the ion in the gas resets its charge state by means of charge-exchange collisions that are determined by the velocity. If we assume a 100 % pure stopping gas, the radioactive ions can reach a 2^+ charge in collisions with helium atoms because for most elements the second ionisation potential is below the first ionisation potential of helium. In argon, a 1^+ charge state can be reached for many elements. However, impurities such as H_2, O_2 and H_2O on a sub-ppm level can easily reduce the charge state of an ion to 1^+. Furthermore, the ionisation of the stopping gas by swift recoil ions and primary-beam particles may lead to important three-body recombination processes involving electrons, ions and neutral gas atoms. It may also reduce the charge state to 1^+ or even lead to neutralisation.

Next to the mentioned three-body recombination, a major mechanism for the loss of ions is diffusion to the walls of the target chamber. Also, plasma screening and space-charge effects could lead to a decrease of the evacuation efficiency, especially at high ionisation rates in the gas cell. These problems are discussed in section 5.1.3.

5.1.3 Problems of the IGISOL technique

Recombination losses

From the very beginning of the ion guide development, it was realised that the ionisation of the stopping gas by the primary beam as well as by recoiling reaction products results in a major important loss that is neutralisation due to three-body recombination between the singly charged ions, free electrons and the neutral buffer gas. Taking the case of ion-electron pairs that are created in a gas cell filled with helium, the rate of the three-body ion-electron recombination $X^+ + e^- + He \rightleftharpoons X^* + He$ depends on α, the recombina-

tion coefficient (cm^3s^{-1}), and on Q, the number of ion-electron pairs created ($cm^{-3}s^{-1}$). Due to the fact that most of the ions are buffer gas ions, the recombination process is dominated by the recombination coefficient of the buffer gas itself. If a beam of ionising radiation of constant intensity passes through the gas cell, the three-body ion-electron recombination reaches an equilibrium for the ion-electron density with a time constant t [37]

$$t = \frac{1}{\sqrt{Q\alpha}} \tag{5.1}$$

At saturation, the density $n = n_{ion} = n_{electron}$ is then

$$n = \sqrt{Q/\alpha} \tag{5.2}$$

For an argon ion in 0.5 atm argon, the recombination coefficient α is 10^{-6} cm^3s^{-1}. For the case of the gas cell at Louvain filled with 500 mbar of argon gas, the ion-electron pair production rate Q equals 2.77×10^{15} at an intensity of 1 pμA of the 30 MeV proton projectile beam [23], leading to a saturation time of 20 μs. It is thus clear that the ionising rate Q, the recombination coefficient α and the residence time of ions and electrons in the stopping gas will determine the recombination losses.

The presence of a high ionisation rate in the gas cell and the three-body recombination that stems from it, is invoked in the literature to explain the loss of ion-guide efficiency at high primary beam intensities. The dependence of the ion-guide efficiency on the intensity of a $^{58}Ni^{10+}$ primary beam was investigated experimentally at Louvain-la-Neuve for an argon buffer gas cell (see figure 5.3). For the case "laser off" (which corresponds to the extraction of $^{58}Ni^{1+}$ ions that are directly thermalised with the IGISOL technique), one observes that the efficiency drops below 1 % when the current of the heavy-ion beam reaches 10^5 pps. The value of Q is then equal to 10^{11} ion-electron pairs $cm^{-3}s^{-1}$ [23].

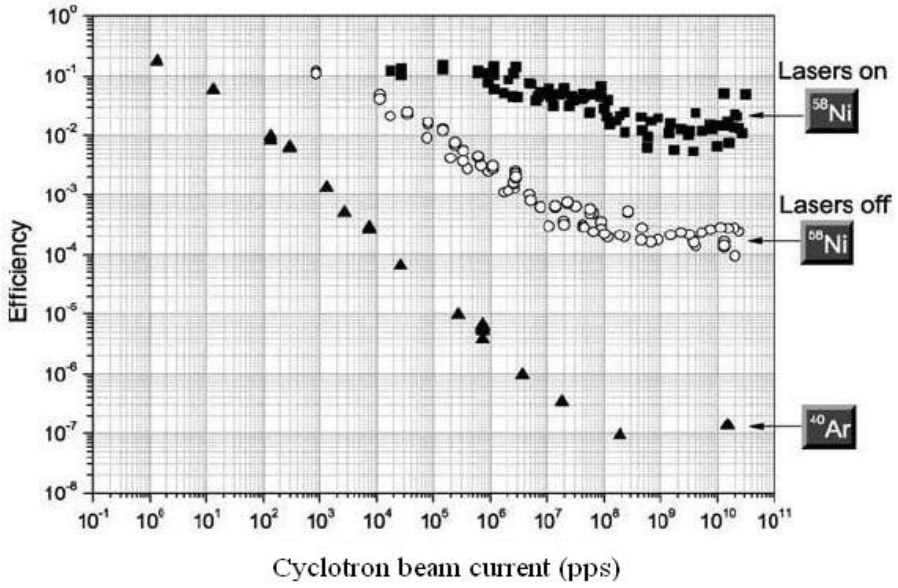

Figure 5.3: Dependence of the ion-guide efficiency at Louvain-la-Neuve for extraction of $^{58}Ni^{1+}$ with laser ionisation (squares) and direct thermalisation (circles) on the $^{58}Ni^{10+}$ primary beam intensity [23].

Space-charge effects

The extraction time of the ions from the gas cell in the IGISOL technique can be reduced by applying electrical DC and RF fields in the cell that drag the ions towards the exit hole and at the same time prevent them from diffusing to the walls, thus reducing the decay losses of short-lived isotopes as well as sticking losses. Such a gas cell shares the principle of the classical ionisation chamber where the electrons are rapidly collected on the electrode, such that we may reduce the losses due to three-body recombination. However, the much higher velocity of the electrons compared to the ions could lead to the accumulation of positive charges and hence the emergence of space charge in the gap of the electrodes.

The main feature of space-charge is its density, which for an incoming

pulsed beam depends on the time. This dependence disappears after a specific time period, which can be calculated for a plane parallel geometry by the following expression [23]:

$$t_{sat} = \frac{\overline{\rho_+}}{Q} \simeq \frac{d_0}{2v_+} \tag{5.3}$$

Here, $\overline{\rho_+}$ is the average positive space-charge density in steady state condition, d_0 is the distance between the electrodes and v_+ is the drift velocity of the positive ions. After this time period, the positive space charge density reaches saturation, which means that the charge creation rate and the charge collection rate are balanced. The potential which is induced by the space charge and which screens the applied voltage is given by [37]:

$$V_{ind} = \sqrt{\frac{eQ}{4\epsilon_0\mu_+}d_0^2} \tag{5.4}$$

Here, ϵ_0 is the di-electric constant for vacuum and μ_+ is the mobility of the ions in the gas cell, which depends on the temperature and pressure of the gas:

$$\mu_+ = \mu_0\frac{T}{p \times 273} \tag{5.5}$$

In this formula, p is the pressure in atmosphere, T is the temperature in K and μ_0 is the mobility of the ions in the gas at normal conditions ($T = 0°$C and $p = 1$ atm).

The space charge limit is reached when complete screening of the applied electrical field by the induced field occurs, such that the net electrical field at the anode equals zero, the collection of charges in its vicinity stops and three-body recombination is taking over in this region. If the ionisation rate Q is further increased, a field-free zone will develop and charges created in this zone will freely recombine. For a given parallel plate chamber, the Q value

corresponding to the space charge limit can thus be calculated by formula 5.4.

Instead of a plane parallel geometry, the cross-section view of a realistic design used in Louvain-la-Neuve is drawn in figure 5.4. Because the metallic walls of the gas cell are grounded on all sides, it can be shown that the electrical field in this geometry can be described by an equivalent cylindrical geometry. Calculations carried out by Facina *et al.* [23] indicate that for the field map of figure 5.4, space charge starts developing at ionisation rates of $Q = 10^{10}$ cm^{-3}s^{-1}.

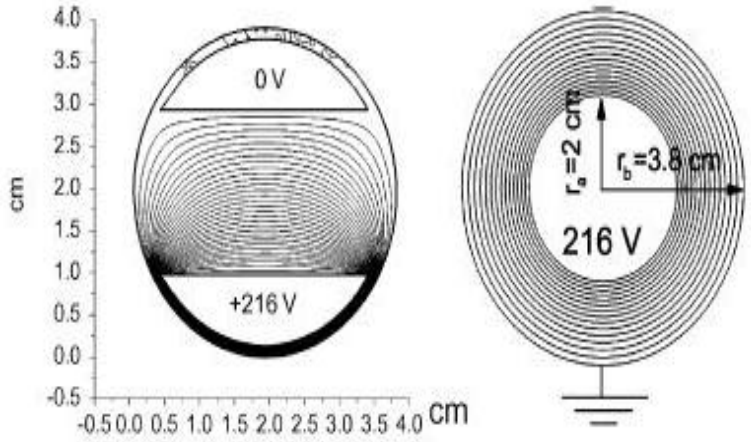

Figure 5.4: Cross-section view of the electrode geometry at Louvain-la-Neuve (left) and equivalent cylindrical geometry (right) [23].

A high ionisation rate of the stopping gas could lead to the formation of an ionised plasma. The high density of electrons will then lead to a high recombination rate and the efficiency for storing and transporting ions will decrease. A consequence of plasma formation is the appearance of collective effects and in particular ambipolar diffusion where the ions and electrons

move with the same velocity $v_{electron} \approx v_+$. Moreover, the plasma will shield the electrical field over a screening distance which is the Debye length, given by the expression [37]:

$$\lambda_D = 69\sqrt{\frac{T_e}{n_e}} \tag{5.6}$$

with T_e the electron temperature in K and n_e the electron density in cm^{-3}. In the gas cell, a necessary condition for plasma formation is that the Debye length of the plasma is smaller than the dimensions of the cell. For the case of the ion guide at Louvain-la-Neuve, a 40 MeV He^{++} projectile beam of 15 pμA transfers a sufficient amount of energy to the electrons so their temperature can be as high as 4600 K. The Debye length is then equal to 1.4×10^{-3} mm [33].

A second effect that emerges with the plasma effect is that the plasma shields itself from external fields through the formation of a plasma sheath. It also leads to a distortion of the electrical field, which may become worrisome in the extraction region of the ion guide. While the Debye length is a measure for the penetration of external fields in the plasma, a necessary condition for the plasma sheath to exist is that the number of charges in the plasma sheath region N_D is much larger than 1. This number is given by [37]

$$N_D = 1380\frac{T_e^{3/2}}{n_e^{1/2}} \tag{5.7}$$

Taking the same conditions as above, N_D is about 125 particles. The presence of local plasma pockets in the gas cell is therefore likely at high primary beam intensities. The importance of this plasma should not be overestimated, however, since the collision frequency with neutral particles remains high (it is already of the order of 10^9 s^{-1} in argon at normal conditions). This effectively dilutes the plasma [33].

Diffusion to the chamber walls

Beside the losses mentioned above, the diffusion of recoil ions to the chamber walls also causes losses because of neutralisation or the particles may simply stick to the wall. Diffusion is slower at higher gas pressures and for heavier stopping gasses. Obviously, diffusion losses are also reduced by reducing the evacuation time of the gas cell.

In situations where the plasma effect is small, the diffusion of ions to the cell walls becomes the main loss mechanism of recoils. This is confirmed by measurements when an α-decay recoil source is put into the gas cell. For optimum conditions, almost 100 % of the α-decay recoils should leave the ion guide as singly charged ions [11]. However, because of diffusion and sticking to the walls the measured efficiency of recoils leaving the ion guide was only 20 %. This means that 80 % of the recoil ions diffused and stuck to the walls of the chamber. Other experiments have put an upper limit of 60 % on diffusion losses. It is clear that the precise value depends strongly on the geometry of the gas chamber and the gas flow. In many measurements, the efficiency increases with the pressure of the stopping gas. The losses are further reduced by increasing the flow rate or using a heavier stopping gas.

The efficiency that is obtained by the IGISOL approach depends on many parameters, which involve the gas cell design, the beam properties, the purity of the gas and the extraction conditions. In addition, the conditions in which the ions are slowed down vary greatly for different reactions. It is therefore difficult to compare the results obtained by different laboratories or even within the same laboratory if the above mentioned parameters are not controlled within a reproducible way. For every ion guide, it is thus necessary to investigate its design in detail and eventually simulate it to estimate or understand its performance. Before doing so, we first discuss in the next section the empirical ways in which the gas cell can be adapted for different reactions.

5.1.4 Ion-guide design for different reaction types

Light-ion induced fusion-evaporation reactions

The first ion-guide systems were designed for reaction products from light-ion induced fusion-evaporation reactions. Because the products of these reactions recoil in the forward direction, the primary beam generally penetrates into the stopping chamber and ionises the buffer gas. If we do not require the suppression of the primary beam, an ion guide for this type of reactions is very simple: it is basically a cylinder with a target at one end and an exit hole in one of the sides. Typical efficiencies between 1-10 % have been achieved in this case for proton-induced reactions [11].

Heavy-ion induced fusion-evaporation reactions

For this type of reactions, the efficiencies are considerably smaller than those that are observed for light-ion induced reactions. This is due to the less efficient stopping of more energetic recoils and also to ionisation of the buffer gas by the heavier primary beam. The effect is witnessed already for α- induced reactions [8, 11]. The ionisation of the buffer gas leads to the neutralisation through recombination of the radioactive ions of interest during their transport in the gas as well as the distortion of the electrical field that may be applied in the extraction region of the ion guide, as discussed in section 5.1.3. Without suppression of the accelerator beam, the efficiency of the ion guide drops to about 0.01 % (for helium buffer gas) [11].

Two solutions have been employed to overcome the effect of the strongly ionising beam. The first one was applied at INS Tokyo [51] and then RIKEN, Japan [21, 27]. The evaporation residues were separated in-flight from the primary beam in a gas-filled dipole magnet and then stopped in a gas cell. The first experiments reached efficiencies above 10%. A similar setup, operating at Argonne National Laboratory, USA, was reported to reach an

efficiency of 40% [8].

A second way to overcome the effect of the ionisation of the buffer gas was applied originally at the SARA facility at Grenoble, France. Called the shadow method, the primary beam is separated from the evaporation residue by the difference in their angular divergence along the beam axis. In this way, an overall efficiency of nearly 1 % was achieved.

Besides these two methods, we can use selective laser ionisation to re-ionise the atom cloud that is stored in the gas cell after its complete neutralisation by three-body recombination has taken place. This approach will be presented in section 5.2.

Fission reactions

Fission fragments recoil out of the fissile target isotropically and with high energy. This allows to separate the stopping volume from the target zone by a thin foil. In this way, the accelerator beam does not pass through the stopping volume and ionisation of the buffer gas is avoided. A schematic drawing of the fission ion guide operating at Jyväskylä is shown in figure 5.5.

In this design the 15 mg/cm^2 uranium target is tilted by 7 degrees with respect to the beam direction, yielding an effective thickness that is as high as 120 mg/cm^2. Employing a 30 MeV proton beam the fission rate in the target is about 3×10^9 fissions /sμC. A quantitative measurement of the yield for the ^{112}Rh fission product gives a total efficiency of 0.02 % at a beam intensity of 10 μA. This corresponds to a yield of about 10^5 ions /s. It has been observed in recent experiments at higher beam intensities that the yield does not scale linearly, but rather with the square root of the beam intensity. The reason for this is not fully understood, but it is likely that ionisation of the gas generated by the fission fragments themselves passing through the stopping volume is responsible for this effect.

Finally, we would like to emphasise that the application of the ion-guide

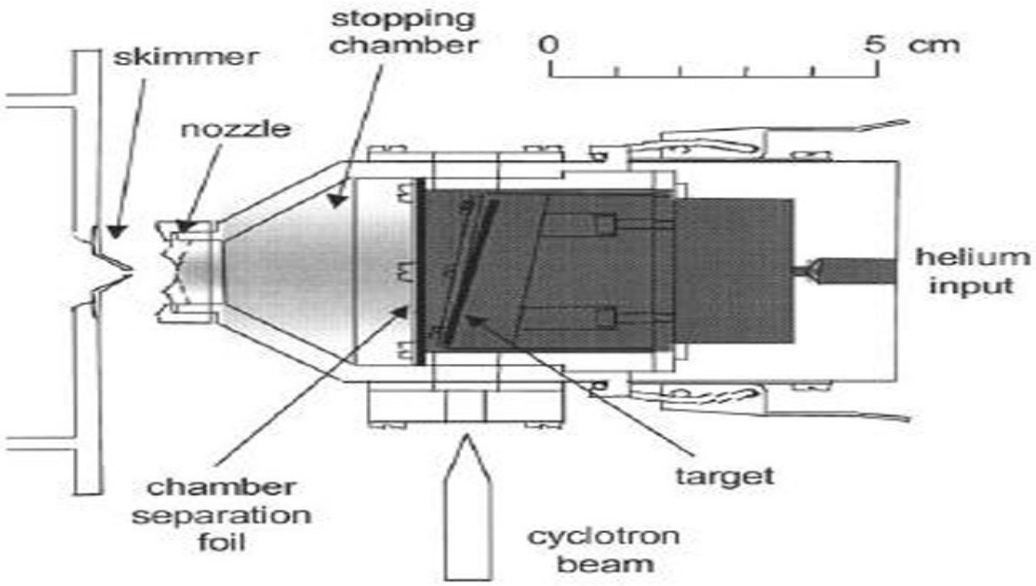

Figure 5.5: The ion guide used for fission reactions at Jyväskylä [11].

technique to the production of radioactive beams in the case of photo-fission has never been investigated before. One of the purposes of this thesis is to study the possibility to use the ion guide for the ALTO project on the basis of fission reactions induced by bremsstrahlung. The results obtained from the calculations that we shall present later on (see section 5.3.2) will give us information on the design of a future photo-fission ion guide.

5.2 The laser ion-guide

5.2.1 Principle of the laser ion guide

Most experiments at on-line mass separators are limited by isobaric contamination of the final beam. When fission reactions are used as the primary production mechanism, the production of exotic neutron-rich isotopes is overwhelmed by more stable isobars. Also beams of extremely neutron-deficient

isotopes produced by heavy-ion induced reactions, suffer from the same problem. It is therefore imperative to purify the beam as much as possible, which means first of all, being selective in the production process. The issue can be overcome to a significant extent by relying on resonance ionisation with lasers.

On the other hand, to study short-lived nuclei that lie far from the β-stability line, a fast extraction of the reaction products is required. In this respect, the ion-guide technique is well suited because of the advantageous extraction times of ions that are as fast as 10 to 100 ms. However, its application may seem rather limited because of the low efficiency, partly due to neutralisation of the ions in the buffer gas (see section 5.1).

An attractive solution is offered when the neutral atoms are re-ionised by resonant photo-ionisation with lasers, as done in the resonance ionisation laser ion source (see section 2.2.1). The technique that combines the ion-guide and the resonance ionisation laser ion source is called the laser ion guide. When moreover a mass separator is coupled to the laser ion guide, one can deliver in principle isotopically and isobarically pure ions. Depending on the characteristics of the laser system, it is possible to obtain an ionisation efficiency that is near unity for about 80 % of all elements, *i.e.* every atom that is irradiated by the lasers will be ionised [53].

Figure 5.6 schematically shows the different pathways for a two-step two-color ionisation. The atoms, which are thermalised in the ground state, are excited by the first-step laser λ_1 to an intermediate level. Then three ways are possible. The second-step laser λ_2 lifts the excited atoms into an auto-ionising state (a discrete multi-particle state in the continuum that rapidly decays by emitting an electron) or directly into the continuum. The atom may also be excited in a high-lying Rydberg state, from where collisions with the buffer gas atoms result in ionisation. Of the three pathways, ionisation through Rydberg or auto-ionising states is preferable since the photo-ionisation cross

section for these states is 10 to 100 times larger than for excitation to the continuum [30].

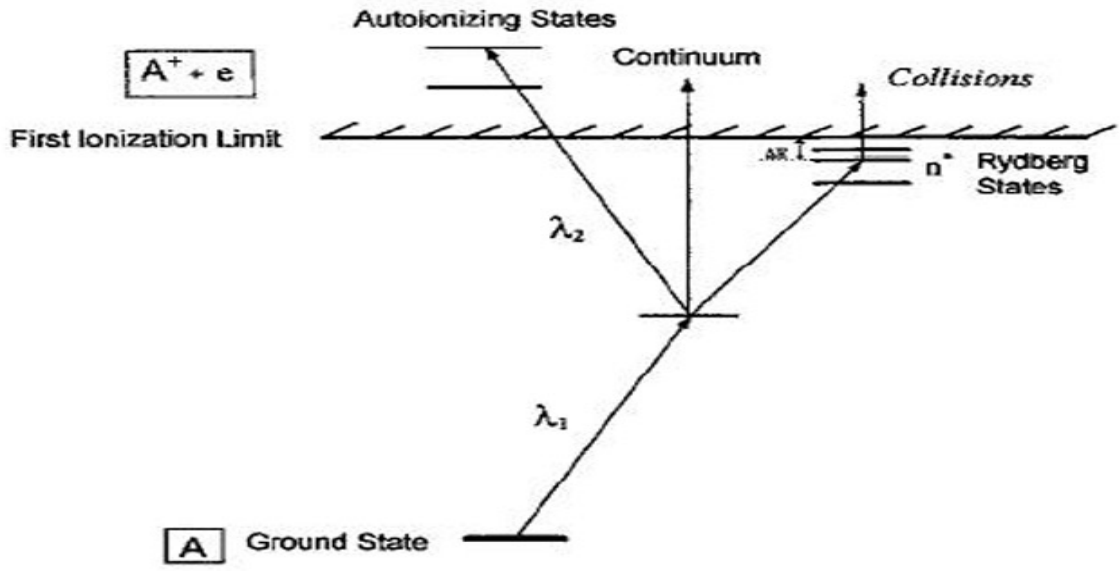

Figure 5.6: Different pathways for resonant laser ionisation [30].

In order to obtain high ionisation efficiencies, a relatively high laser power is needed. In practice, for this reason pulsed lasers are used. These lasers have one major drawback, namely their low duty cycle ($10^{-4} - 10^{-7}$). Since the production of radioactive ions at many isotope separators is continuous, the maximum overall efficiency will not exceed 10^{-4}. However, the laser ion guide method solves this problem since it allows us to store atoms as well as 1^+ ions in the buffer gas for long enough times between the laser pulses and extract them out of the gas almost at will by means of an electrical field.

From these facts, we can conclude that the laser ion guide technique satisfies the three main requirements of an ISOL facility that are efficiency, selectivity and rapidity.

5.2.2 Implementation of the laser ion guide

A schematic layout of the laser ion guide is shown in figure 5.7. The operational principle is based on the selective laser resonance ionisation of nuclear reaction products stopped in a high-pressure noble gas [30, 53, 25]. The accelerated beam hits a thin target that is located in a chamber filled with noble gas. The recoil products from a fusion-evaporation or fission reaction are initially thermalised as neutrals or 1^+ ions. After a few milliseconds, however, all ions are neutralised due to the recombination with free electrons that are created by the primary beam [12]. If we make the transport time from the target area to the laser ionisation zone longer than the survival time, all the reaction products will be effectively neutralised by the time they arrive in the ionisation area. The atoms of interest are then selectively ionised by the laser light, while the other atoms remain essentially unaffected. The ions are subsequently transported by the gas flow through the exit hole, behind which most of the noble gas is removed by differential pumping. The ions are meanwhile accelerated towards the analyzing magnet of the separator.

The procedure results ideally in a pure beam that is free of unwanted isotopes and isobars. Note that if the primary beam does not pass the ionisation area, this region will be mostly free of secondary electrons and the ion-survival time against recombination will surpass the evacuation time of the ion from the gas cell [55].

By choosing the volume of the ionisation chamber and the exit-hole diameter in such a way that the evacuation time τ_{evac} of the ionisation region equals at least the time between two laser pulses $\tau_{rep} = \nu_{laser}^{-1}$ and that τ_{evac} is smaller than the ion-survival time τ_{ion}, one obtains an optimal system:

$$\tau_{ion} \geq \tau_e \geq \tau_{rep} \tag{5.8}$$

In this case every atom is irradiated at least once by the laser and every

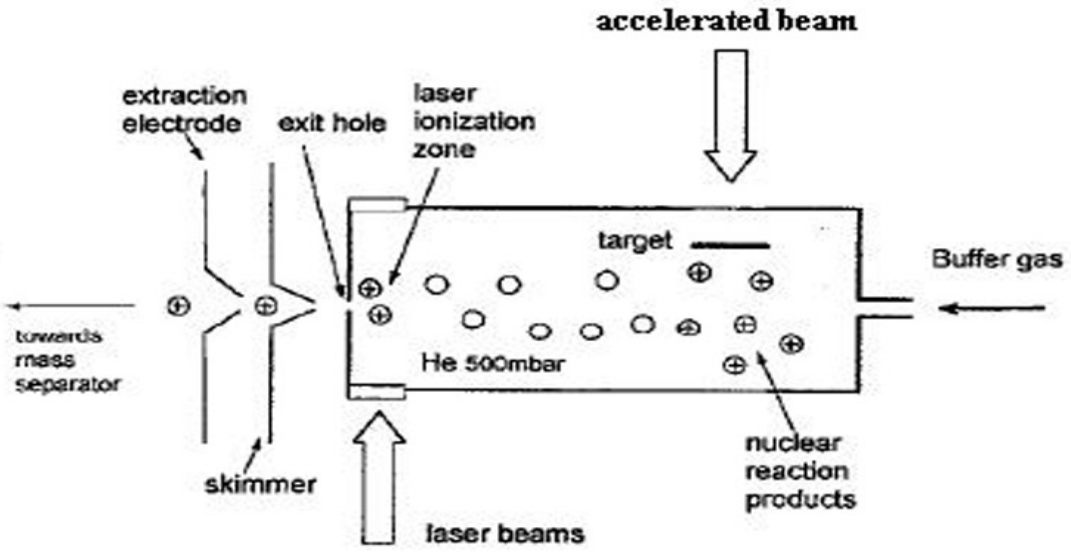

Figure 5.7: Schematic layout of the laser ion guide at Louvain, Belgium.

ion that is created will survive its transport to the exit hole. In order to stop recoil products from heavy-ion fusion-evaporation reactions and obey the time relations above, pressures in the target chamber P_{target} of at least 500 mbar have to be used. This is a factor of five higher than in conventional ion-guide systems without laser ionisation [53]. The volume of the ionisation region V_{ion} (in cm^3) is determined by the laser repetition rate [53]:

$$V_{ion} = \tau_{rep} \frac{Q_{max}}{P_{target}} \times 1000 \tag{5.9}$$

Here Q_{max} is the maximum gas load of the separator (typically 100 mbar l/s).

The processes that cause a reduction of the efficiency of the laser ion guide are the same as for the ion guide (see 5.1.3). In addition, when a recoil atom thermalises in a metastable state while the laser wavelength is tuned to ionise the ground state of the atoms, it will be unaffected by the laser light.

For example, in the reaction ^{54}Fe(^{3}He,2n)^{55}Ni with a 25 MeV ^{3}He beam and helium buffer gas at 500 mbar, it was experimentally observed that only 70 % of the radioactive ^{55}Ni atoms were thermalised in the ground state [30].

5.3 Simulation of buffer-gas ionisation

With the arrival of the ALTO accelerator, a programme for studying the nuclear structure of refractory elements can be opened at IPN Orsay. These elements, for example cobalt and nickel, which have atomic numbers $Z = 27$ and 28, respectively (the latter being a magic number), are very interesting candidates for nuclear structure research. However, refractory elements are in general difficult to produce due to their high melting point, leading to the need for high temperatures to make them volatile and release them from a thick target. An extraction method that is based on a thin target is needed and among the thin-target techniques, the laser ion guide seems a promising approach for producing the intensive and selective beams that evoke our interest (see section 5.2).

At ALTO, we have undertaken preliminary design studies for a laser ion guide. Simulations were carried out with the GEAN-4 code [22] to investigate several of its parameters. In this section, we focus on the calculation of the energy deposit from the 50 MeV incident electron beam at ALTO in a gas cell, as well as from fission fragments. We evaluate the ion-electron pair production rate in the buffer gas it results in. Consequently we shall be able to estimate the performance of the ion guide for a photo-fission scenario. Simulations for the gas cell at Louvain-la-Neuve, Belgium, with a 30 MeV primary proton beam were done for comparison. In addition, in order to move towards the SPIRAL-2 project at GANIL, in which fission will be induced by fast neutrons generated from the break-up of deuterons in a thick target, we also performed a simulation for that case.

5.3.1 Primary proton beam: the gas cell at Louvain-la-Neuve

Geometry

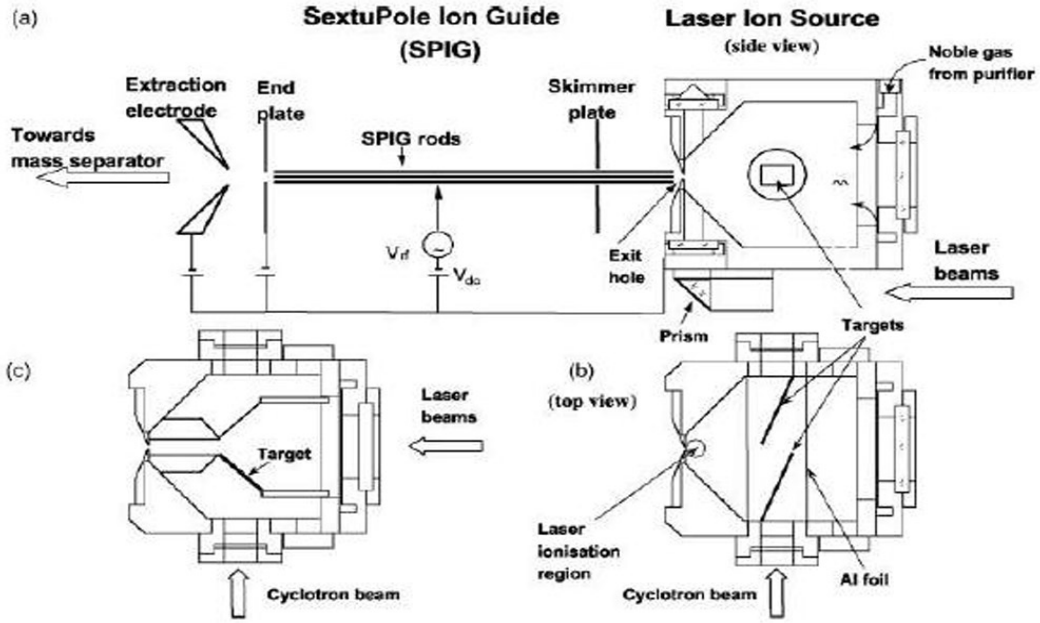

Figure 5.8: Drawing of the laser ion guide at Louvain-la-Neuve. Parts (a) and (b) show the cell used for fission, (c) for fusion reactions [31].

The parts (a) and (b) of figure 5.8 show the design of the laser ion guide at Louvain as it is used for fission reactions. Its volume is around 92 cm^3. The gas cell is filled with 500 mbar argon gas. Two 10 mg/cm^2 natural uranium foils are placed in it, tilted at an angle of 20° relative to the primary proton beam. The visualisation of the gas cell in GEANT-4 is shown in figure 5.9.

Energy deposit of 30 MeV protons in the gas cell

In order to calculate the energy deposit in the gas cell, the GEANT-4 physics processes for protons (multiple scattering, ionisation and energy loss of a

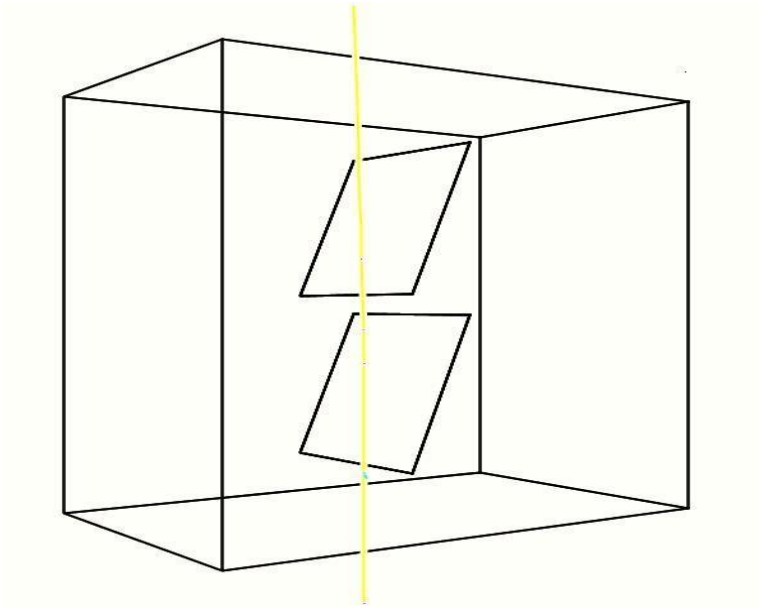

Figure 5.9: Visualisation of the Louvain-la-Neuve gas cell in GEANT-4.

charged hadron, hadron elastic and inelastic processes) are activated. The standard electromagnetic (EM) processes are assigned to the secondary charged particles that are produced by the interaction between the proton beam and the argon buffer gas or the uranium target. Table 5.1 shows the mean energy loss dE/dx and the ion-electron pair production rate Q in the proton beam path at a gas pressure of 500 mbar and a proton beam intensity of 1 μA/cm^2 for two different physics cases: EM interaction only and EM plus hadron elastic and inelastic processes for the proton. We used an average ionisation energy for the argon gas of 26.4 eV [54]. For the case of the EM interaction

Table 5.1: Mean energy loss dE/dx and ionisation rate Q in the gas cell of Louvain-la-Neuve for 30 MeV proton.

Physics case	dE/dx (keV/cm)	Q (pairs/cm^{3}s)
EM interaction only	11.16	2.64 $\times 10^{15}$
EM interaction plus others	10.79	2.55 $\times 10^{15}$

only, the results for the mean energy loss dE/dx and the ionisation rate Q are in good agreement with those of Ref.[23] calculated with the SRIM code, quoted as 11.7 keV/cm and 2.77×10^{15}, respectively. However, the calculation that does not take into account the hadronic processes of the proton will slightly overestimate the energy loss and the Q value in the buffer gas. Indeed, the proton may lose part of its energy in the uranium targets instead, which the EM calculation does not consider. Figure 5.10 shows the spectra for the energy deposit and for the energy of the secondary charged particles produced in the gas cell.

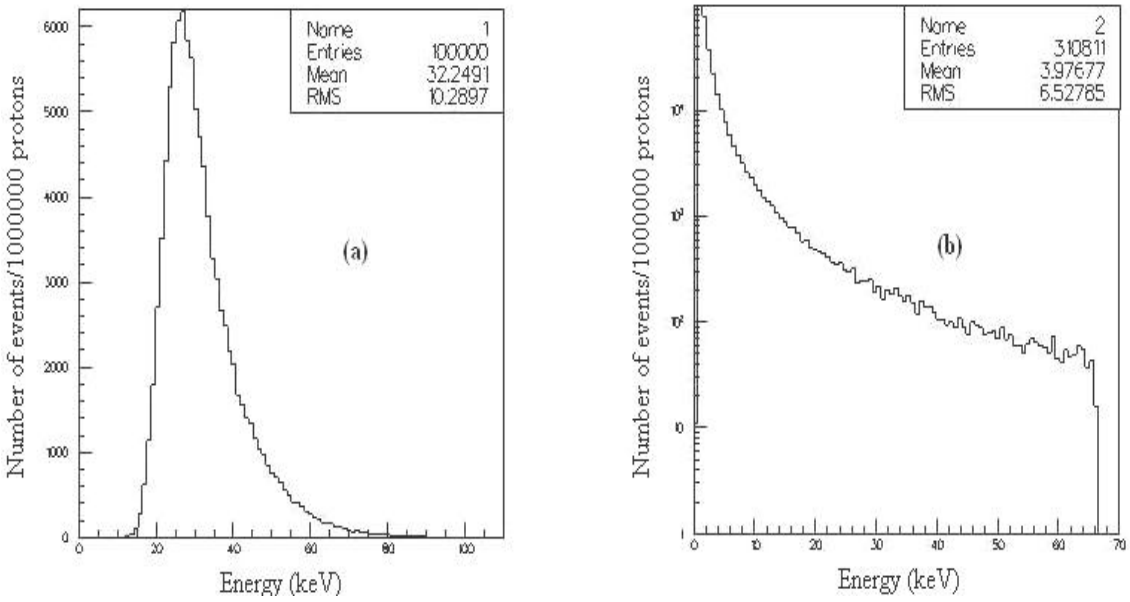

Figure 5.10: (a) Energy deposit spectrum for 30 MeV proton in the gas cell. (b) Energy spectrum of secondary charged particles produced in the gas cell.

5.3.2 Primary electron beam: the future gas cell for ALTO

Geometry

On the basis of the gas cell at Louvain-la-Neuve, we consider a geometry the total volume of which is of the same order. The proposed dimensions of the main rectangular body are $25 \times 40 \times 40$ mm^3, the volume of the rectangular extension where the gas flow enters measures $11 \times 40 \times 40$ mm^3 and the height of the pyramidal exit section equals 36 mm with a base of 40×40 mm^2. In this volume, we would place natural uranium plates and their fission would be induced by the bremsstrahlung generated by the interaction between the 50 MeV primary electron beam and a tungsten converter that is inserted in front of these targets (see Fig.5.13). The quantity and the position of the fission targets is selected on the basis of an optimised yield calculation by O. Bajeat at IPN Orsay [35]. The calculation indicates that the highest yield is obtained for a close geometry and a focused electron beam. Figure 5.11 shows the photo-fission yields for a vertical and a horizontal target placed at 5, 15 and 25 mm from the converter as function of the radius of the electron beam (a thickness of 8 mm is chosen for the tungsten converter such that the electron beam is stopped in it).

However, if we put the target too close to the converter, half of the fission fragments produced in the target will diffuse into the converter and will be lost. For this reason, we propose a minimum distance of 5 mm between the converter and the first vertical target, named V1. The calculated efficiencies for stopping a typical fission fragment of 100 MeV energy produced in a 15 mg/cm^2 uranium target are 23 % in 5 mm, 31 % in 10 mm and 40 % in 20 mm of 500 mbar argon gas. For thicker targets, the product of the target thickness and the percentage of recoils stopped in the gas does not increase any longer (see table 5.2) [35]. For our gas-cell prototype, we decide to place

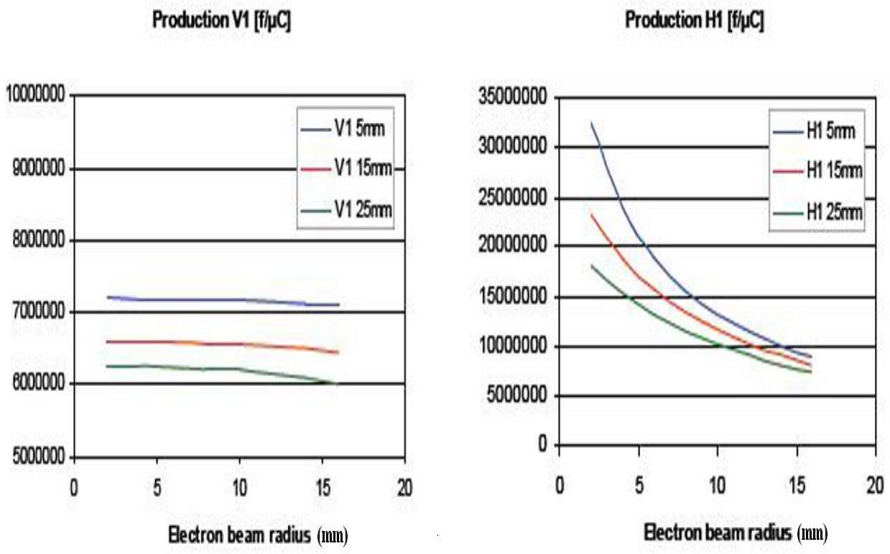

Figure 5.11: Fission yields for a vertical and horizontal target placed at different distances from an 8 mm tungsten converter as function of the radius of the electron beam.

4 vertical targets at successive intervals of 10 mm. The fourth target is thus positioned at 35 mm from the converter.

For a photon beam with an opening angle of 15° (which comprises most of the bremsstrahlung intensity) and a radius for the electron beam of 2 mm, the area of the fourth target irradiated by the photons is circumscribed by a circle with a diameter of 23 mm. We therefore limit the dimensions of the vertical targets to 25×25 mm^2. In order not to lose the fission fragments that recoil out of the last target, we leave a space of 5 mm between this target and the wall of the gas cell, so the depth of the cell becomes 40 mm.

Due to the focus of the electron beam, only one horizontal target that is placed in the beam axis can be efficient. The calculated fission yields for

Table 5.2: Stopping efficiency in 500 mbar argon gas of a 100 MeV fission fragment produced in the middle of a uranium target, for different gas and target thicknesses.

Uran target	10 mm Ar	20 mm Ar
10 mg/cm^2	34 %	49 %
15 mg/cm^2	31 %	40 %
20 mg/cm^2	23 %	
25 mg/cm^2	19 %	

a horizontal target at different heights above the beam axis as function of the radius of the electron beam are plotted in figure 5.12. The calculation corresponds to an electron current of 1 μA, the target dimensions are 25×40 mm^2 and it is placed parallel to the beam axis at a height of 0, 10 and 20 mm and 5 mm away from the 8 mm tungsten converter [35]. Based on this result, we plan to place one horizontal target of 25×40 mm^2 along the beam axis in the gas cell.

A drawing of the proposed gas cell for ALTO is presented in figure 5.13. The thickness of each of the five uranium targets is 15 mg/cm^2. The visualisation of the geometry of the cell in GEANT-4 is shown in figure 5.14.

So far the thickness of the converter was put at 8 mm to ensure that all electrons are stopped in it. In a next step we calculated the photo-fission yield by means of the Ficel code [24] and we found a maximum for the converter thickness at 3 mm (see figure 5.15, this particular calculation was done for five vertical targets of 40×40 mm^2). Indeed, for this thickness there is less photo-absorption in the tungsten slab. For the geometry described above with four vertical and one horizontal targets, a 3 mm tungsten converter and a 1 μA electron beam of 2 mm radius, we finally calculated a total photo-fission yield of 6.7×10^7 fissions /μC. In the first vertical target alone there are then 8.4×10^6 fissions /μC produced.

However, as mentioned in section 5.1.3, the ion-electron pair production

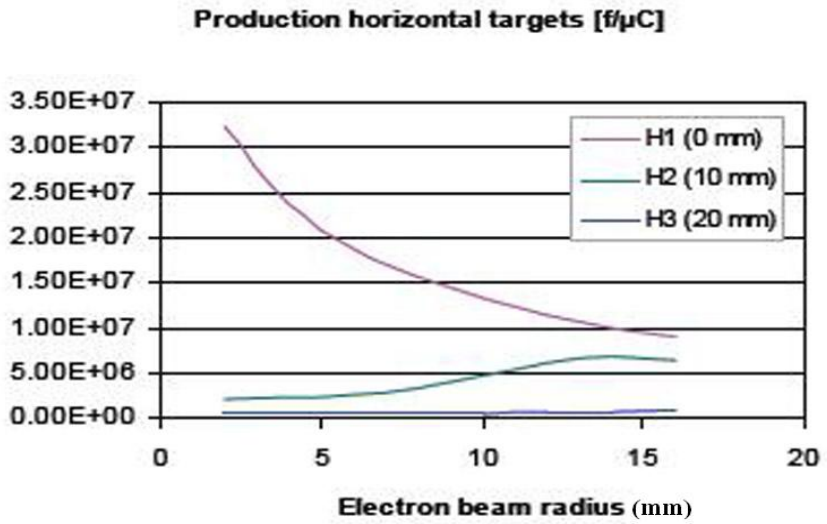

Figure 5.12: Fission yields for a horizontal target placed parallel to the beam axis at different heights as function of the radius of the electron beam.

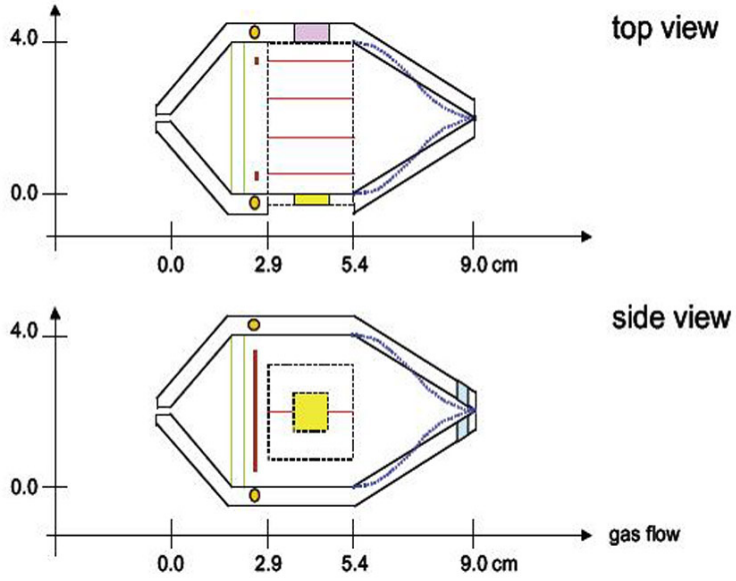

Figure 5.13: Proposed gas cell for ALTO at Orsay.

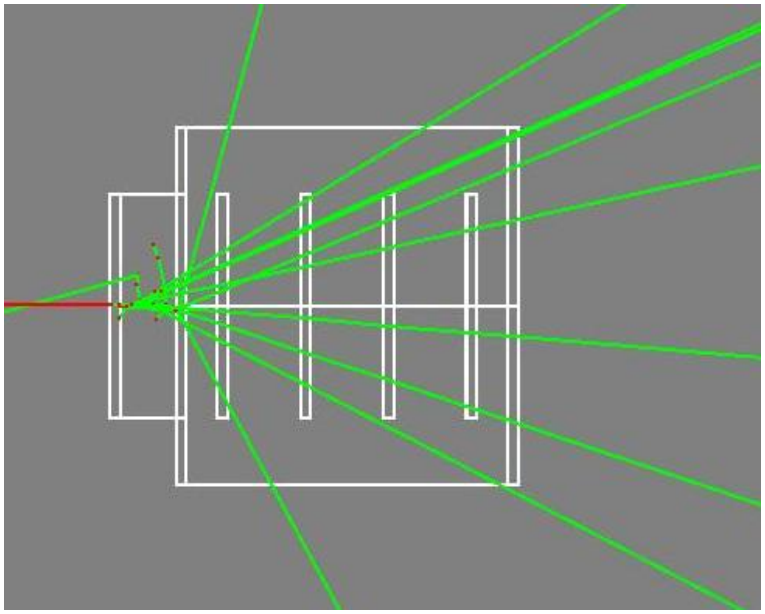

Figure 5.14: Visualisation of the proposed ALTO gas cell in GEANT-4.

rate (the ionisation rate of the buffer gas) plays a very important role in the efficiency of the laser ion guide. Therefore, it is necessary to perform further calculations to estimate this ionisation rate and achieve a compromise between the ionisation rate and the photo-fission yield. Besides, the Ficel code does not consider the creation of secondary particles nor does it take into account the contribution to the fission yield that is induced by neutrons produced from the photo-nuclear reactions (γ, n) or (γ, 2n). Thus, an independent calculation of the photo-fission yield in GEANT-4 is most relevant.

Bremsstrahlung distribution

In order to calculate the photo-fission yield, we first need to simulate the angular and energy distribution of the bremsstrahlung produced by the interaction between the 50 MeV electron beam and the tungsten converter.

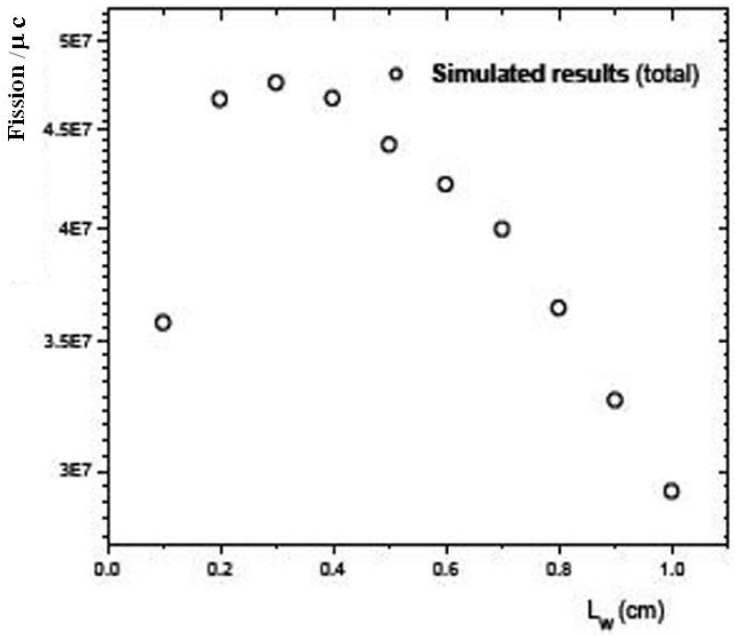

Figure 5.15: Fission yield in the gas cell as function of tungsten converter thickness.

In our calculation, the standard EM interaction processes of GEANT-4 are called and the beam radius is fixed at 2 mm. In figure 5.16, the energy spectrum and the angular distribution of the bremsstrahlung are presented.

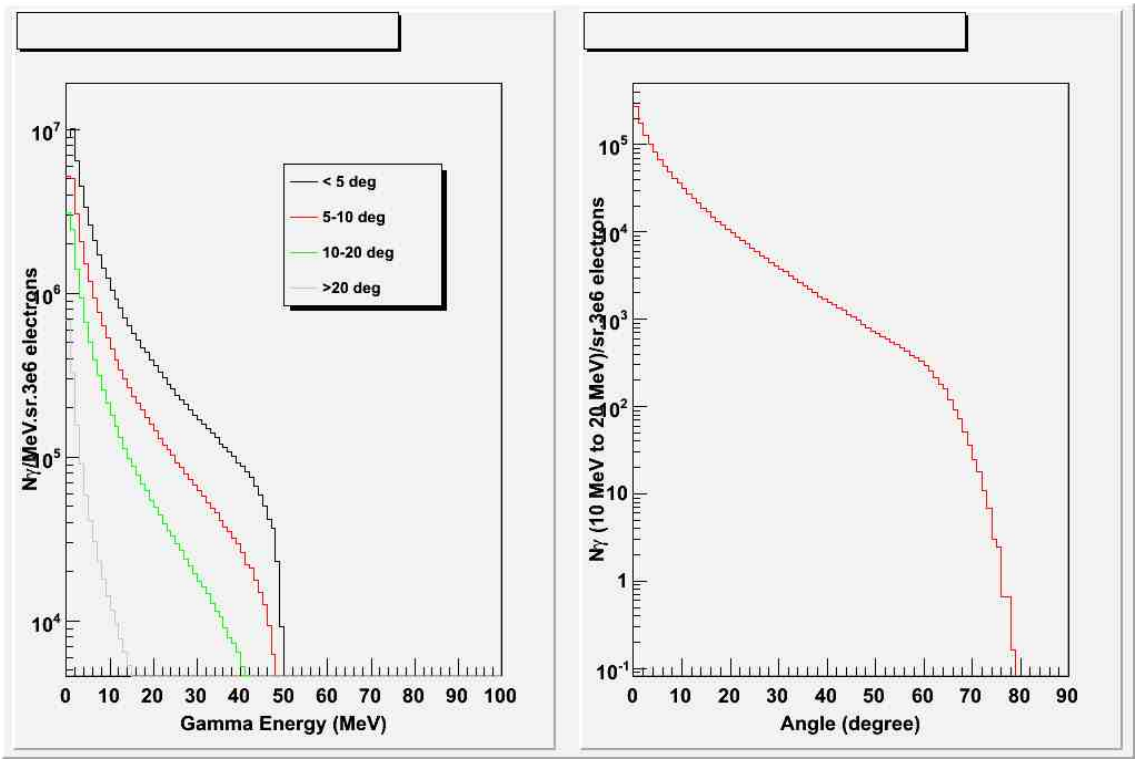

Figure 5.16: Energy and angular distribution of the bremsstrahlung produced by interaction between a 50 MeV electron beam and an 8 mm tungsten converter.

As can be seen, the bremsstrahlung with energies around the Giant Dipole Resonance of ^{238}U (which is near 15 MeV) is almost exclusively emitted under small forward angles. The full width at half maximum (FWHM) of the angular distribution is about 4°. The incident position of the photon on the first vertical target is shown in figure 5.17.

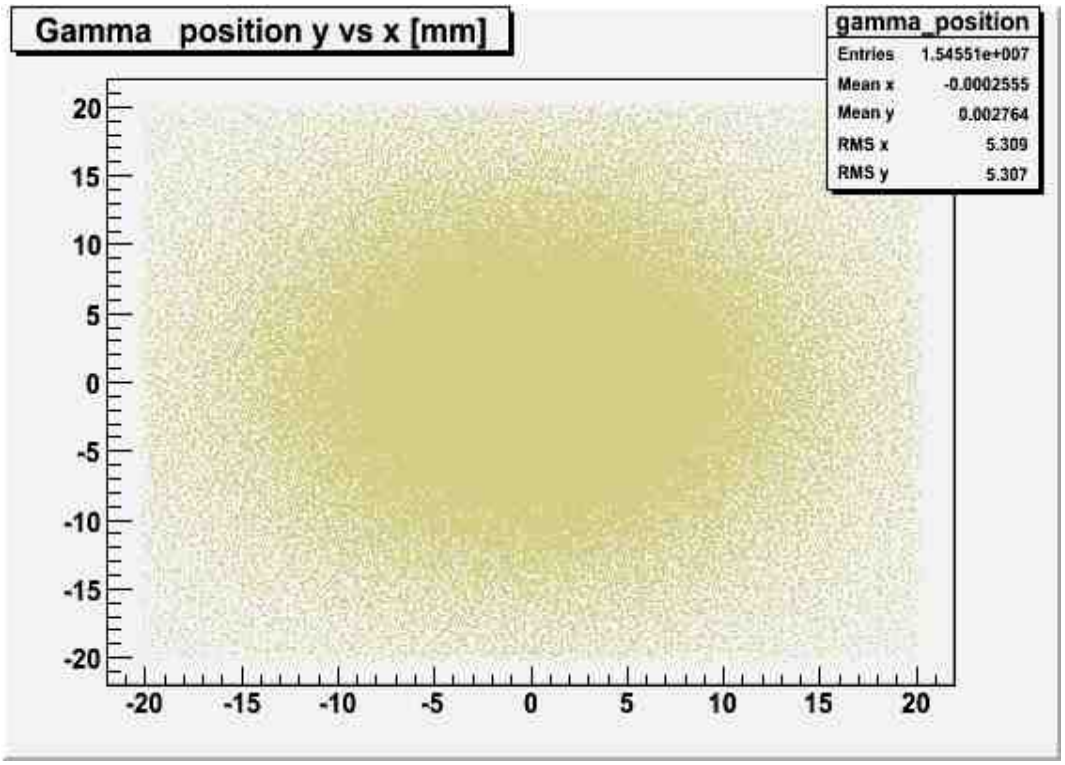

Figure 5.17: Incident point of the bremsstrahlung on the first vertical target.

Photo-fission, photo-neutron and neutron-induced fission yields

Unfortunately, the photo-fission process is not available in GEANT-4. Therefore, we have implemented a class, **G4PhotoFission**, which inherits from the GEANT-4 class **G4HadronInelasticProcess** to handle this physics process [43]. We specify a data set for this process through the **G4CrossSectionDataStore** class. The data for the photo-fission cross section of ^{238}U are taken from [16] and parameterised by a function that is the sum of two Lorentz-shaped functions:

$$\sigma\left(\gamma, F\right) = \sum_{i=1}^{2} \left\{ \frac{\sigma_m(i)}{1 + \frac{\left[E_\gamma^2 - E_m^2(i)\right]^2}{E_\gamma^2 \Gamma^2(i)}} \right\} \tag{5.10}$$

The data set, the fitting curve and its parameters are shown in figure 5.18.

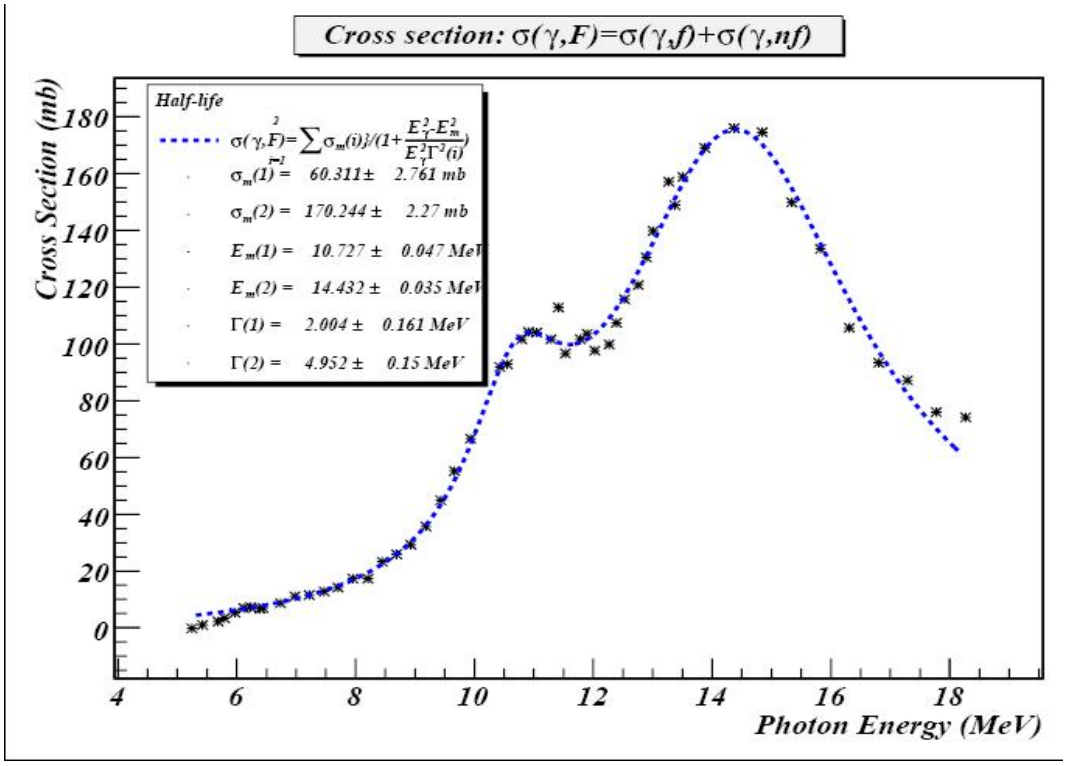

Figure 5.18: Data set and fitting curve for the photo-fission cross section.

Similarly, for the photo-nuclear reactions (γ,n) and (γ,2n), we have implemented appropriate classes to handle the processes and introduced the data sets for these reactions. The fitting curves of the cross-section data for these reactions on ^{238}U are presented in figure 5.19 [16].

We ran our calculation for 3 million events. The photo-fission yields of the four vertical and one horizontal targets in the gas-cell geometry of section 5.3.2 for different converter thicknesses d_W are listed in table 5.3. We observe that the yield of 8.3×10^6 fissions per second in the first vertical target, for a converter thickness of 3 mm, is in very good agreement with the result

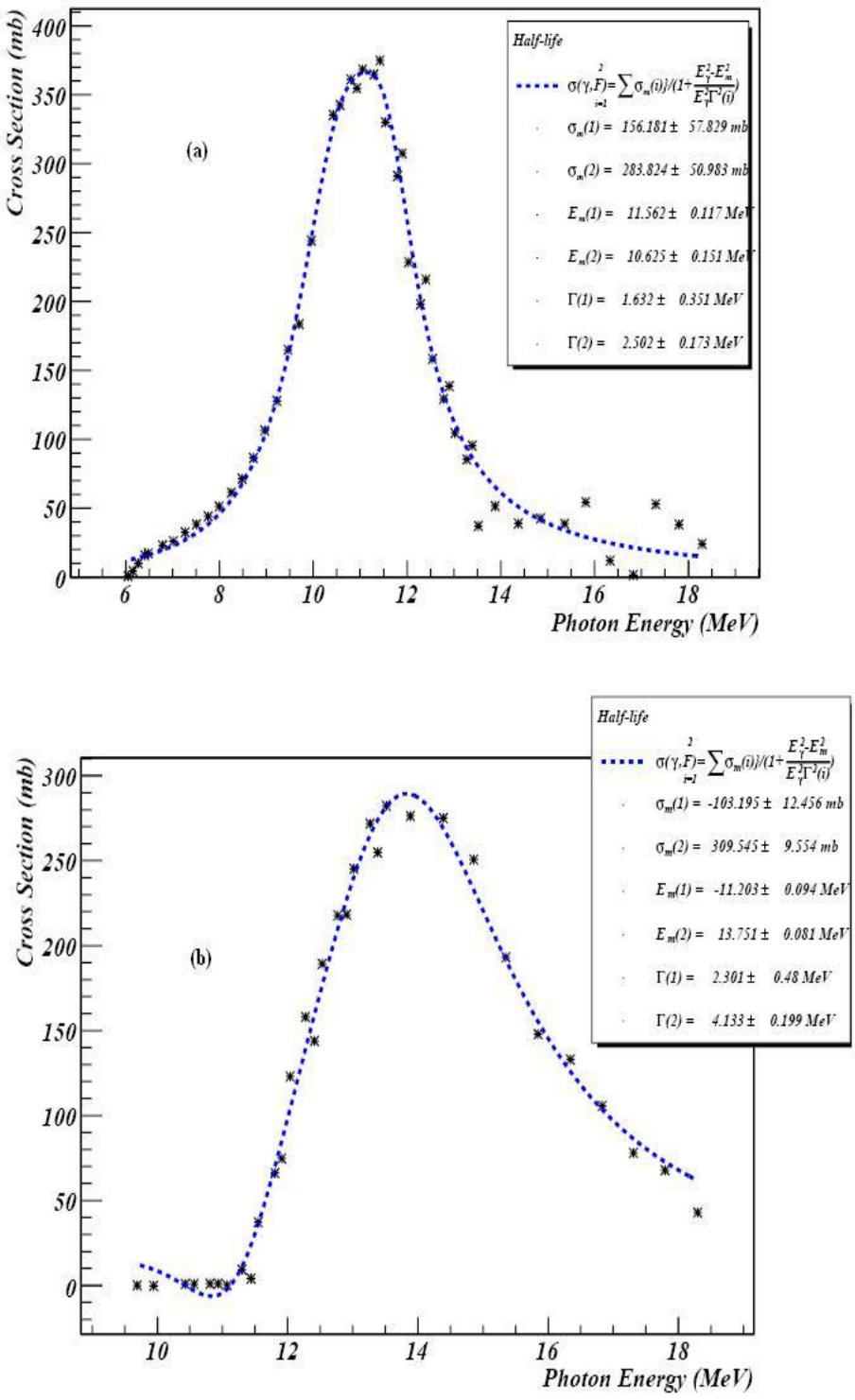

Figure 5.19: Data sets and fitting curves for the (γ,n) (a) and (γ,2n) (b) reaction cross sections.

from the Ficel calculation discussed in section 5.3.2. However, contrary to our earlier conclusions, the photo-fission yield of the targets placed farther away from the converter is higher with up to a factor two and the total yield equals 1.3×10^8 fissions /μC (even 1.5×10^8 for a tungsten thickness of 4 mm), instead of the 6.7×10^7 fissions /μC calculated with Ficel. This increase in yield clearly illustrates the importance of the secondary effects.

Table 5.3: Photo-fission yields of four vertical and one horizontal targets in the gas cell for different converter thicknesses d_W.

d_W (mm)	Photo-fission yield					
	V1	V2	V3	V4	H	Total
1	2.08 10^6	8.32 10^6	4.16 10^6	4.16 10^6	6.45 10^7	8.32 10^7
2	4.16 10^6	6.24 10^6	8.32 10^6	8.32 10^6	7.48 10^7	1.02 10^8
3	8.32 10^6	1.25 10^7	1.46 10^7	6.24 10^6	8.53 10^7	1.27 10^8
4	8.32 10^6	2.08 10^7	1.25 10^7	1.25 10^7	9.36 10^7	1.48 10^8
5	2.28 10^7	1.04 10^7	1.04 10^7	1.25 10^7	8.94 10^7	1.45 10^8
6	1.46 10^7	1.04 10^7	8.32 10^6	1.04 10^7	6.86 10^7	1.12 10^8
8	8.32 10^6	1.25 10^7	1.25 10^7	8.32 10^6	6.03 10^7	1.02 10^8

In figure 5.20, we present the total photo-fission yield in the gas cell as function of the converter thickness. From this figure, we see that the photo-fission yield reaches a maximum at $d_W \approx 4$ mm. The yield of neutrons produced by the photo-nuclear reactions (γ, n) and (γ, 2n) is shown in figure 5.21.

However, as mentioned earlier, the total energy deposit in the gas cell will have a strong influence on the efficiency of the ion guide. Therefore, in order to select the optimal converter thickness we also need to evaluate this energy deposit as function of the thickness of the converter. This work is discussed in the next section.

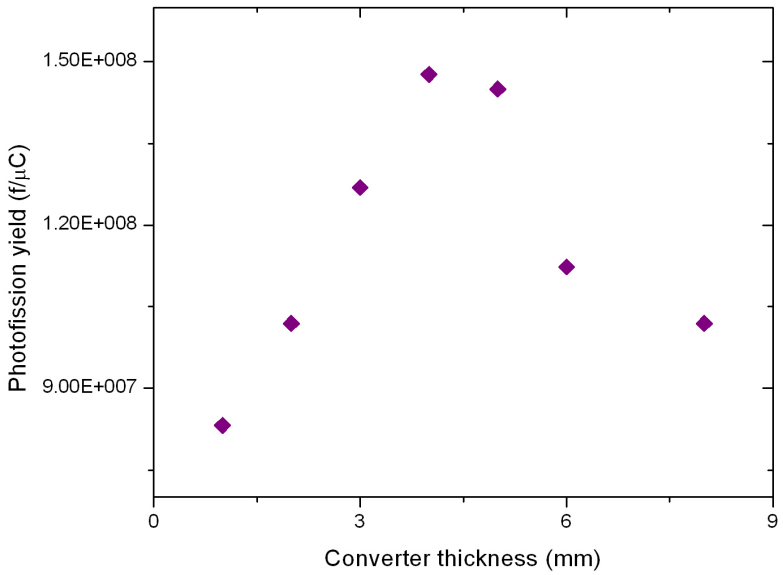

Figure 5.20: Photo-fission yield in the gas cell as function of converter thickness.

Energy deposit and ionisation rate

For the simulation of the energy deposit in the gas cell in Geant-4, we have chosen the standard electromagnetic interaction for the primary electron beam and included the creation of bremsstrahlung and secondary charged particles in the converter and the gas cell. The calculated energy deposit per electron in the converter and in the gas cell for different thicknesses of the converter is shown in figure 5.22.

The figure demonstrates that the range of the 50 MeV electron beam in tungsten is around 8 mm. As the electrons lose their energy in the converter, the energy deposit in the gas cell is smaller. The number of ion-electron pairs that are created by the beam could thus be reduced by incrementing the converter thickness, if we disregard for the time being the effect on the

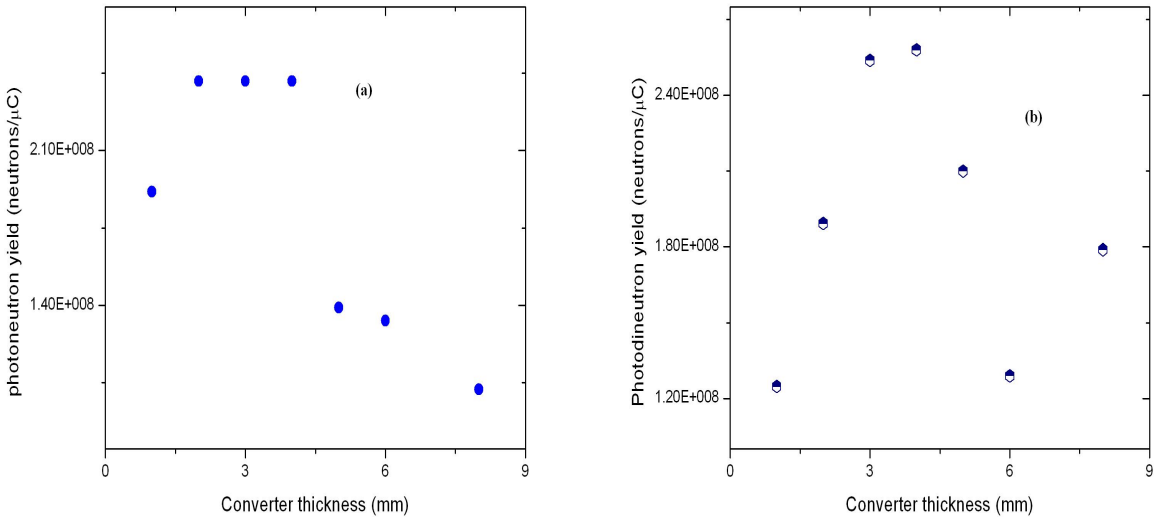

Figure 5.21: Yield of neutrons produced by photo-nuclear reactions (a) (γ, n) reaction and (b) (γ, 2n) reaction

production yield. For the case of the ALTO project, where the electron beam intensity is 10 μA, this behaviour is plotted in figure 5.23. At a converter thickness of 4 mm, we obtain an ionising rate of 1.20×10^{15} ion-electron pairs /cm^{3}s.

On the other hand, the number of secondary particles that would be generated in a thicker converter would also increase (see figure 5.24). Still, nearly all of the secondary charged particles produced in the tungsten converter would in turn be absorbed in it. This can be explained by the low energy of the secondary particles (see figure 5.25). At the same time, the high-energy γ-rays can travel through the gas cell almost without depositing any energy. Taken together, these reasons lead to an energy deposit in the gas cell of some keV per electron (see figure 5.26).

We note that the energy deposit of the photo-fission fragments them-

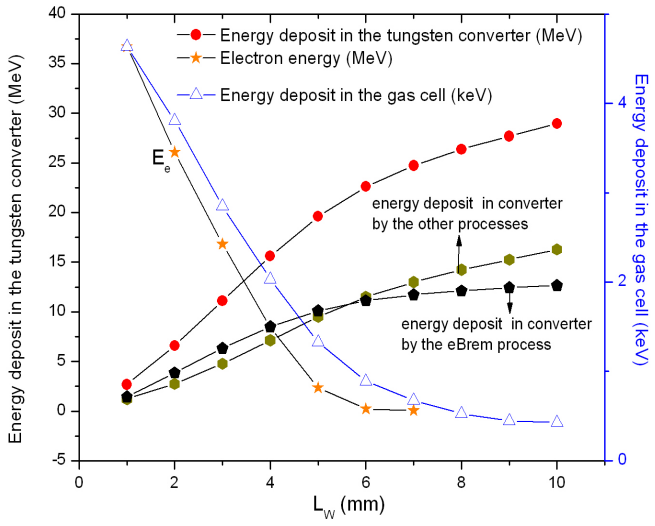

Figure 5.22: Energy deposit in the tungsten converter and in the gas cell per incident 50 MeV electron as function of the tungsten thickness. The mean energy of the electron as function of the depth is denoted by E_e.

selves also should be taken into account. Assuming that we use a 4 mm tungsten converter, we would produce 1.5×10^8 fissions (see table 5.3). By extrapolating the simulation result for the SPIRAL-2 gas cell of 7.7×10^{13} ion-electron pairs /cm^{3}s for 1.9×10^{11} fissions, presented in the next section 5.3.3, we obtain an ion-electron pair production rate from the photo-fission fragments equal to 6.1×10^{10} ion-electron pairs /cm^{3}s. This number is much smaller than the ionising rate provoked by the primary electron beam and its secondary particles (see figure 5.23) and therefore it can be ignored.

5.3.3 Primary deuteron beam: a gas cell for SPIRAL-2

In the SPIRAL-2 project, the use of energetic neutrons to induce fission of natural uranium for the production of neutron-rich nuclei is proposed. The high-energy neutrons in the range between 1 and 40 MeV will be generated by

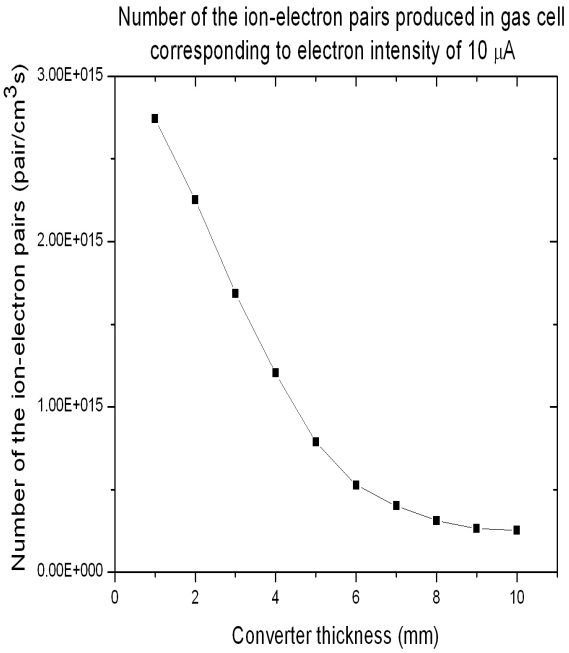

Figure 5.23: Number of ion-electron pairs created by the electron beam in the gas cell as function of tungsten converter thickness.

the break-up of 40 MeV deuterons, which are delivered by a linear accelerator, in a thick graphite target, the so-called converter. The main goal of the study presented in this section is to provide quantitative estimates of the ion-electron pair production rate induced by the neutron beam in a gas cell similar to the one proposed for ALTO (see section 5.3.2). The geometry of the projected SPIRAL-2 gas cell from the GEANT-4 visualisation is shown in figure 5.27.

The ionisation of the buffer gas might be induced by the primary deuteron beam, secondary charged particles produced by the interation between the deuterons and the graphite converter as well as fission fragments. We start by simulating the neutron production rates and then the yield of the neutron-induced fission.

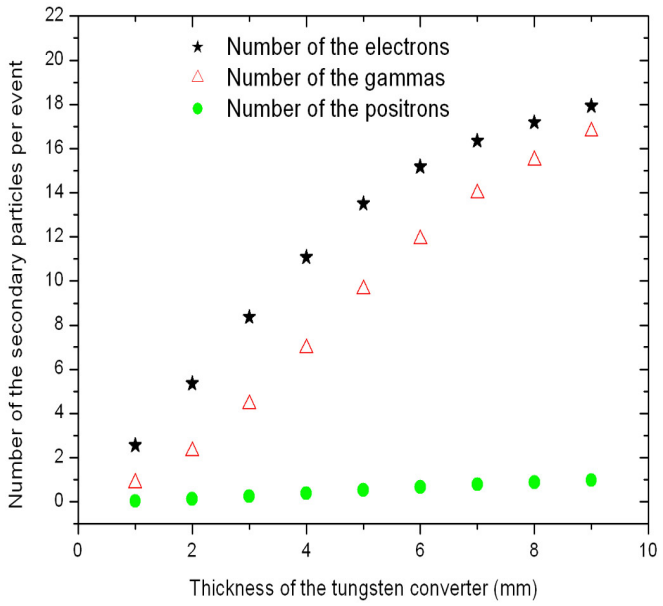

Figure 5.24: Number of secondary particles as function of tungsten converter thickness.

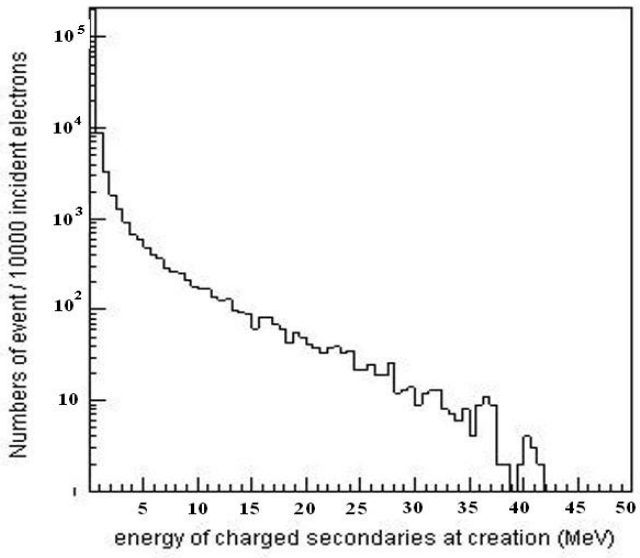

Figure 5.25: Energy spectrum of charged secondaries at their creation point for a 4 mm thick tungsten converter.

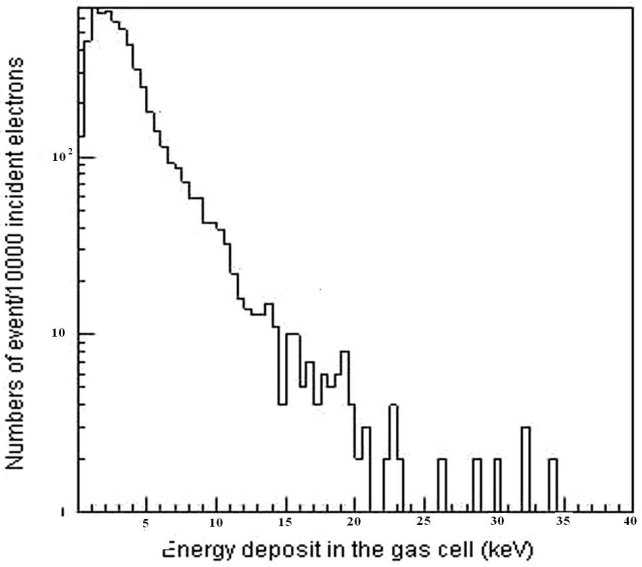

Figure 5.26: Spectrum of deposited energy in the gas cell for a 4 mm thick tungsten converter.

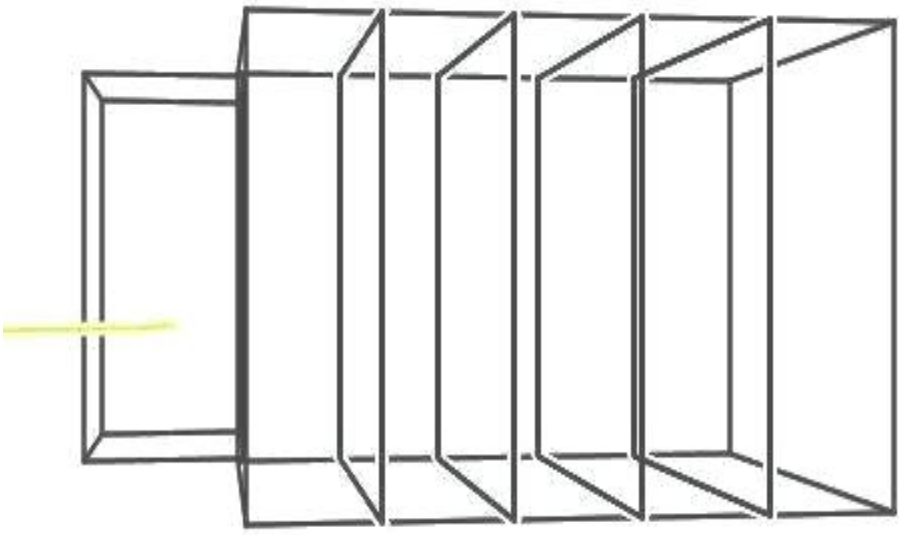

Figure 5.27: Visualisation of the SPIRAL-2 gas cell in GEANT-4.

Neutron production

The production of the high-energy neutrons in the carbon converter via the C(d,n) reaction is simulated through the GEANT-4 built-in code. The Quark-Gluon String Precompound, Binary Cascade and High Precision standard physics lists of Geant-4 were used (QGSP-BIC-HP). The processes taken into account break down for deuterons and neutrons as follows:

For deuterons: multiple scattering and ionisation processes are considered. The binary light ion cascade is used to model the inelastic interaction of ions with matter up to a few GeV /nucleon.

For neutrons: elastic and inelastic scattering (within the binary cascade model), capture and neutron-induced fission are considered. The physics list uses the data-driven high-precision neutron package Neutron-HP to transport neutrons below 20 MeV down to thermal energies.

In our calculation, a 40 MeV primary deuteron beam of 5 mA/cm^2 hits a thick graphite converter. The mean energy loss of the deuterons in the graphite dE/dx is equal to 39.88 MeV/cm. A converter thickness of 10 cm is taken such that the deuterons are stopped in it. The calculated yield of the neutrons emitted from the converter is 0.021 neutrons per incident deuteron. The MCNPX code gives a comparable value of 0.025 neutrons per deuteron [47].

The angular distribution and the energy distributions at different angular ranges are shown in figures 5.28 and 5.29. These distributions are in qualitative agreement with the calculations based on the Serber model as well as the experimental data cited in [52]. In particular, the GEANT-4 results show a peak at low energy that is not present in the spectra of the Serber model but the existence of which is experimentally established. However, the maximum of the energy distributions (not taking into account the low energy peak) is systematically higher than both in the Serber model and in the data, where

it is situated just below half the energy of the incident beam.

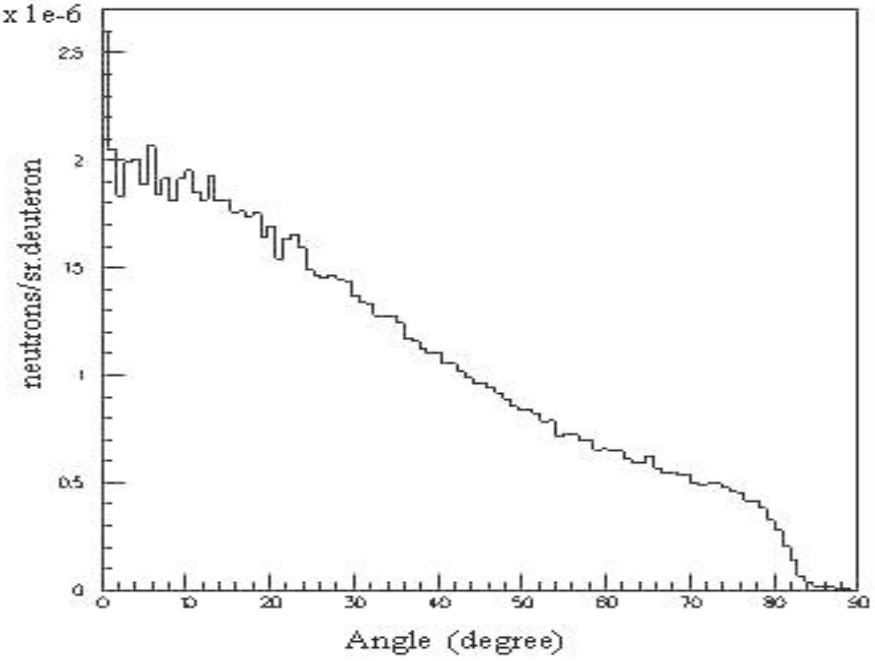

Figure 5.28: Simulated angular distribution of neutrons produced in C(d,n) reaction for 40 MeV deuteron beam.

The simulated fission yield that we obtain for the eventual Spiral-2 gas cell is 6×10^{-6} fissions per deuteron. For a 5 mA deuteron beam, the total fission yield becomes 1.9×10^{11} per second.

Energy deposit and ionisation rate

Besides the physics processes for deuterons and neutrons, we now also enable the standard electromagnetic physics processes for secondary charged particles, which are produced by the interaction of the deuterons in the converter. In addition, we include the ionisation of and the energy loss in the material by ions or fission fragments. The calculated total energy deposit per deuteron and the ion-electron pair production rate Q for a deuteron beam

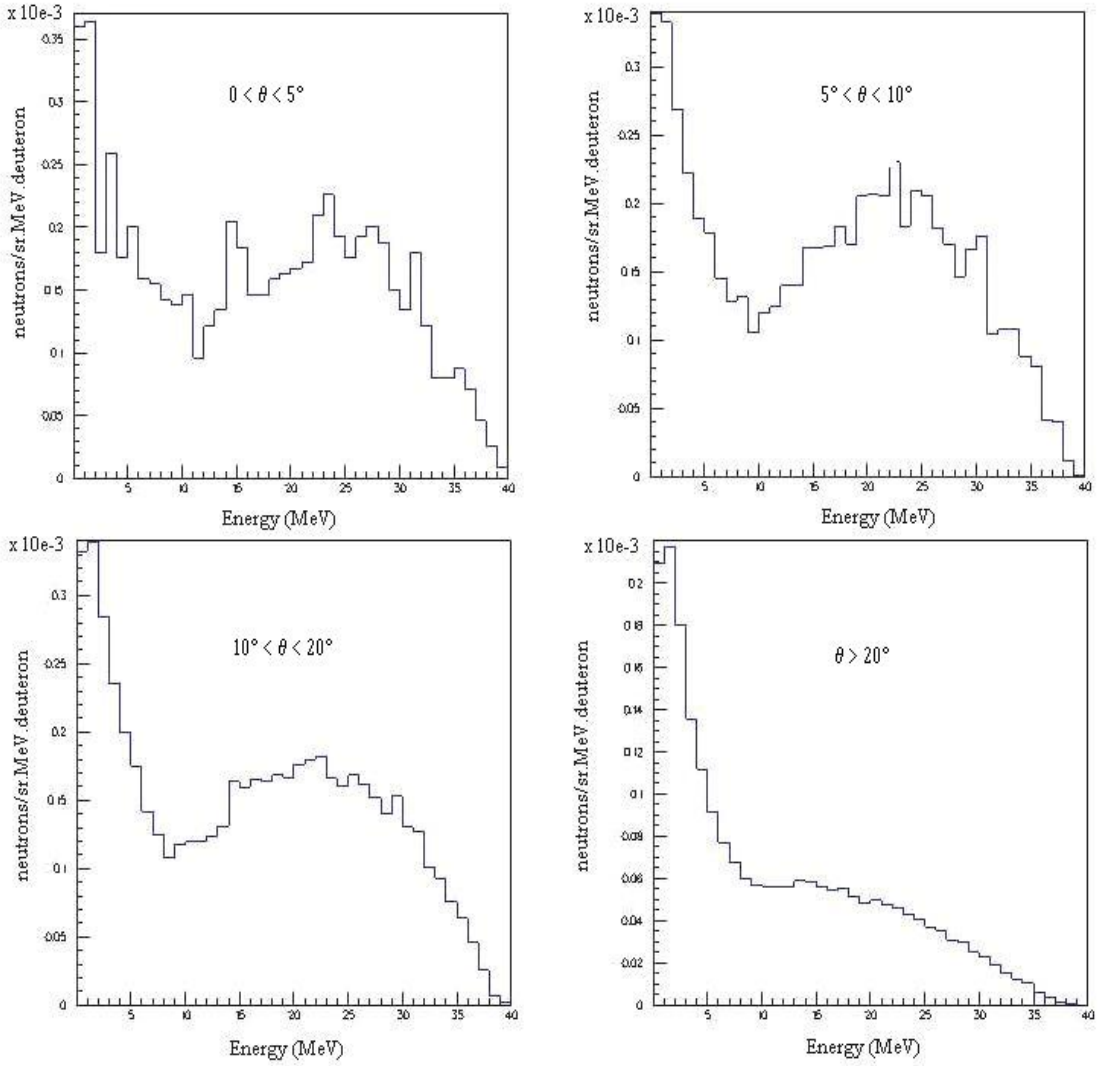

Figure 5.29: Simulated energy distribution of neutrons produced at different angles in C(d,n) reaction for 40 MeV deuteron beam.

of 5 mA in the gas cell, with and without considering the contribution from fission fragments, are presented in table 5.4. These figures are considerably less than what we obtained for the Leuven and the ALTO gas cells, because neutrons interact much less in the gas than protons or photons. Moreover, it appears that the fission fragments are responsible for a major share of 88 % in the total ionisation rate.

Table 5.4: Energy deposit per deuteron ΔE and ionisation rate Q in the SPIRAL-2 gas cell.

	ΔE /deuteron (eV)	Q ($\mathrm{cm^{-3}s^{-1}}$)
Without fission	0.371	1.09×10^{13}
With fission	2.96	8.76×10^{13}

5.3.4 Conclusion

In table 5.5 we summarise the ion-electron pair production rate Q in a gas cell of typical volume for the cases of the 1 μA 30 MeV proton beam at Louvain-la-Neuve, 10 μA 50 MeV electron beam at ALTO and 5 mA 40 MeV deuteron beam at Spiral-2. As can be seen, the Q value of the Louvain-la-Neuve gas cell is the highest, while for the deuteron beam it is more than an order of magnitude lower.

Table 5.5: Ionisation rates Q for the gas cell at Louvain-la-Neuve, ALTO and SPIRAL-2

	Q ($\mathrm{cm^{-3}s^{-1}}$)
Louvain-la-Neuve	2.55×10^{15}
ALTO	1.2×10^{15}
SPIRAL-2	8.76×10^{13}

In the past, the ion-guide technique has been applied successfully at Louvain-la-Neuve. Therefore, it should, in principle be possible to use it for future ion sources at ALTO and the SPIRAL-2 project.

In practice, however, the target area of SPIRAL-2 will be a hostile high-radiation environment where access will be severely limited. An ion guide for SPIRAL-2 should be much more robust than the designs that currently exist. For instance, neutron activation of the buffer gas would need to be taken into account and proper procedures for remote monitoring and handling would need to be developed.

The many constraints that are imposed by the target area of SPIRAL-2 have led to a newer proposal instead to install a gas cell behind the Super Spectrometer Separator S3 (see Fig. 5.30) [10]. This separator is presently being designed at GANIL and will offer competitive conditions for the study of nuclei produced in high-intensity heavy-ion reactions. The beam irradiating the buffer gas would then be composed of low-energy heavy reaction residues rather than deuterons, the feasibility of which has already been proven at Louvain-la-Neuve [30]. Through these heavy-ion reactions, in particular exotic refractory isotopes could be aimed at that then could be injected into the different experimental areas of SPIRAL-2, opening a wide field of interest at the border of our current knowledge.

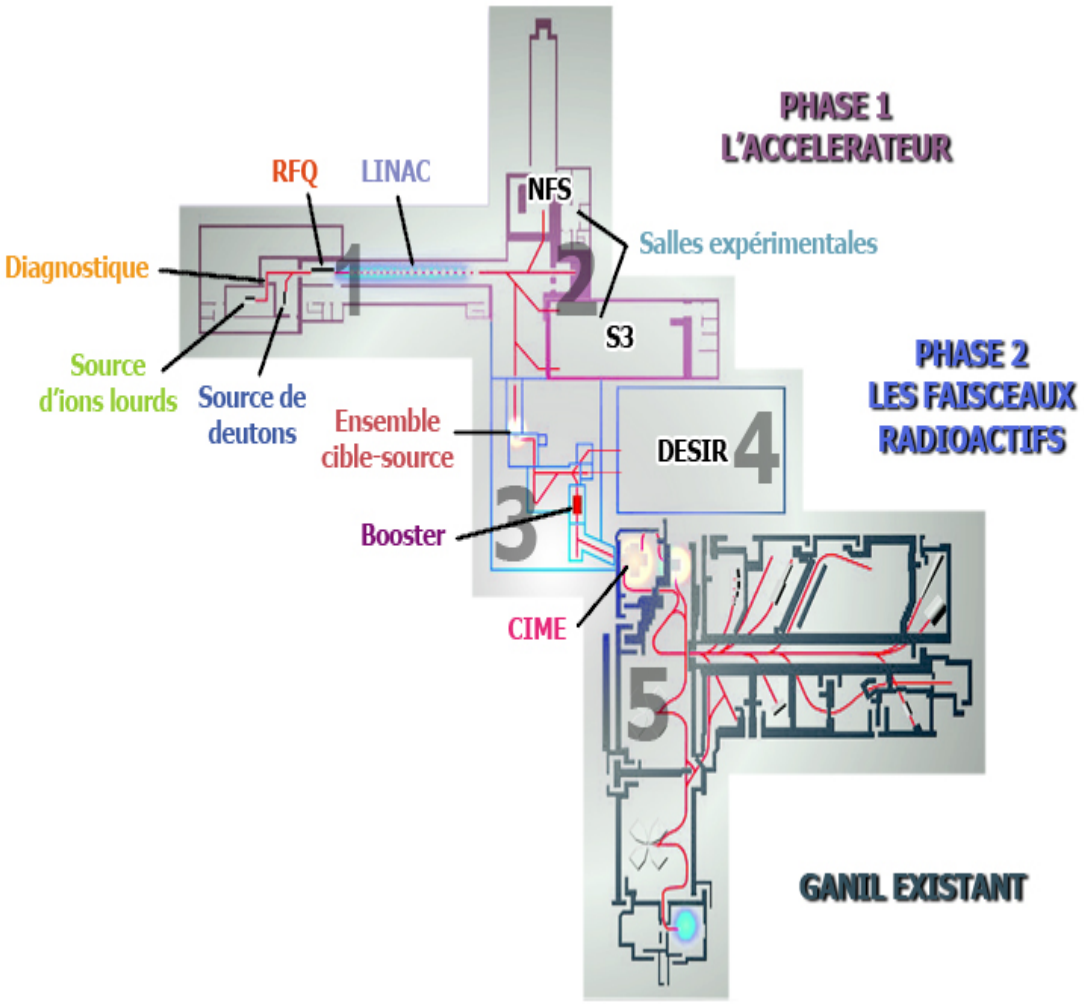

Figure 5.30: Layout of the SPIRAL-2 project setup.

Chapter 6

Conclusions and perspectives

In the year 2000, after the viability of photo-fission was successfully demonstrated through an experiment at CERN, the ALTO project at IPN Orsay was initiated. Six years later, the first radioactive beams were extracted from the UC_x fission target and the measured production rates indicated that once the nominal current of the ALTO electron beam of 10 μA will be reached, the in-target production rate will be 10^{11} fissions per second.

I started my thesis at IPN Orsay in December 2005 and I focused on the following tasks:

- research and development of a new surface ion source for the ALTO facility in order to produce selectively neutron-rich gallium isotopes for nuclear structure studies of their β decay;
- study of the possibility to use the laser ion guide ion source at ALTO as well as at SPIRAL-2.

Based on the Saha-Langmuir theory and other requirements for a surface ion source, rhenium and iridium were selected as materials for the ionisation cavity. In my work, I dedicated efforts to develop this ion source and perform the experiment to measure the surface ionisation efficiency at the off-line separator SIHL at Orsay. For optimising the dimensions of the cavity, I

built a C++ code on the basis of a Monte-Carlo simulation for the ionisation efficiency in different cavities. The code was applied to the ISOLDE surface ion source and reproduced reasonably well the experimental data. The code can therefore be instrumental for designing future developments of the surface ion source.

As to the practical work, a surface ion source with an iridium-coated rhenium cavity of the same dimensions as the cavity at ISOLDE was installed at the SIHL separator. In order to measure the ionisation efficiency for gallium, a quantity of stable gallium was put inside and the ensemble was heated to a temperature $T \approx 1800°C$. A separated gallium current was then detected by a Faraday cup. However, soon after the tube melted for a reason that was not understood clearly. The failure of the test experiment warns us that it is perhaps impossible to use an ionisation cavity made entirely from rhenium. However, a surface ion source with a tungsten or tantalum tube the inner surface of which is covered by a thin rhenium foil could be a better solution [14].

To calculate the ion-electron pair production rate in a possible laser ion guide ion source at ALTO, the photo-fission (γ,f) and photo-nuclear (γ,n) and (γ,2n) reactions were implemented in GEANT-4. This allowed me to evaluate the photo-fission and photo-nuclear reaction yields together with the additional fission yield that is induced by the neutrons produced in the photo-nuclear reactions. Consequently, the ionisation rate of the ion guide buffer gas by the primary electron beam as well as by the fission fragments was determined and the latter was shown to be negligible.

In view of the SPIRAL-2 project, where fission will be induced by neutrons from the C(d,xn) reaction, a code based on Geant-4 was written to simulate the neutron production, neutron-induced fission as well as ionisation in a buffer gas. The results for the neutron distribution show that GEANT-4 can reproduce well the data, including those at low energy where

the Serber model is deficient [52].

Finally, the calculated ionisation rates in a prospective gas cell for both ALTO and SPIRAL-2 indicate that the ion-guide technique can in principle be used for them. While organisational and technical issues (for instance, accessibility in a high-radiation environment) may presently not converge to a speedy implementation, current developments may be favourable instead for a gas cell at the Super Separator Spectrometer at SPIRAL-2. Heavy ions produced in a primary target at the entrance of the spectrometer would be stopped in a buffer gas at the exit of the spectrometer, where they would be measured in their own right or fed into the other experimental areas of SPIRAL-2. It is hoped that the present thesis may provide some of the groundwork for this.

Appendix A

Iridium-Coated Rhenium by Chemical Vapor Deposit (CVD)

As mentioned in chapter 3, iridium is one of three metal with highest working function ($\phi = 5.27eV$). Besides, it has a very high melting temperature (2440° C). Therefore, it would seem to be suitable for making a surface ion source. However, iridium is a very hard metal and therefore it is very brittle, impossible to draw and very difficult to machine to have the cylinderical shape of a typical ionisation cavity. In order to be still able to use this metal in surface ion source, coating the iridium on the surface of a substrate of a refractory metal might be a good solution. Among the refractory metals, rhenium is a possible candidate due to its advantageous properties following:

- The very high melting temperature: 3180°C.
- The high temperature strength and thermal shock resistance of rhenium, which surpass those of all other elements and almost all alloy systems.
- The high working function ($\phi = 4.96$eV), hence the surface ionisation efficiency isn't reduced significantly at the area of bad coating.

- Iridium bonds to, but does not form a eutectic with, rhenium.
- Rhenium's thermal expansion is very close to that of iridium.
- Rhenium lacks oxidation resistance at high temperature but this can be provided by a coating of iridium which has chemical inertness at high temperature.
- Last but not least, rhenium is also hard but it is still possible to machine into the shape of an ionisation cavity.

A.1 Fabrication

CVD is a method of plating which relies on the chemical reaction of a vapor at a surface to form solid structural deposits. The CVD process utilizes a gaseous compound of the element to be deposited, which is flowed over a heated substrate, resulting in thermal decomposition of the material onto the substrate. The first layer forms at nucleation sites; after the substrate is fully covered, growth continues on the crystal faces of the deposit.

Successful CVD-dense, adherent coatings depend on experimentally determining the optimal deposition parameters. These parameters include the gaseous compound of the material to be deposited, substrate temperature, gas concentration, flow, pressure and geometry within the reaction chamber, coating thickness, and substrate material. For the coating to have high integrity and adhesion to the substrate, the substrate must either have a similar coefficient of expansion to that of the deposited material, or form a strong chemical or metallurgical bond with it.

The essential requirements of a CVD facility are that the substrate must be maintained at the correct temperature and the plating gases to be supplied in the correct ratio and at the correct pressure. The substrate is typically heated resistively, inductively, or in a hot wall furnace. The composition of

the plating gases is determined by the type of reaction to be used. The same materials may be deposited using different compounds and different reactions at different temperatures, with each producing good coatings but different crystal structures. The procedure for depositing iridium uses iridium pentaneddionate as the precursor compound. This organometallic compound is also known as iridium acetylacetonate (Ir ac-ac in brief), with the structural formula $Ir(CH_3COCHCOCH_3)_3$. The schematic of a typical CVD apparatus for depositing iridium is shown in figure A.1. Ir ac-ac is heated resistively in horizontal arm of the glass chamber. The carrier/reaction gases sweep the sublimed Ir ac-ac vapor past the area to be coated, which is heated by a 450 kHz magnetic field; iridium deposits on the needed area, while the reaction products are exhausted [17].

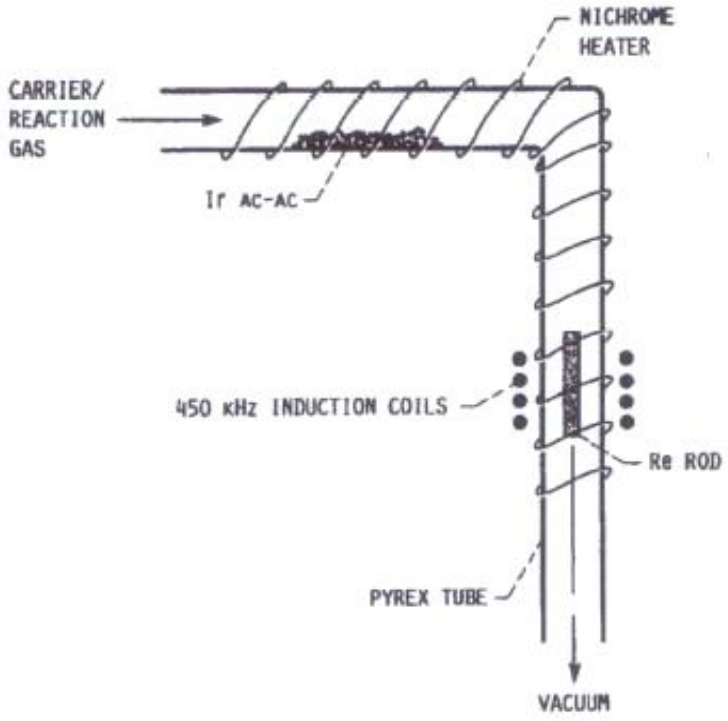

Figure A.1: CVD apparatus for coating Ir onto Re.

Bibliography

[1] NIST ITS-90 Thermocouple database.

[2] J. Al-Khalili and E. Roeckl, *The euroschool lecture on physics with exotic beams, vol. ii*, Springer-Verlag, New York, 2006.

[3] G. D. Alton and G. D. Mills, Nucl. Instr. Meth. Phys. Res. A **382** (1996), 232–236.

[4] J. Arijie, J. Äystö, J. Honkanen, K. Valli, and A. Hautojarvi, Nucl. Instr. Meth. **186** (1981), 149–152.

[5] J. Arijie, J. Äystö, H. Hyvonen, P. Taskinen, V. Koponen, J. Honkanen, A. Hautojarvi, and K. Vierinen, Phys. Rev. Lett. **54** (1985), 99–101.

[6] J. Arijie, J. Äystö, P. Taskinen, J. Honkanen, and K. Valli, Nucl. Instr. Meth. Phys. Res. B **26** (1987), 384.

[7] J. Arje and K. Valli, Nucl. Instr. Meth. **179** (1981), 533.

[8] Juha Äystö, Nucl. Phys. A **693**, 477–494.

[9] J. Cobilheux and G. D. Alton, AIP Conf. Pro. **576** (2001).

[10] SPIRAL's Collaborators, *Preliminary technical proposal for spiral 2 instrumentation*, (2008).

[11] P. Dendooven, Nucl. Instr. Meth. Phys. Res. B **126** (1997), 182–189.

[12] K. Deneffe, B. Brijs, E. Coenen, J. Gentens, M. Huyse, P. Van Duppen, and D. Wouters, Nucl. Instr. Meth. Phys. Res. B **26** (1987).

[13] W. T. Diamond, Nucl. Instr. Meth. Phys. Res. A **432** (1999), 471.

[14] A. Osa et al., Nucl. Instr. Meth. B **266**, 4394–4397.

[15] F. Ibrahim et al., Eur. Phys. J. A **15** (2002), 357–360.

[16] J. T. Caldwell et al, Phys. Rev. C **21** (1980), 1215.

[17] J. T. Harding et al., NASA Technical Memorandum 101309 (1998).

[18] J. Thomas et al., Phys. Rev. C **76** (2007), 044302.

[19] J.P.Omtvedt et al., Z. Physik A **338** (1991), 241.

[20] K.-L. Kratz et al., Z. Phys. A **340** (1991), 419.

[21] K. Morita et al., Nucl. Instr. Meth. Phys. Res. B **70** (1992), 220.

[22] M. Asai et al., Nucl.Instr. Meth. Phys. Res. B **506** (2003), 250–303.

[23] M. Facina et al., Nucl. Intr. Meth. Phys. Res. B **226** (2004), 401–418.

[24] M. Mirea et al., Nucl. Instr. Meth. Phys. Res. B **201** (2003), 433–448.

[25] M. Oshima et al., Nucl. Instr. Meth. Phys. Res. B **70** (1992), 241–244.

[26] O. Perru et al., Eur. Phys. J. A **28** (2006), 307.

[27] T. T. Inamura et al., Nucl. Instr. Meth. Phys. Res. B **70** (1992), 226.

[28] U. Köster et al., Nucl. Instr. Meth. Phys. Res. B **204** (2003), 347.

[29] V. Fedosseev et al., Nucl. Instr. Meth. Phys. Res. B **204** (2003), 353.

[30] Y. Kudryavtsev et al., Nucl. Instr. Meth. Phys. Res. B **114** (1996), 350–365.

[31] Y.Kudryavtsev et al., Nucl. Instr. Meth. Phys. Res. B **204** (2003), 336–342.

[32] Yu. Ts. Oganessian et al., Nucl. Phys. A **701** (2002), 87.

[33] M. Facina, *A gas catcher for the selective production of radioactive beams through laser ionization*, Ph.D. thesis, Leuven University, 2004.

[34] F.Ibrahim, *Lecture on Production of RIB: ISOL Method*, Lecture Notes, XIVth Euro Summer School on Exotic Beam, Houlgate, Frace, 2007.

[35] S. Franchoo, *Cahier des charges aligre*, Private Communication.

[36] http://en.wikipedia.org/wiki/Gallium.

[37] M. Huyse, M. Facina, Y. Kudryavtsev, and P. Van Duppen, Nucl. Instr. Meth. Phys. Res. B **187** (2002), 535–547.

[38] F. Ibrahim, Physics of Atomic Nuclei **66** (2003), 1399–1406.

[39] R. Kent, Los Alamos scientific laboratory, LA-5202-MS informal report (1973).

[40] U. Köster, Communication at the Workshop on Spectroscopy of Neutron-rich Nuclei, Chamrousse, France (16-20 March 2008).

[41] ———, Nucl. Phys. A **701** (2002), 441–451.

[42] Ulli Köster, *Yield and Spectroscopy of Radioactive Isotopes at LOHENGRIN and ISOL*, Ph.D. thesis, TU Munchen, 2000.

[43] M. Lebois, *IPN Orsay and Triumf*, Private Communication.

[44] M. Lebois and D. Verney et al, Phys. Rev. C **80** (2009), 04430.

[45] M. Lebois, M. Cheikh Mhamed, J. M. Curaudeau, M. Ducourtieux, S. Essabaa, S. Franchoo, S. Galès, D. Guillemaud-Muller, F. Ibrahim, C. Lau, J. Lesrel, A. Mueller, M. Raynaud adn B. Roussière adn A. Said, D. Verney, C. Vogel, and the ALTO Collaboration, Proceedings of EXON2006, Khanty-Mansiysk (17-22 July 2006).

[46] Mathieu Lebois, *Struture des noyaux de germanium et de gallium riches en neutrons au-del de n=50 alto*, Ph.D. thesis, Universit Paris-Sud, 2008.

[47] X. Ledoux and D. Ridikas, *Neutrons for science (nfs) at SPIRAL-2*, SPIRAL-2 Workshop (13-14 December 1998).

[48] Mario Santana Leitner, *A monte carlo code to optimize the production of radioactive ion beams by the ISOL technique*, Ph.D. thesis, Technical University of Catalonia (UPC), 2005.

[49] M. Lewitowicz, *The SPIRAL-2 project*, Nuclear Physics A **805** (2008), 519c–525c.

[50] M. Lindroos, Proceedings of EPAC 2004, Lucerne, Switzerland (2004).

[51] T. Nomura, Nucl. Instr. Meth. A **269** (1988), 23.

[52] N. Pauwels, Ph.D. thesis, Université Paris-Sud, 2000.

[53] Z. Qamhieh, E. Vandeweert, and R. E. Silverans, Nucl. Instr. Meth. Phys. Res. B **70** (1992), 131–136.

[54] F. Sauli, *in: Experimental Techniques in High-energy Nuclear and Particle Physics, T. ferbel (ed.)*, (World Scientific) (1991).

[55] P. Taskinen, H. Pentilla, J. Äystö, P. Dendooven, P. Jauho, A. Jokinen, and M. Yoshii, Nucl. Instr. Meth. A **281** (1989), 539.

[56] U.Köster, *The status of Ga beams was presented at ISOLDE*, Note on the 1^{st} meeting of the target and ion-source working group, Geneva (13 September 2000).

[57] J. Vervier, *Status of the EURISOL Project*, Nucl. Instr. Meth. Phys. Res. B **204** (2003), 759–764.

[58] K. Wendt, Nucl. Instr. Meth. Phys. Res. B **204** (2003), 325.

[59] R. G. Wilson, IEEE Trans. Nucl. Sci. **NS-14** (1967), 72–74.

[60] J. A. Winger, Proc. of the 4th International Conference on Fission and Properties of Neutron-rich Nuclei, Sanibel Island, Florida (2008).